Improvement of the Excavation Damaged Zone in Saliferous Formations

Vergütung der Auflockerungszone im Salinar

Phase II

Final Report

Verantwortung für Generationen
Responsibility for Generations

DBE TECHNOLOGY GmbH

Improvement of the Excavation Damaged Zone in Saliferous Formations

Vergütung der Auflockerungszone im Salinar

Phase II

- Generierung von Risssystemen einer Auflockerungszone im Korngrößenmaßstab und Überführung der Ergebnisse auf die Makroebene zur Simulation eines Injektionsvorganges -

Müller, C.; Simo Kuate, E.; von Borstel, L.; Engelhardt, H.J.

DBE TECHNOLOGY GmbH
Eschenstraße 55
D-31224 Peine

Januar 2016

Supported by:

on the basis of a decision
by the German Bundestag

The research work that is the basis of this report was supported by the German Federal Ministry for Economic Affairs and Energy (BMWi = Bundesministerium für Wirtschaft und Energie) represented by the Project Management Agency Karlsruhe (Karlsruhe Institute of Technology, KIT), under contract no. FKZ 02 E 11082. The authors alone, however, are responsible for the contents of this study.

Table of Contents

Abstract

In Germany, salt formations are considered to be suitable to host a deep geological repository for radioactive waste. However, local stress changes adjacent to man-made openings lead to the evolution of an excavation damaged zone (EDZ) during and after excavation. Such an EDZ can have a major impact on the operation of a radioactive waste repository since it represents a region where progressive failure occurs. This decreases the material strength and thus increases the permeability of the originally tight host rock. The objective of this investigation is determined by the need to develop a modeling strategy that can be applied to simulate the permeability increase due to mechanical deterioration of rock salt, in particular that occurring in the EDZ. In order to simulate the shape and arrangement of crystal grains in rock salt, discontinuum approaches were applied using polyhedral elements for the simulation. The polyhedral-shaped discrete elements, which were used here, are called Voronoi polyhedra.

The discrete element method (DEM) differs fundamentally from the continuum approach used so far for salt mechanics problems. Since the shape and arrangement of grains can strongly influence the damage behavior of rocks, it was first checked how well the Voronoi tessellation corresponds to the microstructure of real rock salt samples. The comparison of real and simulated microstructures is based on quantitative image analysis of thin sections of rock salt by determining typical microstructural features, e.g. shape, size, and orientation of grains. The sphericity and the length-to-width ratio of grains correspond well to the rock salt samples used for comparison but there are differences regarding the grain size distribution and the orientation of the grains. The rock salt samples show a significantly larger proportion of smaller grains. Furthermore, a directional anisotropy in terms of particle shape was recognized. However, a further adaption of the polyhedral elements was not carried out in order to avoid the generation of smaller polyhedral edges or bad-quality zone elements.

The DEM subdivides the volume into smaller elements and thus describes a discontinuous distribution of rock salt grains at the microscopic level. Thus, the controlling processes for mechanical deterioration of rock salt at grain scale were identified by making a distinction between physical processes occurring within and between the salt grains. It has been described in the literature that both intra- and intercrystalline deformation processes are related to each other. Incompatibilities in the plastic deformation of adjacent crystal grains cause local stresses at the grain boundaries, which lead to the formation of intergranular mirco cracks. Therefore, anisotropic plastic deformation behavior of individual grains should be considered when using constitutive models. However, since suitable models are not available and the entirely new development of a suitable anisotropic constitutive model would go beyond the scope of this project, simple constitutive models were used and optimized. The objective was to adjust the cooperative nature of crystal plasticity and cracking along the grain boundaries due to an appropriate parameter combination.

The EDZ is formed immediately after excavation due to local stress changes. Assuming that time-dependent creep (dislocation creep) has no impact on the formation of the EDZ, only short-term deformation was taken into account, i.e., evolution of dilatancy due to microstructural deterioration, primary creep caused by strain hardening (dislocation glide), short-term

compressive strength, and residual strength above the peak strength. To simulate the deformation within the salt grains, a continuum-based Mohr Coulomb criterion with an additional strain hardening approach was used. Plastic dilatancy due to fracturing along the grain boundaries is based on a continuum Mohr Coulomb elasto-plastic criterion (shear yield function) including a tension cut-off condition (tension yield function). The friction angle was set to zero to simulate ideal plastic material behavior and the residual cohesion was set to zero to simulate frictional sliding after slip has occurred. The remaining micro parameters used in the distinct element code to describe the mechanical behavior for both grains and grain boundaries are not known and needed to be calibrated. The identification of material parameters is often conducted by back-calculation of laboratory experiments. However, standard laboratory tests, e.g. compression tests, are only applicable to provide information about the macroscopic deformation. For this purpose, further laboratory tests were conducted to derive material parameters used in the constitutive models. Combined acoustic emission and uniaxial compression tests as well as microstructural analyses were carried out to dissolve the macroscopic behavior micromechanically. The information obtained was then used for parameter identification utilizing optimization methods. The objective was to identify the best estimate of the micro-parameter values that can be applied to simulate the laboratory results performed. With regard to the axial strain, a comparison to laboratory and numerical tests succeeded well. Axial stresses reach approximately the axial compressive strength of the laboratory test with values of 27 MPa. The lateral strain accumulation of up to 0.1% is also identical to laboratory results. However, with increasing stress it comes to a lower elongation in lateral direction in contrast to laboratory results. Since the volumetric strain results directly from axial as well as lateral strain, significant increase in volumetric strain is less pronounced in the numerical analysis due to lower lateral strain accumulation. To make a qualitative comparison between the numerical analysis and the acoustic emission (AE) testing, the onset of failure at contacts was equated with events detected by AE testing. The onset of failure is identified at stress levels above 3 MPa. The number of tensile fractures increases continuously and the maximum is reached between 10 and 12 MPa axial stress. At the beginning of loading, tensile fractures appear more frequently than shear fractures, which is in good agreement with laboratory results. It also has been shown that the correct mechanical behavior is mainly achieved by an adequate parameter set controlling grain deformation and deformation along the grain boundaries.

The calibrated parameter combination was then used to generate realistic fracture networks occurring in the EDZ. For this purpose, the excavation of a drift is simulated with continuum mechanical approaches and the zone stresses are recorded in certain parts and for certain depths of the EDZ. The zone stresses are then transferred as boundary stresses on a discontinuum model that comprises polyhedral elements to simulate the fracture development at grain scale. The results of the DEM modelling show a fracture-induced anisotropy and fractures are oriented parallel to the maximum principal stress. It could be shown that the most damaged region is at a depth of 0.5 m from the drift contour. Between 2-3 m depth the fracture density decreases considerably. The results are in good agreement with simulations performed with continuum mechanical approaches and using the dilatancy boundary after Critescu & Hunsche (1998) to describe the damage in rock salt.

The permeability increase in the EDZ can compromise the sealing function of the originally tight rock salt. Therefore, the specification of adequate permeability values is mandatory since it provides information about major pathways for fluid flow. However, the larger number of fractures makes the discontinuum approach less efficient for large-scale modelling and methods are needed to upscale the information gained from discontinuum modelling. The commonly used method is based on the following principle: the fluid flow of a discontinuum model with fractures explicitly represented is similar to that of a continuum model having equivalent hydraulic properties. For this purpose, the hydraulic conductivity tensor of the fracture systems which have already been generated was investigated by simulating the flow under different hydraulic head directions. This allows the specification of directionally dependent (anisotropic) permeability values that can be used as input parameters for large-scale modelling. The models must be calibrated which is generally similar to the procedure used for calibrating the mechanical input parameters: fracture transmissivities are varied until conformity between measured and simulated results is achieved. However, it is very difficult to obtain relevant hydraulic information, and there was no data available that was suitable for calibration. The transmissivity through fractures is based on the cubic law that considers fluid flow between smooth-walled plates with a given aperture. For a first estimate, the aperture of fractures was therefore adjusted based on information coming from microscopic investigations. However, quantifiable and reliable permeability values depend mainly upon suitable aperture values since a change of 3 orders of magnitude in aperture would result in a 9 order of magnitude change in permeability. Nevertheless, realistic permeability values in the order of $10^{-15}\,m^2$ could be numerically calculated. The anisotropy of the fracture pattern is also reflected in the hydraulic conductivity tensor. An anisotropy factor of 1.73 can be specified at a depth of 0.5 m from the drift contour. For depths of 0 m and 2 m no tensor ellipsoid could be specified since the simulated fracture connectivity is below the percolation threshold.

In the first phase of the project, in situ experiments were conducted in order to verify the sealing injection technique using liquid silica. In situ experimental injection tests of liquid silica were performed in a small area of the EDZ in the mine Niedersachsen Riedel in Germany. The liquid silica was mixed with the fluorescent dye Uranin to visualize the silicate in rock salt. Once the work was completed and after a waiting period of three months, drill cores were taken from the injected host rock and thin sections were prepared to inspect the fracture system microscopically. However, a large-scale and continuous penetration of sodium silicate solution was not visible in the analyzed thin sections. Nevertheless, valuable and important insights and previously unknown phenomena could be described. It had previously not been known where the reaction solution remains after the injection of sodium silicate. It was shown that the reaction solution may continue to migrate into the rock salt and become trapped within the crystal structure in the form of fluid inclusions. Furthermore, it could be shown that sodium silicate solution can penetrate into crack systems with widths less than 10 microns and seal them.

The last part of the study is about the long-term stability of liquid silica improved rock salt samples. A laboratory research program was conducted during the first phase of the project which considered an injection of rock salt with sodium silicate solution. The influence of the contact with NaCl and $MgCl_2$ solutions on the mineral content and the composition of the solutions were investigated. These studies have been completed by analyzing the solubility

of amorphous silica in saturated NaCl solutions with $MgCl_2$ of varying concentration. Additionally, it was tested whether amorphous silica is able to act as a chemical barrier by analyzing the reaction behavior of selected trace elements in contact with amorphous silica.
It could be shown that in saline environment, the silicate is insoluble in saturated brines, transforms over time into stable crystalline SiO_2-phases and forms stable MOC-Phases in the presence of Mg^{2+}. First laboratory tests to verify the use (application) of silicate to act as a chemical barrier against repository-relevant elements supply promising results. In the course of the experiment, a decrease in the concentration of several elements is observed. This means that amorphous silicate may act as a chemical barrier for specific elements in the saline environment.

Zusammenfassung

In Deutschland werden Salzformationen als geeignete Standorte für tiefe geologische Endlager für radioaktive Abfallstoffe angesehen. Lokale Spannungsänderungen können jedoch während und nach der Auffahrung zur Ausbildung einer Auflockerungszone (ALZ) führen. Solch eine Auflockerungszone kann wesentliche Auswirkungen auf den Betrieb eines Endlagers für radioaktive Abfälle haben, da sie einen Bereich darstellt, wo das Wirtsgestein geschädigt ist. Das verringert die Materialfestigkeit und erhöht somit die Permeabilität des ursprünglich dichten Wirtsgesteins. Das Ziel dieser Untersuchungen ist die Entwicklung einer Modellierungsstrategie, die dazu verwendet werden kann, den Permeabilitätsanstieg in der Auflockerungszone von Steinsalz aufgrund von mechanischer Schädigung zu modellieren. Zur Simulation der Form und Anordnung von Kristallkörnern in Steinsalz wurden Diskontinuumsansätze eingesetzt, die polyedrische Elemente für die Simulation verwenden. Die hier verwendeten polyedrischen Diskreten Elemente werden Voronoi Polyeder genannt.

Die Diskrete Elemente Methode (DEM) unterscheidet sich grundlegend von dem üblicherweise in der Salzmechanik verwendeten Kontinuumsansatz. Da die Form und Anordnung der Körner wesentlichen Einfluss auf das Schädigungsverhalten eines Gesteins haben können, wurde zunächst untersucht, wie gut die Voronoi-Elemente die Mikrostruktur von Steinsalzproben abbilden. Der Vergleich von realen und simulierten Mikrostrukturen basiert auf einer quantitativen Bildauswertung von Dünnschliffproben zur Ermittlung typischer mikrostruktureller Eigenschaften, wie z.B. Form, Größe und Orientierung der Körner. Die Sphärizität und das Länge-Breite-Verhältnis der Körner weisen eine gute Übereinstimmung mit den für den Vergleich genutzten Steinsalzproben auf. Allerdings gibt es Unterschiede bei der Korngrößenverteilung und der Kornorientierung. Die Steinsalzproben haben einen wesentlich höheren Anteil an kleineren Körnern. Außerdem wurde eine Richtungsabhängigkeit (Anisotropie) bezüglich der Form der Elemente festgestellt. Eine weitere Anpassung der Polyederelemente wurde jedoch nicht vorgenommen, um zu vermeiden, dass kleinere polyedrische Kanten oder Elemente mit Bereichen schlechter Qualität erzeugt werden.

Die DEM unterteilt das Volumen in kleinere Elemente und beschreibt so eine diskontinuierliche Verteilung von Steinsalzkörnern auf mikroskopischer Ebene. Die Unterscheidung zwischen physikalischen Prozessen innerhalb und zwischen Salzkörnen stellt daher eine erste wesentliche Grundlage für die Wahl geeigneter Stoffmodelle dar. In der Literatur wird beschrieben, dass sowohl inter- als auch intrakristalline Verformungsprozesse miteinander in Verbindung stehen. Inkompatibilitäten in der plastischen Verformung angrenzender Kristallkörner erzeugen lokale Spannungen an den Korngrenzen, die zur Bildung intergranularer Mikrorisse führen. Bei der Verwendung von Stoffmodellen sollte deshalb das anisotrope plastische Verformungsverhalten der einzelnen Körner berücksichtigt werden. Da geeignete Modelle jedoch nicht zur Verfügung stehen und die Neuentwicklung eines geeigneten anisotropen Stoffmodells den Rahmen dieses Projektes überschreiten würde, wurden einfache Stoffmodelle verwendet und optimiert. Ziel war es, das Zusammenwirken von Kristallplastizität und Rissbildung entlang der Korngrenzen mit Hilfe einer geeigneten Parameterkombination zu simulieren.

Die ALZ wird direkt nach der Auffahrung aufgrund lokaler Spannungsänderungen gebildet. Ausgehend davon, dass zeitabhängiges Kriechen (Versetzungskriechen) keinen Einfluss auf die Ausbildung der ALZ hat, wurden nur zeitunabhängige Verformungsprozesse berücksichtigt, d.h. Entwicklung der Dilatanz aufgrund mikrostruktureller Schädigung, primäres Kriechen aufgrund von Verfestigungsprozessen (Versetzungsgleiten), Kurzzeitfestigkeit und Restfestigkeit oberhalb der Höchstfestigkeit. Um die Verformung innerhalb der Salzkörner zu simulieren, wurde ein kontinuumbasiertes Mohr-Coulomb-Kriterium mit zusätzlichem Verfestigungsansatz gewählt. Für die Korngrenzen wurde ein Mohr-Coulomb Ansatz gewählt. Der Reibungswinkel wurde auf Null gesetzt, um ideales plastisches Materialverhalten zu simulieren. Oberhalb der Bruchgrenze wird ein einfaches Reibgesetz angenommen.

Geeignete Kennwerte für die in den Stoffmodellen verwendeten Parameter zur Beschreibung des mechanischen Verhaltens in und entlang der Körner sind allerdings nicht bekannt und müssen kalibriert werden. Materialparameter werden häufig durch Rückrechnung von Laborversuchen ermittelt. Mit Standardlaborversuchen, z.B. Druckversuchen, können allerdings nur Informationen über makroskopische Verformungen ermittelt werden. Zu diesem Zweck wurden weitere Laborversuche zur Ermittlung von Materialparametern für die Materialmodelle durchgeführt. Um das makroskopische Verhalten mikroskopisch aufzulösen, wurden einaxiale Druckversuche mit akustischen Emissionsmessungen sowie mikrostrukturellen Analysen kombiniert. Die so erhaltenen Informationen wurden dann mit Hilfe von Optimierungsmethoden zur Identifizierung von Parametern verwendet. Ziel war es, geeignete Kennwerte für die Mikroparameter zu ermitteln, die am besten zur Simulation der durchgeführten Laborversuche verwendet werden können. Hinsichtlich der Axialspannung war ein Vergleich mit den Laborversuchen und numerischen Versuchen sehr erfolgreich. Mit Werten von 27 MPa erreichen die Axialspannungen ungefähr die axialen Druckspannungen der Laborversuche. Auch die Querdehnung von bis zu 0,1% entspricht den Laborergebnissen. Im Gegensatz zu den Laborergebnissen kommt es jedoch mit zunehmender Spannung zu einer geringeren Verformung in lateraler Richtung. Da die volumetrische Verformung ein direktes Ergebnis der axialen und lateralen Verformung ist, sind signifikante Erhöhungen der volumetrischen Verformung in den numerischen Analysen aufgrund der geringeren lateralen Verformung weniger stark ausgeprägt. Für einen qualitativen Vergleich zwischen den numerischen Analysen und den akustischen Emissionstests wurde das Versagenseinsetzen an den Kontaktflächen mit Ereignissen, die bei den akustischen Emissionstests entdeckt wurden, gleichgesetzt. Schädigung tritt bei Spannungen über 3 MPa auf. Die Anzahl an Rissen nimmt kontinuierlich zu, wobei das Maximum bei einer axialen Spannung zwischen 10 und 12 MPa erreicht wird. Zu Beginn der Belastung treten Spannungsrisse häufiger auf als Scherbrüche, was gut mit den Laborergebnissen übereinstimmt. Es zeigte sich auch, dass das richtige mechanische Verhalten hauptsächlich durch eine geeigneten Parameterkombination erreicht wird, der die Kornverformung und die Verformung entlang der Korngrenzen steuert.

Mit der kalibrierten Parameterkombination wurden dann realistische, in der Auflockerungszone vorkommende Rissnetzwerke generiert. Zu diesem Zweck wird die Auffahrung einer Strecke mit einem kontinuumsmechanischen Ansatz simuliert, und die Spannungen in bestimmten Bereichen und für bestimmte Tiefen der Auflockerungszone aufgezeichnet. Die Spannungen werden anschließend als Randbedingungen in ein Diskontinuum-Modell über-

tragen, das polyedrische Elemente zur Simulation der Rissentwicklung auf Kornebene beinhaltet. Die Ergebnisse der DEM-Modellierung zeigen eine rissinduzierte Anisotropie, wobei die Risse parallel zur maximalen Hauptspannung angeordnet sind. Es konnte gezeigt werden, dass sich der Bereich mit der größten Schädigung in einer Tiefe von 0,5 m von der Streckenkontur befindet. In einer Tiefe zwischen 2 und 3 m verringert sich die Rissdichte erheblich. Die Ergebnisse stimmen gut mit den Simulationen überein, die mit Ansätzen aus der Kontinuumsmechanik durchgeführt wurden und die Dilatanzgrenze nach Critescu & Hunsche (1998) zur Beschreibung der Schädigung des Steinsalzes verwendet haben.

Die Erhöhung der Permeabilität der Auflockerungszone kann die Dichtfunktion des ursprünglich dichten Steinsalzes beeinträchtigen. Deshalb ist die Angabe geeigneter Permeabilitätswerte zwingend erforderlich, da sie Informationen über wesentliche Lösungspfade liefern. Durch die größere Anzahl an Rissen ist der Diskontinuum-Ansatz allerdings weniger effizient für große Modelle, und es werden Methoden benötigt, um die durch das Diskontinuumsmodell erhaltenen Informationen auf die Makroebene zu überführen. Das am häufigsten verwendete Verfahren basiert auf folgendem Prinzip: Der Durchfluss in einem Diskontinuum-Modell, in dem Risse explizit dargestellt werden, ähnelt dem eines Kontinuum-Modells mit entsprechenden hydraulischen Eigenschaften. Zu diesem Zweck wurde der hydraulische Durchlässigkeitstensor der numerisch simulierten Risssysteme bestimmt, indem der Fluss unter verschiedenen hydraulischen Gradienten simuliert wurde. Dies ermöglicht die Festlegung von richtungsabhängigen (anisotropen) Permeabilitätswerten, die als Input-Parameter für die Modellierung im großen Maßstab verwendet werden können. Die Modelle müssen auch hier kalibriert werden, wobei die Methode der ähnelt, die für die Kalibrierung der mechanischen Input-Parameter verwendet wird: Die Transmissivität der Risse wird so lange variiert, bis die gemessenen und simulierten Ergebnisse übereinstimmen. Es ist jedoch sehr schwierig, relevante hydraulische Information zu bekommen, und es waren keinen Daten verfügbar, die für eine Kalibrierung geeignet waren. Die Transmissivität durch Risse basiert auf dem kubischen Gesetz, die eine Flüssigkeitsströmung zwischen glatten Wänden mit bekannter Öffnungsweite berücksichtigt. Für eine erste Einschätzung wurde die Öffnungsweite der Risse deshalb basierend auf Informationen aus mikroskopischen Untersuchungen verwendet. Quantifizierbare und zuverlässige Permeabilitätswerte hängen jedoch hauptsächlich von geeigneten Öffnungsweiten ab, da eine Änderung der Öffnungsweite von 3 Größenordnungen eine Änderung der Permeabilität von 9 Größenordnungen zur Folge hätte. Trotzdem konnten realistische Permeabilitätswerte in Höhe von $10^{-15}\,m^2$ numerisch bestimmt werden. Die Anisotropie des Rissmusters spiegelt sich auch im hydraulischen Durchlässigkeitstensor wider. In einer Tiefe von 0,5 m von der Streckenkontur kann ein Anisotropiefaktor von 1,73 ermittelt werden. Für die Tiefen 0 m und 2 m konnte kein Tensor-Ellipsoid ermittelt werden, da die simulierte Risskonnektivität unterhalb der Perkolationsschwelle liegt.

In der ersten Phase des Projektes wurden In-situ-Versuche durchgeführt, um die Injektionsmethode unter Verwendung von flüssigem Silica zu überprüfen. Diese In-situ-Versuche wurden in einem kleinen Bereich der Auflockerungszone des Bergwerks Niedersachsen Riedel in Deutschland durchgeführt. Das flüssige Silica wurde mit dem Fluorescein Uranin gemischt, um das Silikat im Steinsalz sichtbar zu machen. Nach Abschluss der Arbeiten und einer Wartezeit von drei Monaten wurden dem injizierten Wirtsgestein Bohrkerne entnom-

men, von denen Dünnschliffe präpariert wurden, um das Risssystem mikroskopisch zu untersuchen. Ein großräumiges und durchgängiges Eindringen der Natronwasserglaslösung war in den analysierten Dünnschliffen jedoch nicht sichtbar. Dennoch konnten wertvolle und wichtige Einblicke gewonnen und bisher unbekannte Phänomene beschrieben werden. Es war vorher nicht bekannt, wo die Reaktionslösung bleibt, nachdem das Natronwasserglas injiziert wurde. Es zeigte sich, dass die Möglichkeit besteht, dass die Reaktionslösung weiter in das Steinsalz eindringt und in Form von Lösungseinschlüssen in die Kristallstruktur eingebunden wird. Weiterhin zeigt sich, dass Natronwasserglaslösung in Risssysteme mit Weiten von weniger als 10 µm eindringen und diese abdichten kann.

Der letzte Teil der Studie befasst sich mit der Langzeitstabilität von mit flüssigem Silica vergüteten Steinsalzproben. Während der ersten Phase des Projektes wurde ein Laborversuchsprogramm durchgeführt, das die Injektion von Steinsalz mit Natronwasserglaslösung vorsah. Der Einfluss des Kontaktes mit NaCl- und $MgCl_2$-Lösungen auf den Mineralgehalt und die Zusammensetzung der Lösungen wurde untersucht. In diesen Studien wurde die Löslichkeit von amorpher Kieselsäure in gesättigter NaCl-Lösung mit variierendem $MgCl_2$-Gehalt analysiert. Zusätzlich wurde das Reaktionsverhalten ausgewählter Spurenelemente in Kontakt mit amorpher Kieselsäure analysiert, um zu testen, ob amorphe Kieselsäure als chemische Barriere fungieren kann. Es konnte gezeigt werden, dass das Silikat in salzhaltiger Umgebung in gesättigten Lösungen nicht lösbar ist, sich mit der Zeit in stabile kristalline SiO_2-Phasen umwandelt und in Anwesenheit von Mg^{2+} stabile MOC-Phasen bildet. Erste Laborversuche zur Überprüfung des Einsatzes von Silikat als chemische Barriere gegenüber für Endlager relevante Elemente zeigen vielversprechende Ergebnisse. Im Verlauf des Experiments wurde eine Konzentrationsabnahme mehrerer Elemente beobachtet. Das bedeutet, dass amorphe Kieselsäure in einer salzhaltigen Umgebung für bestimmte Elemente als chemische Barriere fungieren kann.

1 Introduction

In Germany, deep geological formations are regarded to be suitable to host repositories for radioactive waste. An important part of the safety concept is the identification of a suitable rock formation that ensures the safe enclosure of the waste. In addition to claystones and granitoid rocks, especially salt formations are suitable to host a deep geological repository for highly radioactive waste (Kockel & Krull, 1995). In Germany, the safety concept for a deep geological repository in salt formations considers not only the isolation capability of the geological barrier but also that of the geotechnical barriers in order to seal all man-made openings (e.g., shafts, chambers and drifts) (Krone, et al., 2008). However, local stress changes adjacent to man-made openings lead to the evolution of an excavation damaged zone (EDZ) during and after excavation. As proposed by Tsang et al. (2005), such an EDZ can have a major impact on the operation of a radioactive waste repository.

The EDZ is a region where progressive failure occurs. This decreases the material strength and thus increases the permeability of the originally tight host rock. It is known that the degradation is due to the initiation and propagation of microcracks. As proposed by Griffith (1921), the initiation of microcracks starts from existing flaws acting as stress concentrators. In crystalline materials, it is widely assumed that grain boundaries act as the predominant source of stress concentrating flaws (e.g. Eberhardt et al., 1999). With increasing degradation, the coalescence of individual fractures results in a pervasive fracture network where a sudden increase in permeability can be observed. The mathematical theory that considers the influence of connectivity on the conductivity is the so-called "percolation theory" (Stauffer & Aharony, 1994). Below a certain percolation threshold, the influence of the hydraulic conductivity of individual fractures on the integral permeability is negligible because a continuous path for fluid flow does not exist (e.g. Robinson, 1983; Long & Witherspoon, 1985; Berkowitz, 1995). Fracture density appears to be the most important factor in controlling the connectivity of fractures (Zhang & Sanderson, 2002). The percolation theory is also applicable when describing the hydraulic behavior of the EDZ in rock salt (Popp et al., 2001; Alkan & Müller, 2008). The microstructural damage occurring in the EDZ can therefore compromise the integral sealing function of the barrier, even though the barrier itself can be regarded as intact.

To verify the substantial and reliable sealing of the EDZ as required by the safety concept, the hydraulic behavior of the EDZ should initially be assessed. The rheological behavior of rock salt around backfilled man-made openings leads to sealing and healing mechanisms that can decrease the permeability over time (e.g. Senseny et al., 1992; Hunsche & Hampel, 1999; Schulze et al., 2001). The sealing processes are stress-dependent and strongly driven by the increasing confinement due to creep. Thus, the effect of sealing processes on the permeability of rock salt can be simulated and evaluated using the conventional fluid pressure criterion or a permeability-effective stress function proposed by Müller-Hoeppe et al. (2014). However, the rates at which healing processes take place and their impacts on the permeability are not quantified (Wieczorek & Schwarzianeck, 2004). Therefore, injection of liquid silica is considered additionally as a sealing technique of microfractures in order to meet the requirement of the sealing function of a technical barrier (Müller-Hoeppe & Schmidt, 2015).

However, many methods used to describe the mechanical processes inside the EDZ are based on continuum mechanical approaches where the damage is considered as an isotropic property (Hampel et al., 2012). Tsang et al. (2005) identified several aspects that need to be addressed to enhance the understanding of the EDZ and the modeling techniques to simulate its behavior. An area of significant weakness in EDZ studies is that of anisotropy. Boundary conditions and rock properties, such as in-situ stresses, fracture networks or induced permeability changes caused by drift construction are anisotropic and the interaction of these properties and their behavior are an open question (Tsang et al., 2005). There have been some efforts where the damage in the EDZ in rock salt is assumed to be anisotropic (e.g. Missal et al., 2015). However, the interaction between damage and permeability cannot be studied explicitly since the solutions are based on continuum approaches where both properties are simply linked by empirical functions. In order to further investigate the initiation, propagation and interaction of fractures, it is necessary to characterize the mechanical and hydraulic behavior at grain scale where fracture connectivity and permeability can be investigated explicitly. Therefore, to explicitly simulate the EDZ, a continuum-based approach is only suitable to a limited extent.

The objective of this investigation is determined by the need to develop a modeling strategy that can be applied to simulate the permeability increase due to mechanical deterioration of rock salt, in particular that occurring in the EDZ. In order to simulate the shape and arrangement of crystal grains in rock salt, discontinuum approaches were applied in the first phase of the project (Bollingerfehr et al., 2011). The discrete element method is widely accepted as a suitable tool for analyzing the fracture and damage behavior (Jing & Stephansson, 2007). The capability of the discrete element method to simulate the EDZ has already been demonstrated in the literature (Lisjak et al., 2014). To expand the approach to three dimensions and to allow a more realistic shape of the discrete elements used, the distinct element code 3DEC was used. The polyhedral-shaped discrete elements, which were used here, are called Voronoi polyhedra.

However, a complete model-based simulation of both the fracture system of the EDZ and the injection process was not realized in the first phase of the project VerA (FKZ 02E10649; Bollingerfehr et al., 2011). It was shown that the mechanical behavior, especially the fracture development, does not fully correspond to laboratory experiments and, thus, needs further research (Müller et al., 2012). It also became clear that the simulation of the entire EDZ is beyond practical application when using discontinuum approaches. Information derived from microstructural modeling must be transferred to the macroscale. Therefore, in the second phase of the project, great importance was attached to improve the mechanical behavior of the model at grain scale, to generate a realistic fracture system of the EDZ and to upscale the information derived from discontinuum approaches to the macroscale.

The second chapter deals with the representation of rock salt at grain scale using polyhedral elements (Fig. 1). It therefore constitutes the basis for the subsequent generation of fracture systems occurring in the EDZ. In the first phase of the project it was shown that standard laboratory tests, e.g. compression tests, are only applicable to provide information about the macroscopic deformation behavior. Knowledge about the controlling fracture processes occurring at grain scale cannot be obtained. Therefore, the validation of the simulation results,

especially of the fracturing, is only suitable to a limited extent. For this purpose, laboratory tests were conducted both to derive material parameters used in the constitutive models and to validate the simulated fracture network at grain scale. Combined acoustic emission and uniaxial compression tests as well as microstructural analyses were carried out to dissolve the macroscopic behavior micromechanically. Since the microstructure can have an influence on the fracture development, it is also verified how well the typical shape and arrangement of rock salt grains is simulated by Voronoi polygons. Moreover, the Voronoi pattern was geometrically improved to enhance both the numerical stability and the runtime of the simulation.

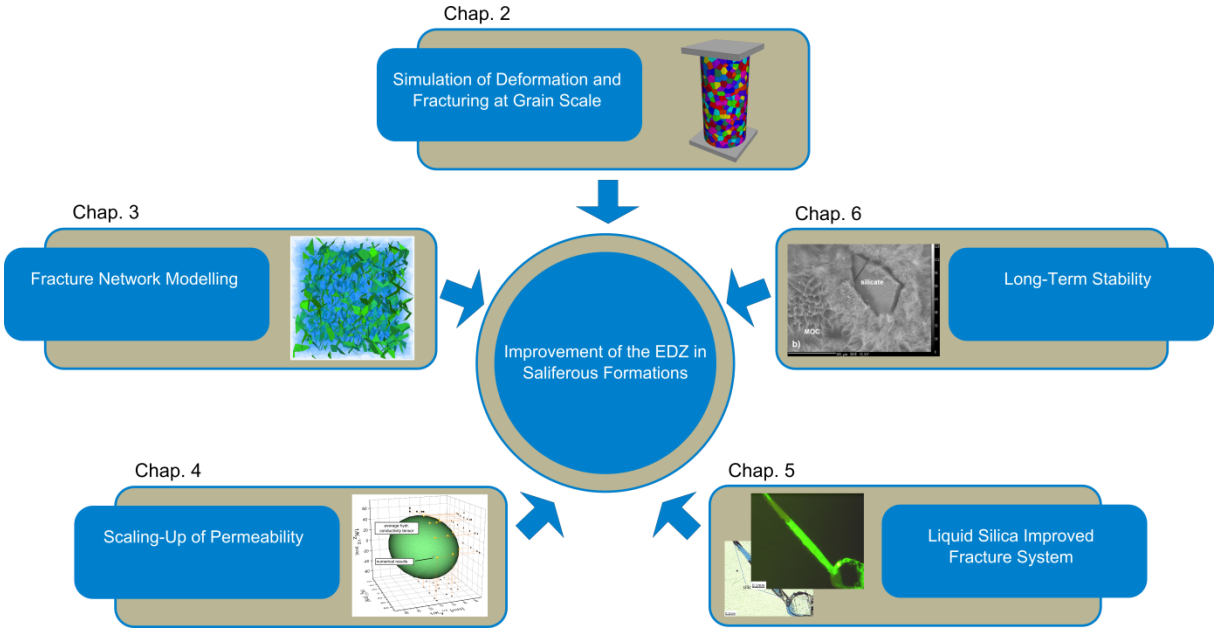

Fig. 1: Structure of this report

Chapter three describes the generation of realistic fracture networks occurring in the EDZ using the discontinuum approach and polyhedral elements. For this purpose, the excavation of a drift is simulated with continuum mechanical approaches and the zone stresses are recorded in certain parts and for certain depths of the EDZ. The zone stresses are then transmitted as boundary stresses on a discontinuum model that comprises polyhedral elements to simulate the fracture development at grain scale. The fracture network generated this way should be comparable to those observed in the EDZ.

The fourth chapter introduces a method to upscale the information gained from discontinuum modeling to the macroscale. As discussed earlier, the permeability increase in the EDZ is mainly caused by micro fractures, which can compromise the sealing function of the original tight rock salt. Therefore, the specification of adequate permeability values is mandatory for the accurate simulation of the injection process. The method used for upscaling is based on the following principles: the fluid flow of a discontinuum model with fractures explicitly represented is similar to that of a continuum model having equivalent hydraulic properties. For this purpose, the hydraulic conductivity tensor was investigated by simulating the flow through a discontinuum model under different hydraulic head directions. This allows the specification of

directionally dependent (anisotropic) permeability properties that can be used as input parameters for large-scale modeling.

In chapter five the modeling strategy is complemented by investigations on a liquid silica improved fracture system. In the first phase of the project, in situ experiments were conducted in order to verify the sealing injection technique using liquid silica. Once the work was completed and after a waiting period of three months, samples (drill cores) were taken from the injected host rock, and thin sections were prepared to inspect the fracture system microscopically.

Chapter six is about studies to characterize the long-term stability of liquid silica improved rock salt samples. A laboratory research program was conducted during the first phase of the project which considers an injection of rock salt with sodium silicate solution. The influence of the contact with NaCl and $MgCl_2$ solutions on the mineral content and the composition of the solutions were investigated. These studies have been completed by analyzing the solubility of amorphous silica in saturated NaCl solutions with $MgCl_2$ of varying concentration. Additionally, it was tested whether amorphous silica is able to act as a chemical barrier by analyzing the reaction behavior of selected trace elements in contact with amorphous silica.

2 Mechanical Simulation of Rock Salt at Grain Scale

Rock salt consists of individual grains which are connected by grain boundaries forming a polycrystalline microstructure. Local stress changes adjacent to man-made openings result in microcracking and granular disintegration during and after excavation. Although it results in a macroscopic deformation, the relevant processes that induce an excavation damage zone (EDZ) occur at the scale of the microstructure. The macroscopic mechanical characteristic of a polycrystalline material is influenced by the mechanical behavior of single crystals as well as the geometric organization (fabric) of the crystals forming the microstructure. The mechanical behavior of single crystals includes the deformation of grains and their boundaries whereas the fabric includes their arrangement, size and shape.

In order to simulate individual grains, the Discrete Element Method (DEM) was used. The DEM is widely accepted as an appropriate tool for analyzing the fracture and damage behavior of rocks at the microscopic level (Lisjak & Grasselli, 2014). The geometric properties of the grains were simulated by using polyhedral elements based on a Voronoi tessellation. The polyhedral elements are internally deformable and the bonds between the polyhedral elements can be configured to simulate the deformation behavior of grain boundaries. In general, the material properties of rock salt have to be described within numerical modeling by using appropriate constitutive models. In the past, a series of suitable constitutive models have been developed to simulate the mechanical behavior adequately (Hampel et al., 2012; Salzer et al., 2012). However, these models are adapted for continuum mechanical approaches, where the sum of deformation processes is simply homogenized over the volume and thus is averaged out. When using the DEM, this homogenization approach is not applicable. The DEM subdivides the volume into smaller elements and thus describes a discontinuous distribution of rock salt grains at the microscopic level. Thus, it is necessary to distinguish between the physical processes occurring within and between the salt grains.

The following chapter outlines the generation of Voronoi polygons (chap. 2.1). The objective is to verify how well the crystalline microstructure is simulated by Voronoi polygons and to enhance the numerical stability by a geometrical improvement of the Voronoi pattern. Subsequently, the controlling processes for mechanical deterioration of rock salt at grain scale are illustrated (chap. 2.2). In the final chapter, the material parameters used in the constitutive models to reproduce the microfracturing (chap. 2.3) are identified. The deformation behavior and the fracturing processes of the numerical models are analyzed and compared to laboratory tests.

2.1 Using the Voronoi Tesselation to Reconstruct the Microstructure

The DEM describes a discontinuous distribution of grains at the microscopic level. Thus, a first step is the accurate construction of a representative microstructure for grain scale modeling. The experimental characterization of microstructures is generally based on image analysis on two-dimensional thin sections (Heilbronner & Barrett, 2013). The advantage is the fast and easy handling, but some quantities cannot be considered adequately by classical methods that use two-dimensional images (Uchic, 2011). Recently, new measurement

techniques such as Electron Backscattered Diffraction (EBSD) play an important role for grain scale modeling (Brahme et al., 2006; Rollett et al., 2007). A major advantage is the exact representation of complex microstructures. However, the characterization of larger and more complex microstructures is usually very time-consuming and expensive (Quey et al., 2011).

The information coming from experimental characterization is used to reconstruct a microstructure for numerical modeling. The reconstruction and generation is generally based on deterministic or stochastical approaches. Deterministic approaches use the image information gained from thin sections directly to transfer the microstructure onto a grid, e.g. using the mesh of a Finite Element Method (FEM) model (e.g. Barbe et al., 2001) or discrete elements using the DEM (e.g. Wichert et al., 2014). Stochastic approaches use statistical data from experimental characterization to randomly generate grains with representative sizes and shapes. Especially randomly generated particles, based on the Voronoi tessellation, are in the spotlight of scientific interest (e.g. Zhang et al., 2002; Christianson et al., 2006; Herbst et al., 2008; Kazerani & Zhao, 2010; Müller et al., 2012; Asahina et al., 2012; Knauth et al., 2014). A major advantage of the Voronoi tessellation is the grain shape variability, which is representative for polycrystalline rock samples (Quey et al., 2011). Since rock salt consists of individual grains that are connected by grain boundaries forming a polycrystalline microstructure, the Voronoi tessellation was considered as a suitable microstructure for modeling.

Since a simplification to two dimensional models constitutes an improper solution, particularly with regard to the complex fracture system, a three-dimensional computation of the Voronoi tessellation was considered. In order to generate Voronoi polyhedral, the software library GrainGen was used in the first phase of the project (Walter et al., 2010). A Voronoi diagram is a partitioning of a space into discrete, polyhedral-shaped elements, so called Voronoi elements. The partitioning is based on points in space, and each point has a corresponding region consisting of all points closer to the point than to any other. The library GrainGen is based on a Laguerre geometry (also referred to as power or radical tessellation) that uses spheres with different radii rather than points. It is therefore defined as a weighted Voronoi tessellation. The center points of the spheres build up the point process and certain radii values for the spheres are the weights for the center-point process (Herbst et al., 2008). Since the underlying sphere packing influences the size of the resulting polyhedra, GrainGen is suitable to generate models with specified grain size distributions (Walter et al., 2009). However, it turned out that the generated Voronoi geometry behaves numerically unstable due to small polyhedral edges leading to bad-quality zone elements (Bollingerfehr et al., 2011). Small zones are very responsive to deformation, so that removing small edges can prevent the generation of degenerated zones. Moreover, the zone quality controls the critical time step for calculation, and optimization can decrease the calculation time (Itasca, 2013). It was therefore considered whether alternative libraries provide more appropriate Voronoi geometries.

The first alternative considered is Voro++, an open source software library proposed by (Rycroft, 2009). Voro++ is also based on sphere packings so that direct comparison with GrainGen is possible. The Voro++ object-oriented C++ code was modified to allow the generation of a readable input for the solver Itasca 3DEC used in this study (Itasca, 2013).

Subsequently, a sphere packing was created with Itasca PFC3D that served as a basis for the Voronoi generation process for both GrainGen and Voro++. It turned out that both codes provide identical geometries and are supposedly based on the same mathematical and algorithmic concepts. Consequently, a different approach was considered, where the geometry is optimized after generation. The large-scale 3D random polycrystal generator Neper proposed by Quey et al. (2011) additionally allows the removal of small entities (edges and faces). Neper removes small edges with a length that is below a given threshold value. Deleting a small edge means replacing it and its two connected vertices with a single vertex. However, this leads to some topological modifications of the polyhedral surfaces involved. The new vertex has a position that is different from those of its parent vertices, and as a consequence does not lie within the initial planes of its faces (Quey et al., 2011). In order to test the geometry regularization, several Voronoi models with different threshold values (fmax 0, 0.5 and 25) were generated und discretized by 3DEC using the build-in tetrahedral zone generation. For evaluation, the distribution of zone volumes obtained after geometry regularization is given in Fig. 2. As the threshold value is increased, more small edges are deleted by the geometry regularization algorithm of Neper. As a consequence, it becomes easier for the tetrahedral mesh generator to generate larger zones.

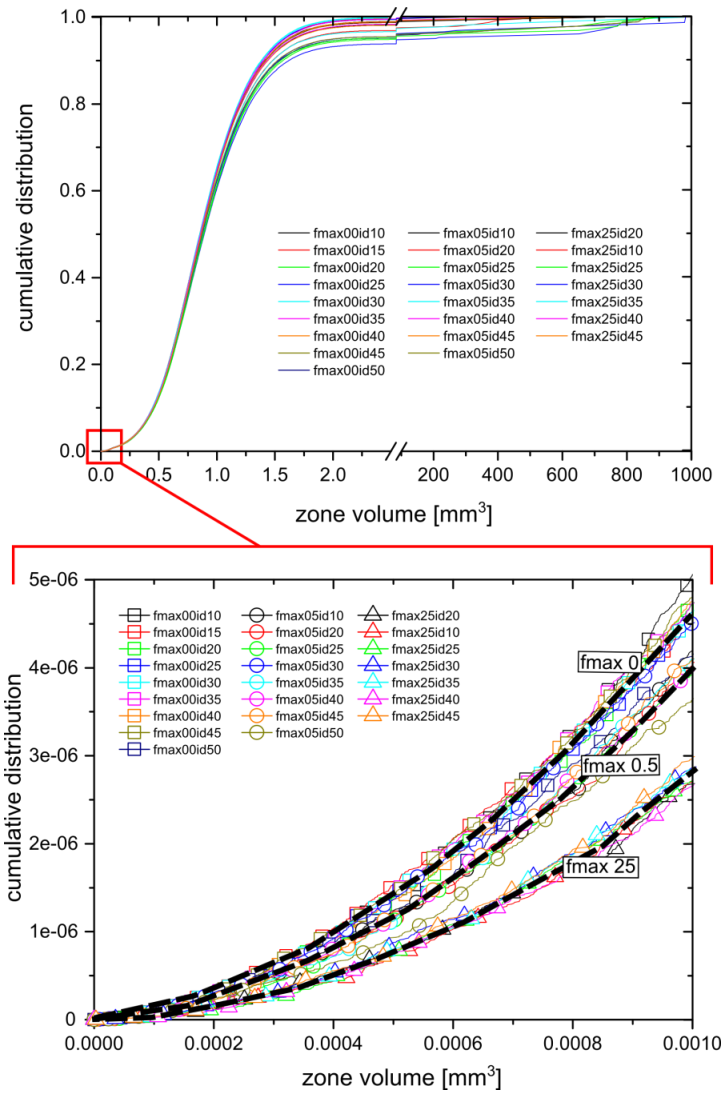

Fig. 2: Zone volume distribution of the Voronoi tesselation as the cumulative frequency curve generated from zone counts of different volumes.

However, 3DEC appears very sensitive to the topological modifications due to the geometry regularization. Because a polyhedron must necessarily be formed by planar faces in 3DEC, the distortion of the polyhedral surface causes problems when importing the optimized Voronoi tessellation. Therefore, the given threshold value should be selected carefully. A threshold value of fmax 0.5 was considered to be suitable. This way, geometrically improved Voronoi models could be generated for the application in 3DEC. It is therefore primarily used for Voronoi generation within this work.

Calibration of the Voronoi models is usually performed by comparing numerical results with those obtained by laboratory results (see Chap. 2.3). An important objective of this strategy is to adjust the macroscopic stress-strain relationship as well as the small-scale fracturing. However, it is known that the shape and arrangement of grains can strongly influence the fracture and damage behavior of rocks (e.g. Lan et al., 2010). Thus, to avoid that the Voronoi models are a source of error, the generated microstructure must correspond as closely as possible to the microstructure to be analyzed in the laboratory.

The comparison of real and simulated microstructures is based on quantitative image analysis of thin sections of rock salt. Cylindrical rock salt samples of the z3 Formation (z3BK/BD) were selected for analysis. Image based analysis was carried out in collaboration with the University of Göttingen (Geoscience Centre, Müller & Leiss, 2013). Three thin sections (75 x 110 mm) were cut perpendicular to each other to allow a comparison with the three-dimensional Voronoi pattern and are oriented along the cylindrical axis. Visual study of the thin sections was done using a petroscope (MAP, ADC-3L) and by tracing the grain boundaries. Then, ImageJ 1.47t (Wayne Rasband) was used for the quantitative analysis by determining typical microstructural features, e.g. shape, size, and orientation of grains. Fig. 3 shows the three thin section images and the grain boundaries traced. It was not always possible to determine the grains' contours adequately due to non-traceable boundaries (larger open areas between grains). However, 724 grains in thin section A, 795 grains in thin section B and 570 grains in thin section C could be recorded and analyzed.

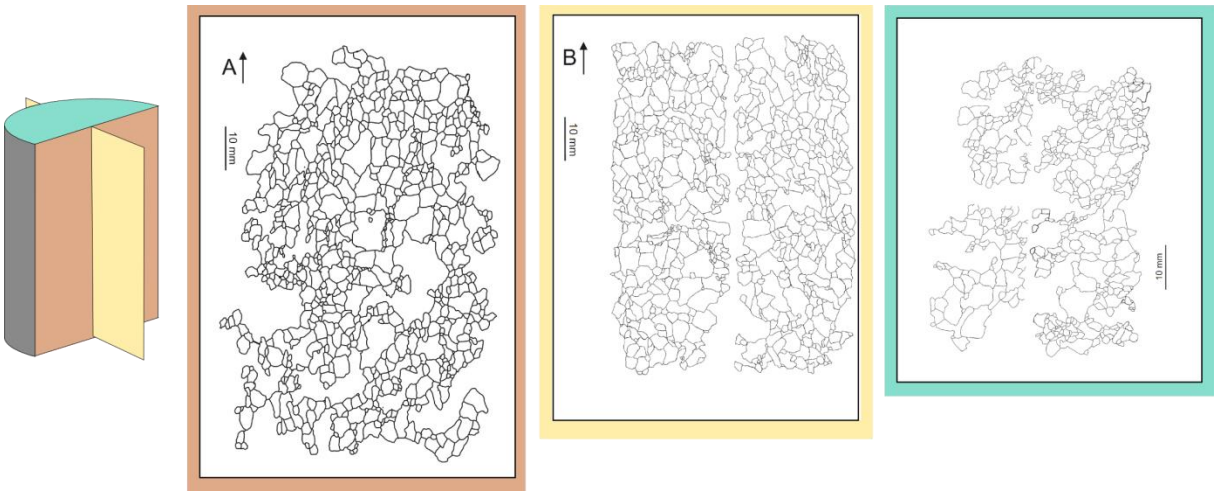

Fig. 3: **Microstructure of rock salt.**

To allow a comparison of the rock salt microstructure with the stochastic microstructure, a cube with an edge length of 10 cm and 15625 elements was generated using the Voronoi algorithm Neper (Quey et al., 2011), which results in an average Voronoi element edge length of approximately 4 mm. Slices were cut along the principle directions und analyzed in the same manner as the real rock samples using ImageJ. 521, 494 and 522 Voronoi elements were analyzed in the x, y and z direction, respectively (Fig. 4)

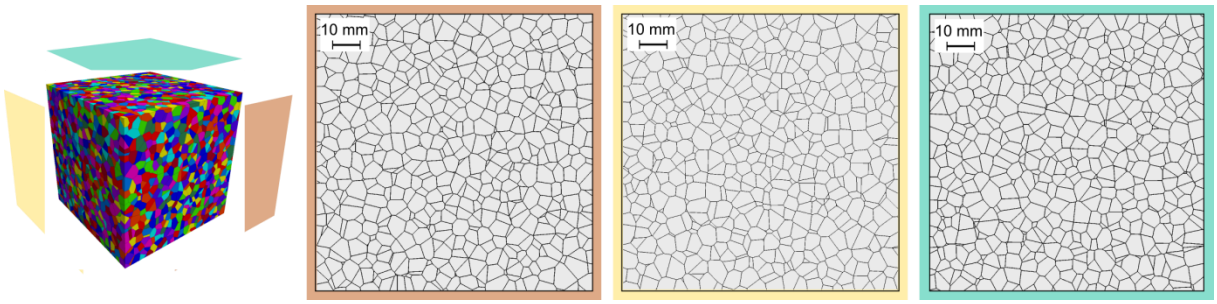

Fig. 4: **Voronoi microstructure used for grain scale modeling.**

Grain size is the dominant microstructure feature of polycrystalline materials. The diameter of particles is usually based on a certain equivalency criterion und must thus be clearly defined by the measuring procedure. In this work, the surface-equivalent sphere diameter was used, which is given as the diameter of a sphere having the same area as the particle:

$$d_{area} = \sqrt{\frac{4A}{\pi}} \quad (1)$$

The grain size distribution is similar for each thin section and can be fitted to a lognormal distribution (Fig. 5). The grain sizes range from 0.5 to 11 mm. An averaged diameter of 1.8 mm can be specified for rock salt thin section A, 2.0 mm for thin section B and 1.9 mm for thin section C. Approximately 70% of the grains (particle number) have an average diameter of less than 3 mm. The smaller particles represent recrystallized grains along grain boundaries or eventually healed cracks (Müller & Leiss, 2013). Compared to this, the Voronoi microstructure shows element sizes ranging from 0.5 to 8 mm. Approximately 70% of the Voronoi elements have sizes between 4 and 6 mm. An average element diameter of 4.5 mm can be specified. In addition to the grain size distribution, the grain area distribution was evaluated as well. Although the smaller salt grains dominate numerically, grains larger than 4 mm constitute a high proportion of the total surface area due to the wider particle size distribution with grain sizes up to 12 mm (Fig. 6). The Voronoi elements show a considerably lower dispersion about the mean. The major part of the total area of the Voronoi microstructure is made up of elements with a diameter between 4 and 6 mm.

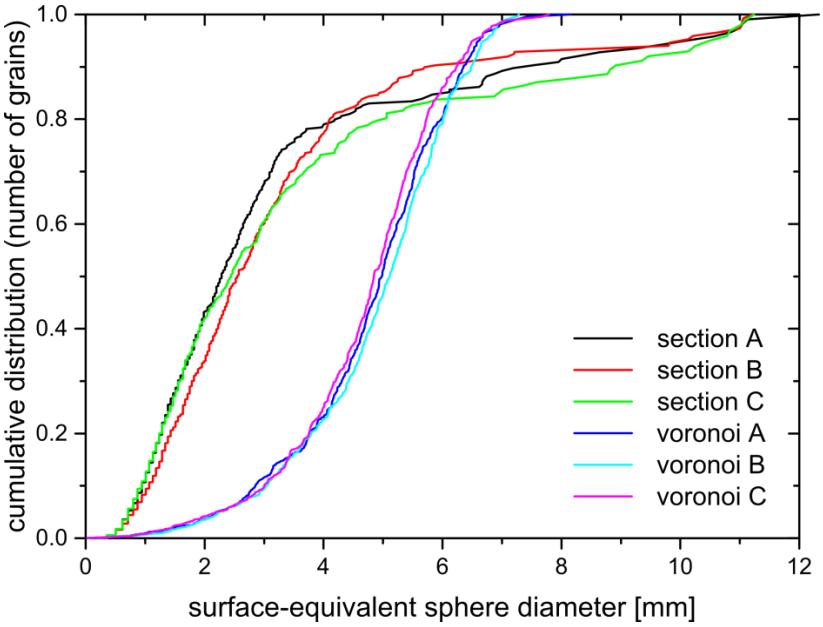

Fig. 5: Grain size distribution of rock salt and Voronoi tesselation as the cumulative frequency curve generated from particle counts of different sizes.

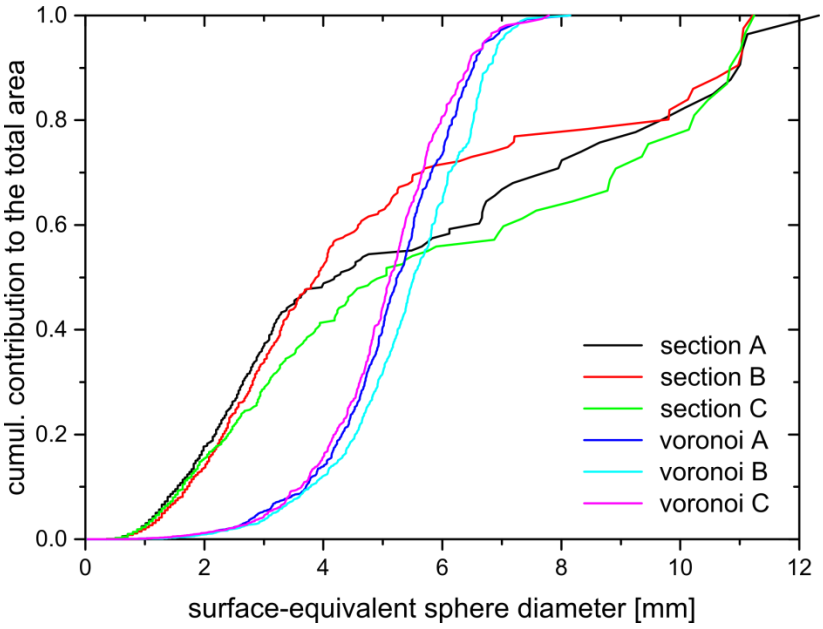

Fig. 6: Contribution of grains with different sizes to the total area as the cumulative frequency curve generated from particle counts of different surface areas.

The shape of the grains was characterized by measuring the sphericity, the length-to-width ratio (aspect ratio) and the orientation of the longest grain length. The sphericity after (Wadell, 1935) is a measure of how spherical a body is. It represents the ratio of the surface of a sphere of equal volume to the surface of the body according to the relationship:

$$SPHT = \frac{4\pi A}{U^2} \quad (2)$$

An ideal sphere results in a value of 1, for all irregular shaped bodies a value <1 is calculated (e.g. square 0.89). Nearly 70% of both the salt grains and the Voronoi elements show a sphericity between 0.6 and 1.0 (Fig. 7). The length-to-width ratio was examined analogously to sphericity (Fig. 8). The results show that 70% of the grains have a ratio between 1 and 2.

However, it should be taken into account that many grains approximate a rectangular or diamond shaped form. Although a hexagon is assumed as isotropic, a long-axis along the diagonal line and a short-axis between the edges can be measured. Therefore, a fake shape anisotropy can be measured but its relevance is negligible with respect to microstructure mechanisms.

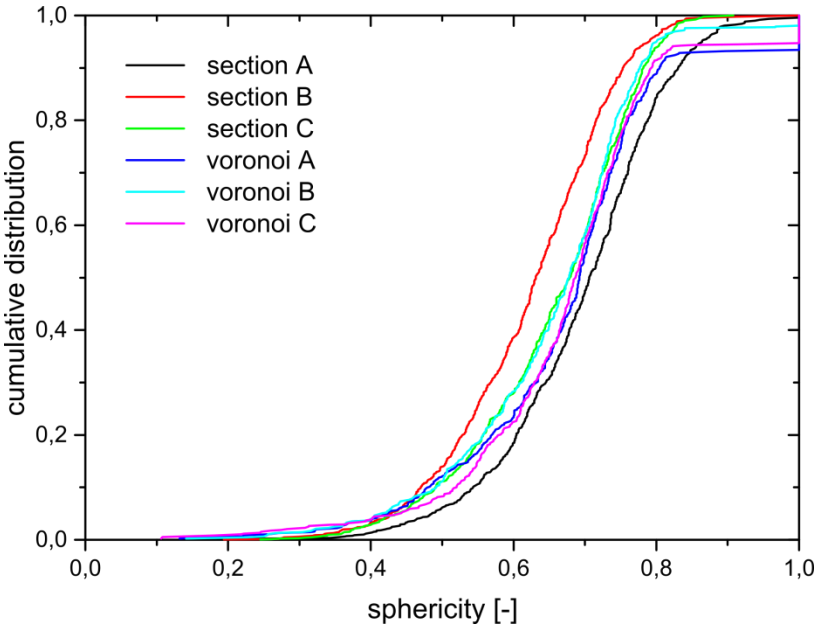

Fig. 7: Cumulative frequency curve generated from particle counts of different sphericities.

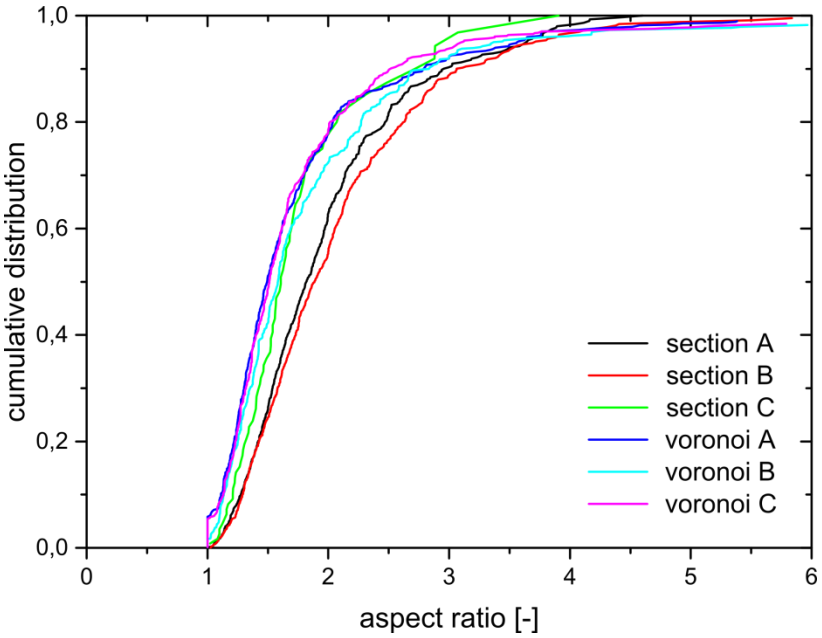

Fig. 8: Cumulative frequency curve generated from particle counts of different width-length ratios (aspect ratio).

The orientation of the grains was specified by measuring the angle between the longest grain length and the cylinder axis (z-direction). The frequency distribution of the angles leads to the so-called rose-diagram (Fig. 9). Thin sections A and B show a long-axis with preferred orientation parallel to the sample cylinder axis due to deformation mechanisms occurring in the natural rock salt investigated. This directional anisotropy in terms of the particle shape is slightly visible at the traced grain boundaries (Fig. 3). The Voronoi microstructure shows no preferred orientation and can therefore be assumed to be isotropic.

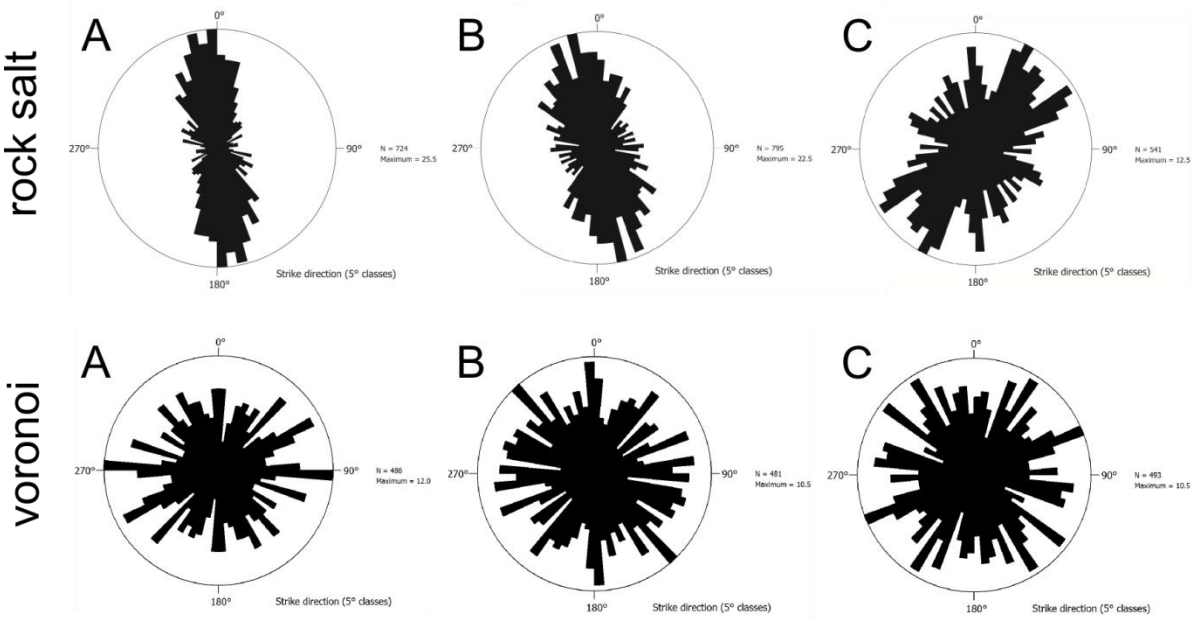

Fig. 9: **Direction distribution measuring the angle between the longest grain length and the cylinder axis for rock salt and Voronoi elements.**

2.2 How Cracks Are Formed in Rock Salt

The DEM subdivides the volume into smaller elements and thus describes a discontinuous distribution of rock salt grains at the microscopic level. In order to adequately describe the mechanical behavior of rock salt, the physical processes occurring within and between the salt grains have to be simulated by suitable constitutive models.

The deformation behavior of rock salt is characterized by a series of processes. The following processes and properties are considered as essential (Hampel et al., 2007):

- linear elasticity under low stress condition
- evolution of dilatancy, which is associated with microstructural deterioration and increased permeability
- primary and secondary creep, which are caused both by strain hardening with increasing stress (dislocation glide) and recovery processes due to relief of internal stresses after long time periods (dislocation creep)
- tertiary creep, which is linked to damage processes above the dilatancy boundary
- short-term compressive strength at high loading rates and long-term strength as a result of creep failure
- peak strength and residual strength

Particularly emphasis is given to the development of microstructural damage along grain boundaries occurring in the EDZ. The EDZ is formed immediately after excavation due to local stress changes. Assuming that time-dependent creep (dislocation creep) has no impact on the formation of the EDZ, only short-term deformation processes must be taken into account, i.e., evolution of dilatancy due to microstructural deterioration, primary creep caused by strain hardening (dislocation glide), short-term laboratory compressive strength, and residual strength above the peak strength.

Initially, simple constitutive equations were considered to be suitable for the purpose of simulating the controlling deformation processes (Bollingerfehr et al., 2011). The elastic behavior was described by a linear-elastic constitutive model. Because of the nature of the discrete element method, the elastic behavior is governed both by the deformability of the polyhedral-shaped elements and the grain boundaries. Plastic dilatancy due to grain-boundary cracking (intercrystalline deformation) was simulated by using the Mohr Coulomb elasto-plastic criterion including a tensions cut-off condition. To simulate the deformation within the salt grains (intracrystalline deformation), a continuum-based Mohr Coulomb criterion with an additional strain hardening approach was used. The shear yield function is non-associated, and the tensile flow rule is associated. The strain hardening of rock salt is mainly produced due to an accumulation of dislocations, which can be regarded as time-independent plastic deformation. With increasing dislocation density and resulting increase if interactions between both free dislocations within each glide plane and different glide planes, they can constrain each other in their development. As a consequence, a larger yield stress is required to maintain plastic deformation. Since the structure of the salt crystal is not modified by these processes, a crack-free and constant-volume deformation is assumed. Thus, the dilation angle was reduced to zero in the shear potential function and the tensile strength was increased to inhibit tensile failure.

However, it already became clear in the first phase of the project that the stress-strain relationship corresponds quite well to laboratory experiments, but that the micromechanical damage development needs further research. Based on the results, it was concluded that both intra- and intercrystalline deformation are related to each other (Müller et al., 2012). Bourcier et al. (2012) could visualize the cooperative nature of both mechanisms and highlight their close relationship with local microstructure. With the help of microstructure analysis it was shown that incompatibilities in the plastic deformation of adjacent crystal grains cause local stresses at the grain boundaries, which lead to the formation of intergranular microcracks (Bourcier et al., 2012). In order to verify how this behavior can be described by appropriate constitutive models, the description of the controlling processes with special consideration of the microstructure is a first essential step.

Sodium chloride crystallizes in a cubic lattice (face-centered cubic lattice, fcc). The unit cell is composed of three equally long axes arranged at 90 degrees to each other. Along the three axes of a unit cell an alternating arrangement of sodium and chloride ions can be recognized. Each sodium ion is octahedrally surrounded by six chloride ions and *vice versa* (Fig. 10).

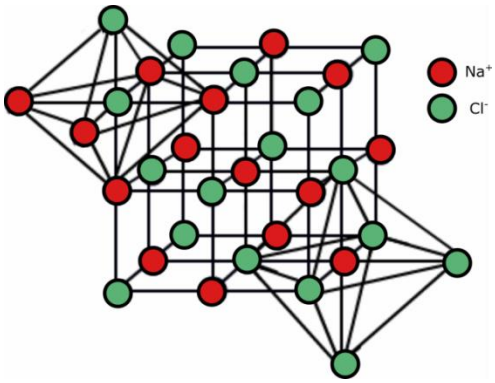

Fig. 10: Cubic lattice of sodium chloride.

With respect to the elastic properties, three independent constants were obtained for the face-centered cubic lattice (C_{11}, C_{12}, C_{44}). In contrast to isotropic materials that have only two independent constants, sodium chloride has direction-dependent elastic constants (orthotropic material). The elasticity tensor C can be represented as follows:

$$\begin{bmatrix}\sigma_1\\ \sigma_2\\ \sigma_3\\ \sigma_4\\ \sigma_5\\ \sigma_6\end{bmatrix} = \begin{bmatrix} c_{11} & c_{12} & c_{12} & \cdot & \cdot & \cdot \\ c_{12} & c_{11} & c_{12} & \cdot & \cdot & \cdot \\ c_{12} & c_{12} & c_{11} & \cdot & \cdot & \cdot \\ \cdot & \cdot & \cdot & c_{44} & \cdot & \cdot \\ \cdot & \cdot & \cdot & \cdot & c_{44} & \cdot \\ \cdot & \cdot & \cdot & \cdot & \cdot & c_{44} \end{bmatrix} \begin{bmatrix}\varepsilon_1\\ \varepsilon_2\\ \varepsilon_3\\ \varepsilon_4\\ \varepsilon_5\\ \varepsilon_6\end{bmatrix} \quad \textbf{(3)}$$

For sodium chloride the following values are derived from literature: C_{11}=49,1GPa, C_{11}=12,7GPa and C_{11}=14,0GPa (Gebrande & Kern, 1982).

In contrast to elasticity, the plastic deformation is irreversible. The reasons are slip mechanisms, which cause atomic planes to slip according to the crystal lattice. A critical resolved shear stress is required to initiate a slip. The shear stress on slip plane and slip direction can be determined by Schmidt's Law (Fig. 11):

$$\tau = b_i n_j \sigma_{ij} = m_{ij}\sigma_{ij} \quad \textbf{(4)}$$

where n_j is the unit vector of the slip plane and b_i denotes the slip direction. The outer product $b_i \otimes n_j$ is the so-called Schmidt tensor m_{ij}.

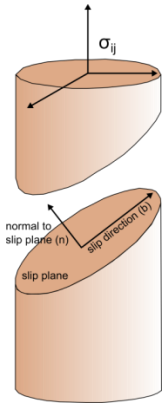

Fig. 11: Geometric relationship for calculating the shear stress on a shear plane using the normal to the slip plane n and the slip direction b.

The planes and directions are usually defined using the Miller indices, where the notation *(hkl)* denotes the planes and the notation *[uvw]* denotes the direction. Depending on the crystal system, a particular coordinate system is used as a basis. The cubic lattice is based on a Cartesian coordinate system. In the context of crystal planes, the three integers denote a plane orthogonal to a direction (hkl) in the basis of the reciprocal lattice vectors. Negative vectors are written with a bar. Due to crystallographic reasons, certain slip planes are equivalent in the crystal, which is expressed by the notation {hkl}. As an example, the notation {100} denotes the set of all planes that are equivalent to each other due to the symmetry of the lattice, i.e., (100), ($\bar{1}$00), (010), (0$\bar{1}$0), (001) and (00$\bar{1}$). They correspond to the surface of a cube (Fig. 12). Similar to equivalent slip directions, the notation <uvw> is used.

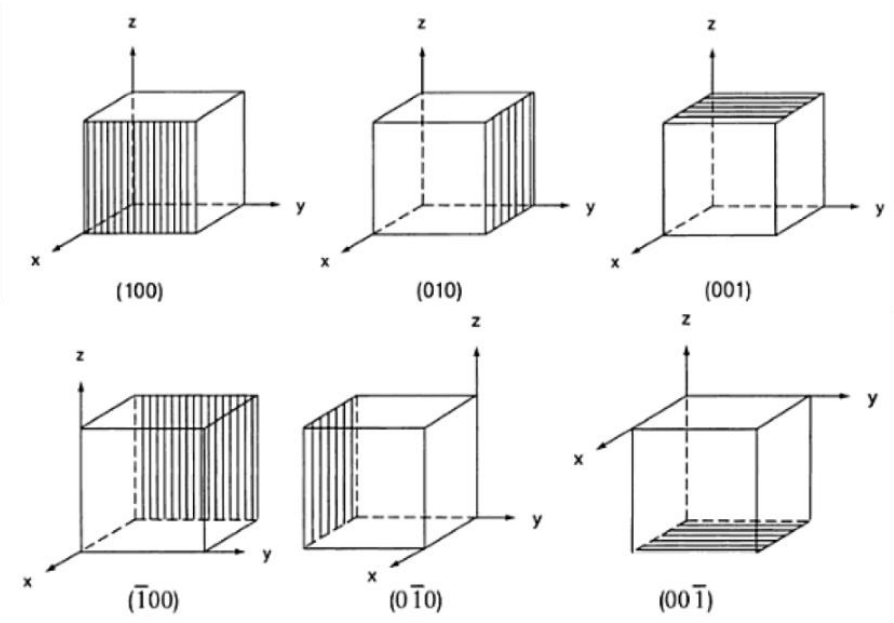

Fig. 12: **Miller indices of the planes {100} in a cubic lattice (modified after Kanani (2006)).**

Slip planes generally represent close-packed lattice planes (greatest number of atoms per area), and the direction occurs in close-packed lattice lines (Kleber et al., 2010). Because planes of type {111} and directions of type <1$\bar{1}$0> are along the close packed plane, they usually form the slip system in a face-centered cubic crystal (Rösler et al., 2008). For ionic crystals such as sodium chloride, however, more complicated conditions exist because similarly charged ions are not allowed to touch each other during slipping (Karato, 2008). Although the (100) lattice planes represent the close packed planes in sodium chloride, translation occurs predominantly on {110} planes towards <1$\bar{1}$0>. {100}<110> and {111}<1$\bar{1}$0> were specified as secondary slip systems (Tammann & Salge, 1927; Buerger, 1930). At room temperature, however, much higher stresses are required for the secondary slip system than for the activation of the primary slip system (Fig. 13a). Thus, at temperatures up to 200°C, slip mechanisms take place primarily on {110}<1$\bar{1}$0> (Kelly & Knowles, 2012). However, laboratory results show that the yield stress of polycrystals (aggregate of crystalline grains) is significantly higher than in the case of single crystals with the primary

slip system {110}<1$\bar{1}$0> (Fig. 13b). Thus, the plastic strain of polycrystalline rock salt cannot be fully covered by the primary slip system.

This observation is closely related to the so-called Mises criterion (Mises, 1928). The criterion suggests that yielding of a polycrystalline material can only be achieved if each grain has the capability of homogeneous plastic deformation. A homogenous deformation is only possible if five displacement components (translations) being independent from each other operate in each grain. Independent means that a slip system cannot be described by the components of the other slip systems; they must be linearly independent of each other in a mathematical sense. The five translation systems (i.e. slip systems) can be obtained from the six components of the strain tensor (ε_{xx}, ε_{yy}, ε_{zz}, ε_{xy}, ε_{yz}, ε_{xz}) if the assumption of volume consistency (ε_{xx} + ε_{yy} + ε_{zz} = 0) occurring in a homogenous deformation is considered (Junker, 2000).

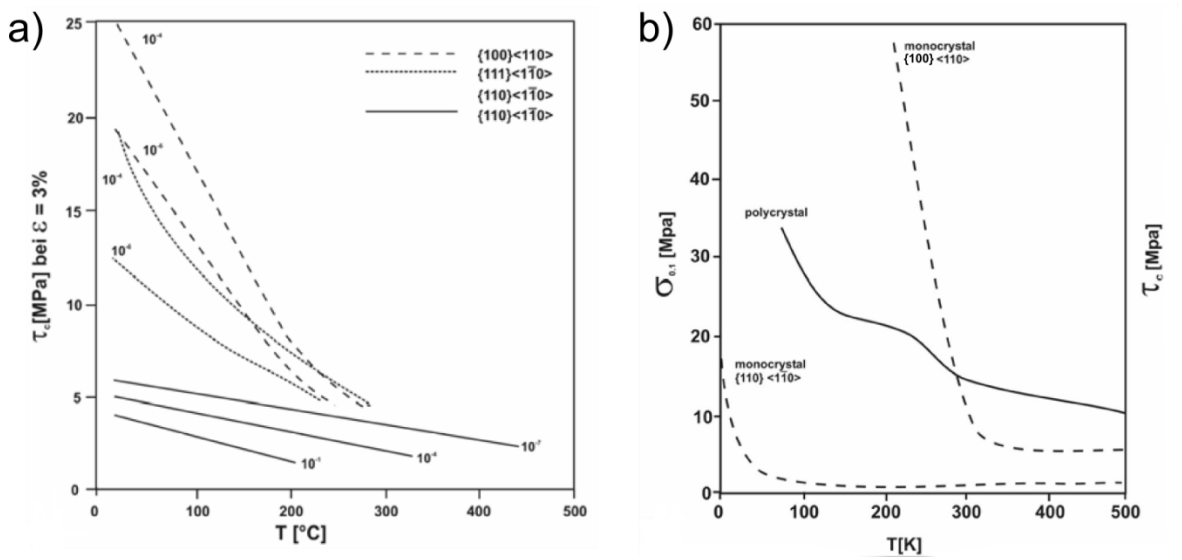

Fig. 13: **Critical shear stresses (a) for observed slip systems versus temperature (Carter & Heard, 1970) and shear stresses (b) for polycrystalline rock salt and monocrystalline rock salt for different slip systems after Skrotzki et al. (1981) (modified after Scheffzük (1999)).**

In rock salt, the primary slip system {110}<1$\bar{1}$0> has six crystallographically equivalent slip systems (rhombic dodecahedral slip system) as well as the slip system {100}<110> (cubic slip system) (Fig. 14). For the slip system {111}<1$\bar{1}$0> twelve translation system have been described (octahedron slip system).

However, in the primary slip system only two systems are independently developed, whereas the {100}<110> and {111}<1$\bar{1}$0> systems have three and five, respectively (Carter & Heard, 1970; Senseny et al., 1992). Because the {110}<1$\bar{1}$0> system is the dominant slip system at low temperatures but has only two independent translation system, secondary slip systems must be activated for a homogenous deformation of polycrystals. This results in higher yield stress of polycrystals in contrast to single crystals of type {110}<1$\bar{1}$0> as mentioned earlier (Fig. 13b). Moreover, the mandatory activation of five translation systems required for ho-

mogenous deformation leads to difficulties, especially when deformation takes place at low temperatures (Scheffzük, 1999).

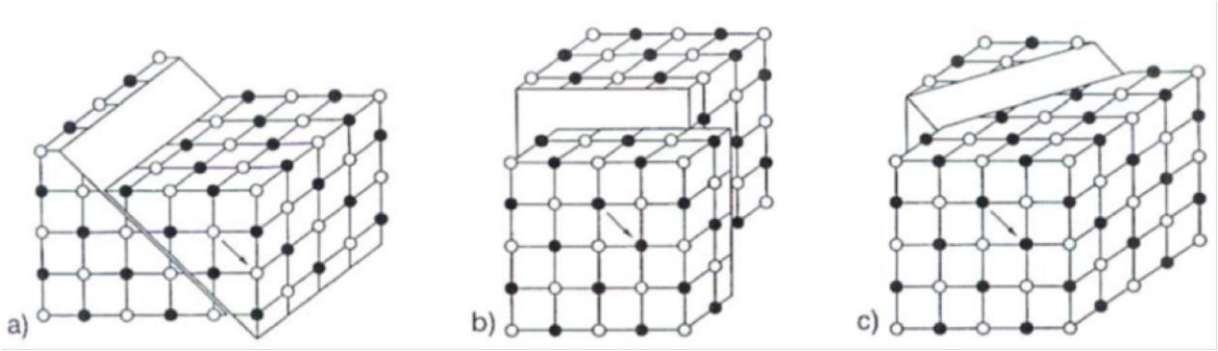

Fig. 14: **Slip systems in sodium chloride showing the slip direction (110) on the slip planes a) (110) (rhombic dodecahedral system), b) (100) (cubic system) and c) (111) (rhombic dodecahedral system) (Scheffzük, 1999).**

The Schmidt Law (4) demonstrates that slip system activation of a specific crystal largely depends on its location to the external applied stress. Assuming a material without a texture, slip planes and slip directions can change from one crystal to another. Thus, critical resolved shear stresses to initiate a slip may vary within a polycrystalline sample, and the crystal with the lowest critical shear stress yields first. With the help of microstructure analysis on rock salt, the activation of crystal plasticity due to slip bands and its contribution to the local interaction between neighboring grains was chronologically visualized by Bourcier et al. (2012). When crystal plasticity starts, the activation of slip bands is first limited to single grains due to their specific orientation to external stress (Fig. 15). With further loading, crystal plasticity intensifies within individual grains. Since crystal deformation takes place only on certain planes and in certain directions, local incompatibilities in the plastic deformation of adjacent crystal grains cause local stresses that induce cracking along grain boundaries (Bourcier et al., 2012). Cracking is to be expected when the stress to activate the required independent slip systems is higher than the cleavage stress (Skrotzki et al., 1981).

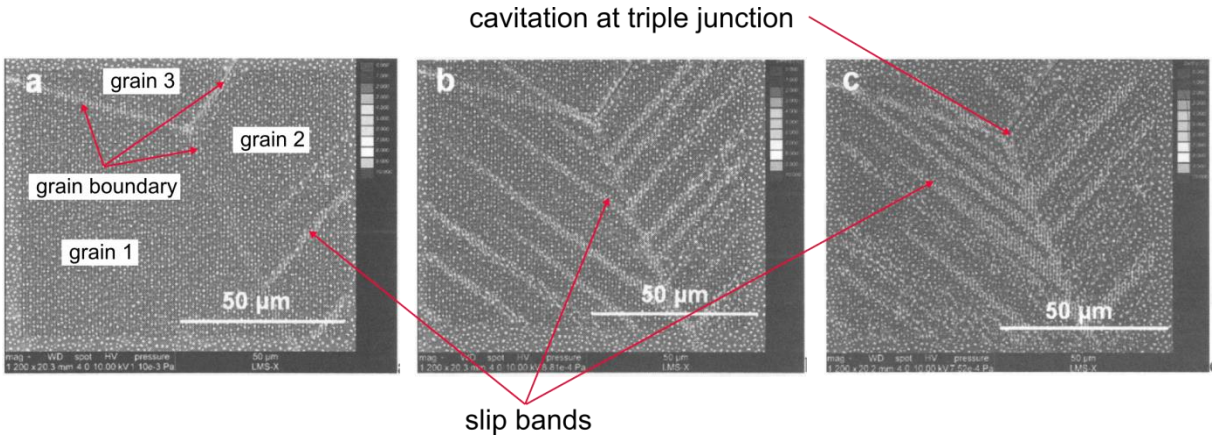

Fig. 15: **Representation of intergranular microcracking along grain boundaries due to incompatibilities in the plastic deformation of adjacent crystal grains. The stress condition was increased from left to right (modified after Bourcier et al. (2012)).**

When looking at the macroscopic sample, the anisotropic behavior of individual grains is averaged out due to the random distribution of crystallographic orientations. Therefore, the medium, particularly with regard to the finite strain, can be assumed to be quasi-isotropic when considering continuum mechanical approaches (Harder, 1997). However, when using the DEM, the grains and grain boundaries were explicitly simulated. Thus, in order to simulate the permeability increase due to mechanical deterioration along grain boundaries, anisotropic plastic deformation behavior of individual grains should be considered. Unfortunately, the DEM code 3DEC used in this study provides only a simple constitutive model for anisotropic deformation. The so-called ubiquitous model allows plastic deformation by defining weak planes of specific orientation using the Mohr-Coulomb criterion (Itasca, 2013). The implementation of additional planes as well as the restriction of slipping to a certain direction is not possible. However, the entirely new development of a suitable anisotropic model would go beyond the scope of this project due to the amount of time required for implementation. For this reason, the model used in the first phase of the project was optimized by a further parameter adjustment. The objective was to adjust the cooperative nature of crystal plasticity and cracking along grain boundaries due to a suitable parameter combination.

2.3 Model Calibration to Reproduce Fracturing

The DEM differs fundamentally from the continuum approach used so far for salt mechanics problems. Macroscopic parameters derived from laboratory tests are available for rock salt and can easily be used in continuum-based modeling. Because the DEM considers the mechanical behavior an order of magnitude below the model dimension, relevant micro-parameters are generally difficult to determine from classical investigations. The identification of material parameters used in the constitutive models is often conducted by back-calculation of laboratory experiments. The procedure is called inverse modeling, in which the (unknown) input parameters of the DEM model are varied until the behavior of the numerical sample matches the behavior of a physical sample, e.g. compression test. However, only the macroscopic behavior can be validated this way. Therefore, further investigations are necessary for validation of the micromechanical fracture mechanisms and the simulated fracture pattern.

In order to realize the calibration of the Voronoi models with special consideration of the microstructure, uniaxial compression tests were conducted with the same rock salt lithology described and analyzed in chapter 2.1. In addition to macroscopic data usually recorded during compression tests (stress-strain curves of axial, lateral and volumetric strains), acoustic emission (AE) measurements were also performed (chap. 2.3.1). AE events are defined as transient elastic waves generated by the rapid release of energy within the material due to fracture generation. Therefore, these examinations allow a micromechanical characterization of the relevant fracture processes. The experimental data was supplemented by microscopic examination of the samples after the experiments (chap. 2.3.2). The results are necessary to check to what extent the simulated fracture system coincides with real fracture patterns. The information obtained was then used for parameter identification utilizing optimization methods. The objective is to identify the best estimate of the micro-parameter values that can be applied to simulate the laboratory results (chap. 2.3.3).

2.3.1 Uniaxial Compression Test with Acoustic Emission Testing

A comprehensive geotechnical program including uniaxial compression tests in combination with acoustic emission testing is provided as a basis for the calibration process. Investigations were conducted in collaboration with the TU Bergakademie Freiberg (Institute of Geotechnics). To provide reliable results, 4 samples were analyzed. The results are represented in detail as a laboratory report in Frühwirt (2013) and have therefore been summarized below, based exemplarily on the data of sample PK4. The compression test was performed on a cylindrical specimen with 100 mm in diameter and 250 mm in length. The specimen was loaded axially up to failure using the testing machine TIRAtest 28500. The impact of time-dependent creep (dislocation creep, see Chap. 2.2) on the mechanical behavior was not incorporated in the numerical modeling. Therefore, a fast constant loading velocity of 0.25 mm/min was applied, which is equal to an axial strain rate of 1×10^{-3} min^{-1}. To obtain an even load distribution, the end faces were grinded, and PVC spacers of 30 mm were used to reduce the friction between the end faces of the specimen and the two loading plates. Axial deformation was measured directly on the specimen using three length extensometers with measuring points applied at the third points of the sample length. In addition, the axial strain was calculated by measuring the distance between the two loading plates including the PVC spacers. Lateral deformation was determined by a circumferential extensometer with a roller chain at the center of the specimen. As the specimen diameter enlarges, the chain causes the extensometer to expand. The volumetric strain is calculated by summing up the strain along the principal directions using the information from the length and circumferential extensometers ($\varepsilon_{vol} = \varepsilon_{axial} + 2\ \varepsilon_{lateral}$).

To allow a validation with the simulated fracture processes, additional data was recorded using the method of AE. The objective of AE testing is to detect and locate the fracture generation of rock salt during uniaxial compression tests. AE events are transient elastic waves emitted by the rapid energy release of cracks as they are created or propagated. These waves propagate through the sample and can be detected by sensors mounted on the walls of the specimen. AE testing can provide comprehensive information concerning the intensity, location as well as the type of fracture generation in a stressed material (Lockner, 1993). Thus, it has become a recognized nondestructive test method commonly used for rock damage evaluation in civil engineering (e.g., Zang et al., 1996; Cai et al., 2004; Stoeckhert et al., 2015). Particularly in the domain of salt mechanics, AE testing is an interesting option to further investigate the development and interaction of fractures before and after the dilatancy boundary (e.g., Manthei, 2004; Alkan & Müller, 2008). Specimen inserted in the testing machine between the two spacers with deformation and AE measurement equipment attached on the specimen are shown in Fig. 16.

Acoustic measurements were performed using the acoustic emission system Vallen AMSY-6. The system is based on the so-called "hit-based" architecture using eight piezoelectric sensors fixed to the wall of the specimen. A crack origination, called event, gives rise to acoustic emission that can be detected by the sensors producing a hit on each one. Since the events occur in very quick succession, it must be ensured that the measured AE signals detected by a sensor belong to the correct event. For this purpose, certain criteria were defined, which grouped the individual sensor hits to distinct events. The more criteria are met,

the better the reliability and validity of the results. As a result, fewer events can be measured because not every hit fulfills the requirements for evaluation.

In addition to the possibility of detecting fracture events, it is also possible to locate the AE sources. To identify the source location, the arrival times of hits at different sensors have to be compared. This requires information about the velocity with which the waves travel through the medium. However, the sample gets damaged during the compression test which leads to a reduction of the wave velocity. It is therefore necessary to determine the wave velocity during the compression test by measuring the wave travel time between certain sensors at regular intervals. The ultrasonic waves were generated by creating an inverse piezoelectric effect via the sensors.

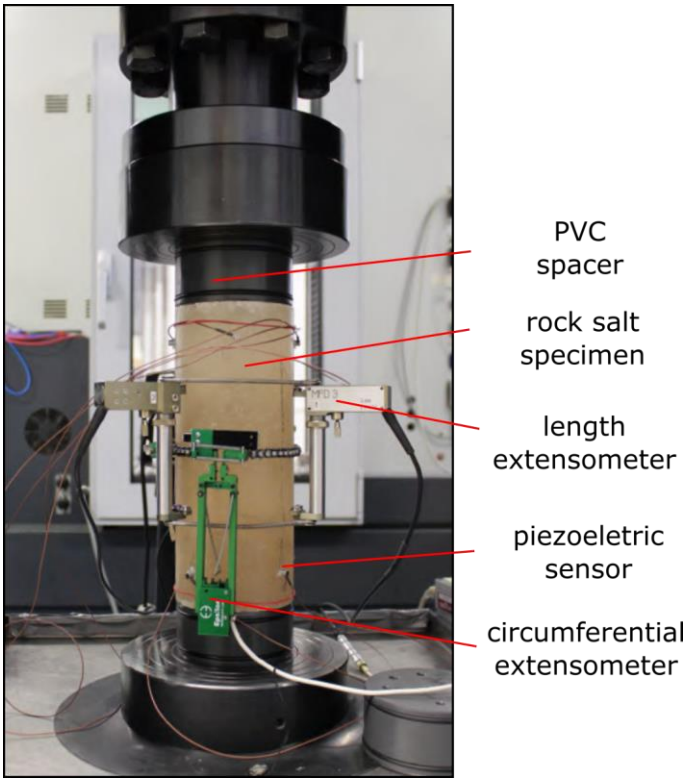

Fig. 16: Specimen inserted in the testing machine between the two spacers with deformation and AE measurement equipment attached on the specimen (modified after Frühwirt (2013)).

The polarity analysis was used to differ between events caused by tensile mechanisms, closure mechanisms, and those with some component of shear motion. The polarity response of an event is based on the sign of the first-pulse amplitude of waves/ hits detected at the sensor. The classification used according to the fracture type is based on a simplistic approach proposed by Zang et al. (1998) using the sign of the first-pulse amplitude *Ai* and calculating the mean polarity value *pol* of hits *k* belonging to a single event:

$$pol = \frac{1}{k}\sum_{i=1}^{k} sign(Ai) \qquad (5)$$

The polarity value *pol* was used to distinguish between shear events (-0.25 ≤ pol ≤ 0.25), tensile events (-1 ≤ pol ≤ -0.25) as well as compression events (0.25 ≤ pol ≤ 1).

Axial and lateral strain versus axial stress is shown in Fig. 17 together with volumetric strain versus axial strain. When loading starts, elastic behavior dominates the stress-strain relationship. However, the stress-strain relationship determined by the length extensometer does not exactly match the axial strain values calculated by the distance of the loading plates. This is because the length extensometer considers the deformation around the center of the sample, which does not include the deformation of the PVC spacer, and effects emerge at the end faces due to closure of secondary cracks. Since this behavior cannot be simulated by the numerical modeling, the calibration is based primarily on the information coming from the length extensometers.

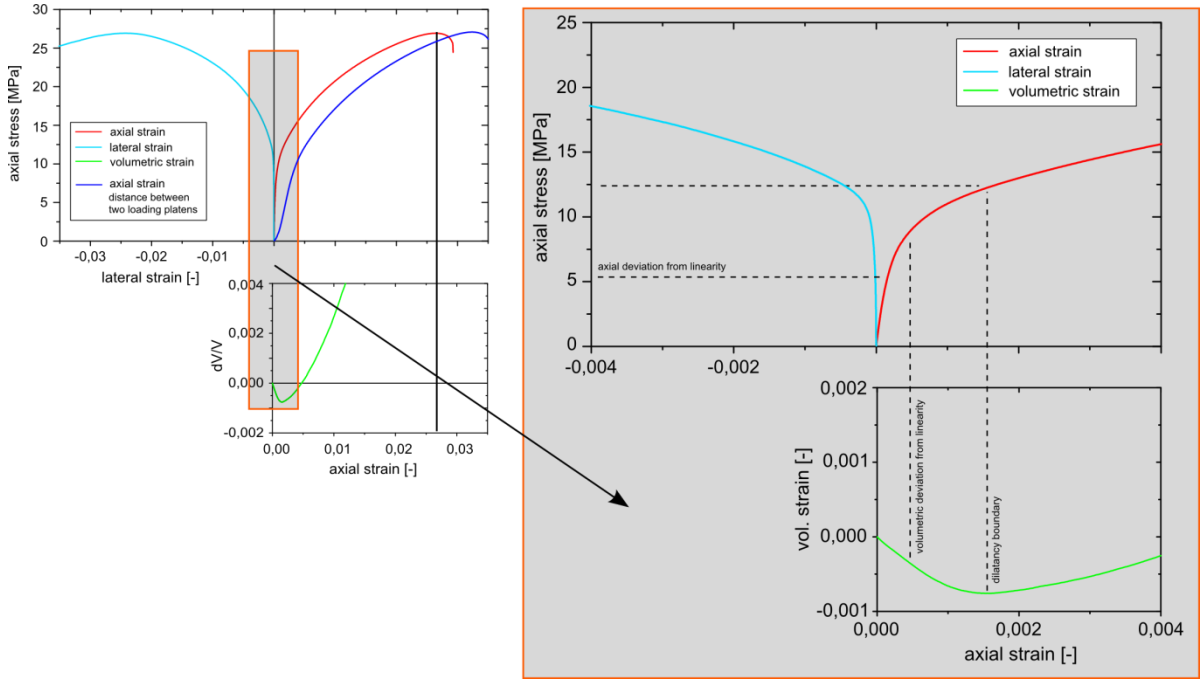

Fig. 17: **Axial and lateral strain versus axial stress, together with volumetric strain versus axial strain.**

The plastic deformation starts at values of about 5 MPa axial stresses and is characterized by a deviation from linearity in the axial strain curve. The strain accumulation is essentially higher in axial than in lateral direction. Moreover, the deviation from linearity in the lateral and volumetric strain curve starts with a marked delay at values between 7.5 to 10 MPa. With increasing axial stress, the volumetric strain accumulates. The dilatancy boundary, which is assumed by a zero derivative of the volumetric strain against axial strain, occurs at an applied stress of 12.5 MPa. The uniaxial compression tests reveal a compressive strength of 27 MPa and an axial strain accumulation of 2.5%, which is comparable with results from literature. The post peak behavior of the uniaxial compression test is characterized by brittle fracturing like failure with an abrupt decrease of axial stress.

Fig. 18 shows the evolution of P-wave velocities during compaction as a function of time. Since the testing machine provides a constant strain rate, the time axis is proportional to the axial strain calculated by the distance between the two loading plates. However, the axial strain measured by the length extensometers is not directly proportional to the time axis. The

elastic range is characterized by P-wave velocities in the range of 4 to 4.5 m/s, which corresponds with data from literature (Gebrande & Kern, 1982). The elastic range ends at an applied stress of about 8 MPa with a significant P-wave velocity decrease to values of about 3.6 m/s. With increasing axial stress, the P-wave velocities are further reduced to 2.25 m/s at axial stresses of 12 MPa and 1.2 m/s shortly before the peak strength.

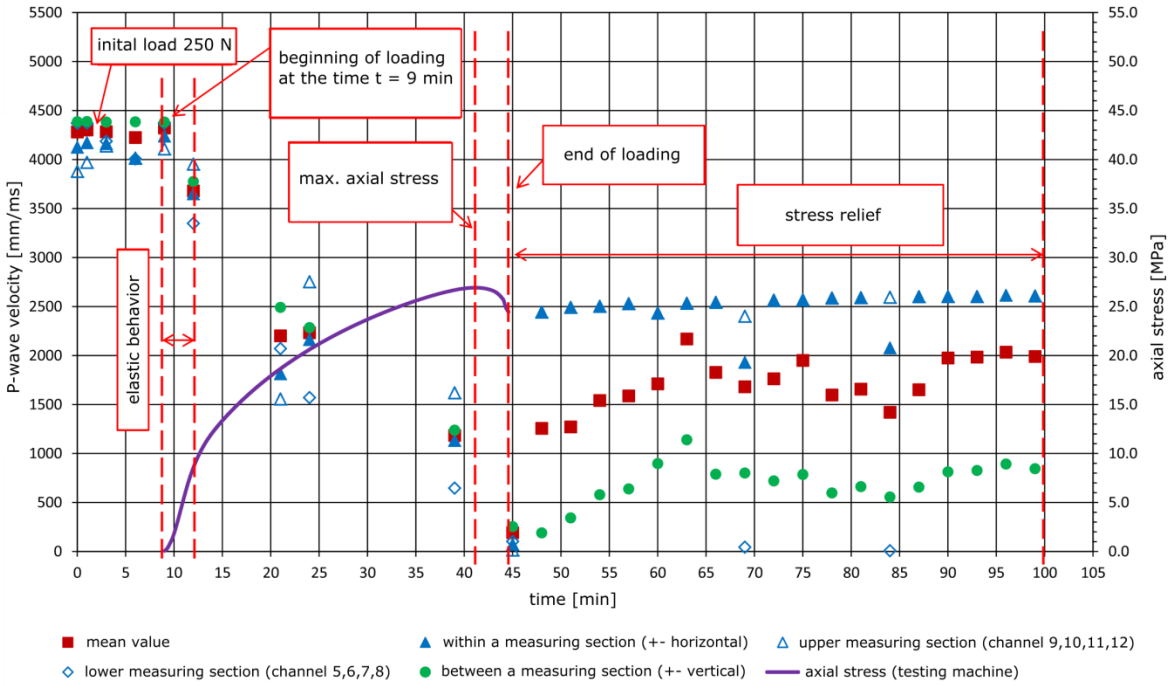

Fig. 18: **Change of axial stress and P-wave velocities as a function of time in uniaxial compression test (modified after Frühwirt (2013)).**

The diagrams in Fig. 19 show the cumulative detected number of AE events and the AE rate versus time as well as the cumulative AE energy and AE energy rate versus time. Diagrams include events detected by all sensors as well as events that are detected at least by two sensors. In the elastic range, there are almost no acoustic events measured by the sensors. AE initiation starts at stress levels above 5 MPa, which corresponds to the point where the axial and volumetric strain curves deviate from linearity. The AE rate increases continuously and the maximum AE rate is reached at axial stresses of 15 MPa. After this, a decrease in AE activity can be observed. Energy and energy rate diagrams show a similar trend with peak levels during the beginning of loading and a gradual decrease with increasing stress. However, a certain amount of AE energy is maintained throughout the entire testing, which indicates that AE events were released continuously. This is comparable to observations from literature. Zhang et al. (2015) compared the AE characteristics of rock salt with granite and marble. The hard rock samples exhibit a gradually increasing trend in the AE event rate and energy rate with an increasing stress level prior to peak strength. Peaks in AE event rates and energy rates predominantly occur at stress levels of approximately 60-80% of the peak strength (Cai et al., 2004; Zhang et al., 2015). In contrast to this, the AE activity of rock salt is reached during early stages of loading and decreases gradually with increasing stress.

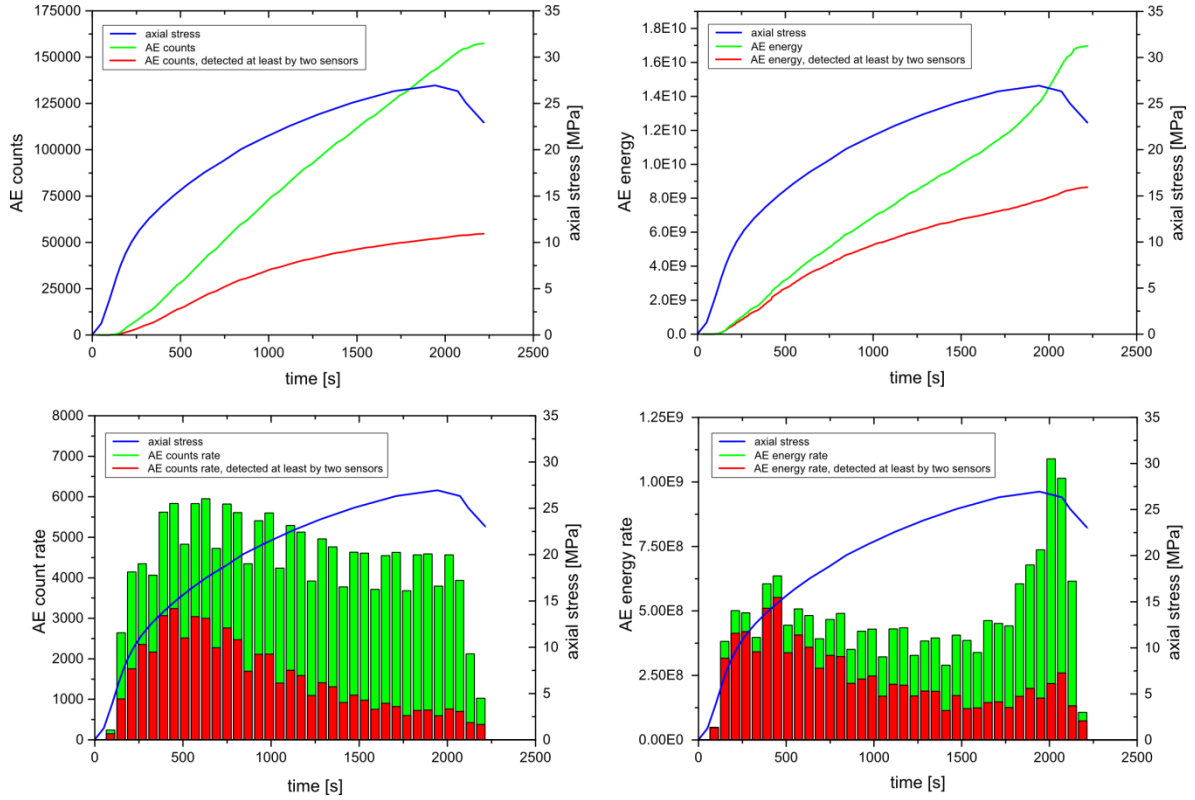

Fig. 19: AE events, AE rate, AE energy and AE energy rate versus time of loading.

A more detailed analysis of AE activity is given in Fig. 20, where the different events were evaluated according to their type of fracture generation (Eq. 5). The first motion polarity analysis of the AE data reveals that nearly 80% are interpreted as tensile fractures. Approximately 10% of the events having first motions predominantly towards the source are denoted as micro fractures of compression type. Shear events characterized both by motions away from the source in some directions and my motions towards it in other directions made up ~10%. Thus, tensile cracking seems to be the main reason for deterioration of rock salt.

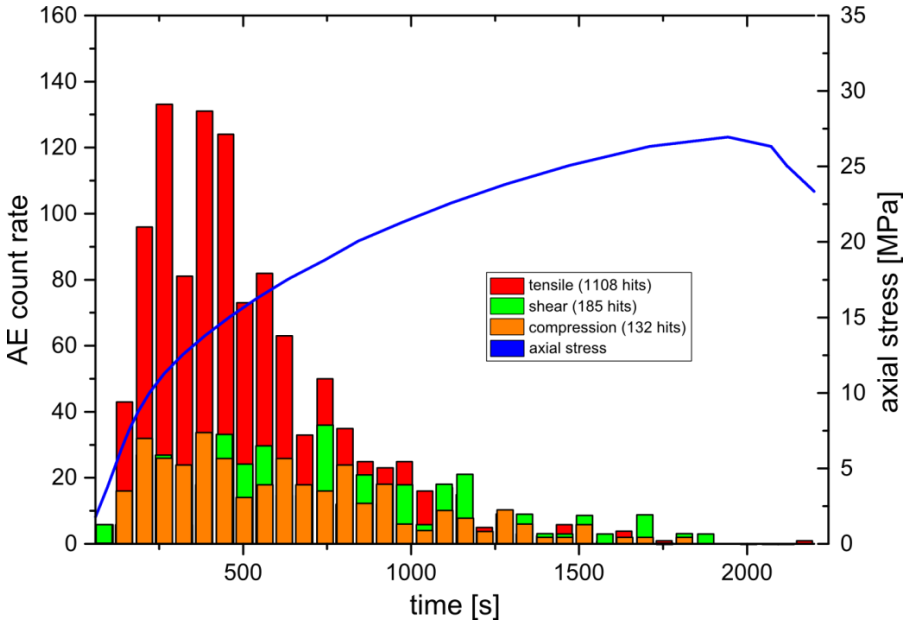

Fig. 20: Classification of located events due to their first motion polarity into three types (tensile, shear and compressionsal) using Eq. 5.

The different types of sources can be compared with respect to spatial and temporal occurrence. Spatial distribution of AE events was determined for different stress intervals (Fig. 21). When loadings starts, AE event locations are concentrated near the specimen ends but are uniformly distributed in space with further loading stress. However, near the peak strength, AE events are restricted to the center of the sample. The formation of a distinct nucleation region or a shear band development was not recognized.

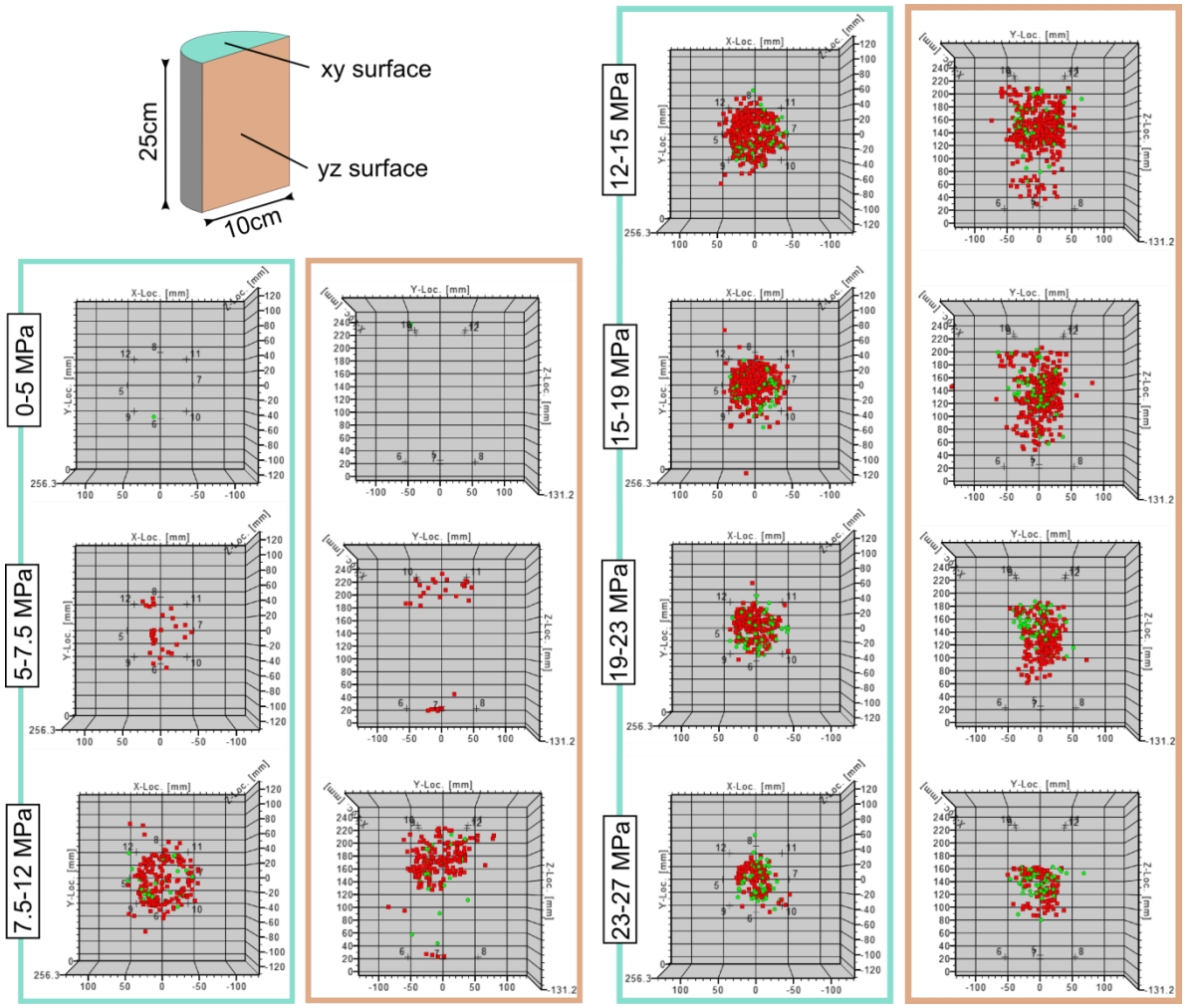

Fig. 21: **Spatial distribution of AE events at different stress level intervals. Green: all hits belonging to a single event are positive according to the polarity analysis (dilation pulse); red: all hits belonging to a single event are negative according to the polarity analysis (compression pulse). Mixed forms are filtered out due to software specific limitations.**

2.3.2 Topology of the Fracture Network

Microstructural investigations were conducted on a deformed rock salt sample in order to complement the AE measurements and to allow the observation of local fracture processes. The sample was evacuated in a desiccator and soaked with blue epoxy resin to intensify the

visualization of microfractures. A thin section was cut parallel to the cylinder axis and through the sample center, and polished surfaces were prepared for microstructural investigations. Fig. 22 shows the deformed sample and the typical microfracture pattern after the uniaxial compression test.

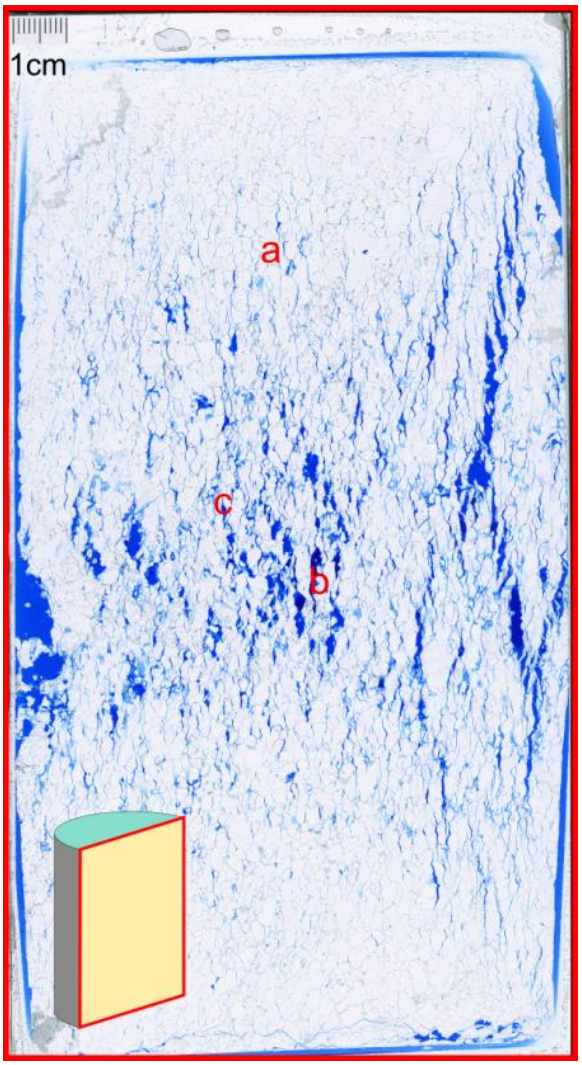

Fig. 22: Thin section image (digital scan using a transparency unit) of the cylindrical rock salt sample after the compression test. The blue areas (epoxy resin) indicate damage due to microfractures. Letters in the image refer to microscopic images (see below).

Fig. 22 shows that the shape of the microfractures is strongly controlled by the halite grains, whereas the direction is closely related to the stress geometry. The fractures are aligned parallel to the axis of maximum stress. Due to the influence of end friction between the sample and the plastic spacers used, cone-shaped areas can be observed. Much fewer cracks can be observed in this domain. These are mostly isolated along grain boundaries and are thus smaller in length and width (Fig. 23a). Intragranular cracks can be observed occasionally along the cleavage planes of the halite minerals (cleavage fractures).

Towards the center of the specimen, the fracture density increases and fracture enlargement and widening become visible (Fig. 23b). Through linkage of more isolated fractures, individual slip-zones lead to the evolution of a pervasive fracture network. In general, fractures initially originate at the grain boundaries and then continue to propagate through adjacent halite grains, mostly along cleavage planes. Wedge-type pores are particularly apparent,

which usually form through piling up of dislocations and grain boundary slip at triple junctions (Fig. 23c).

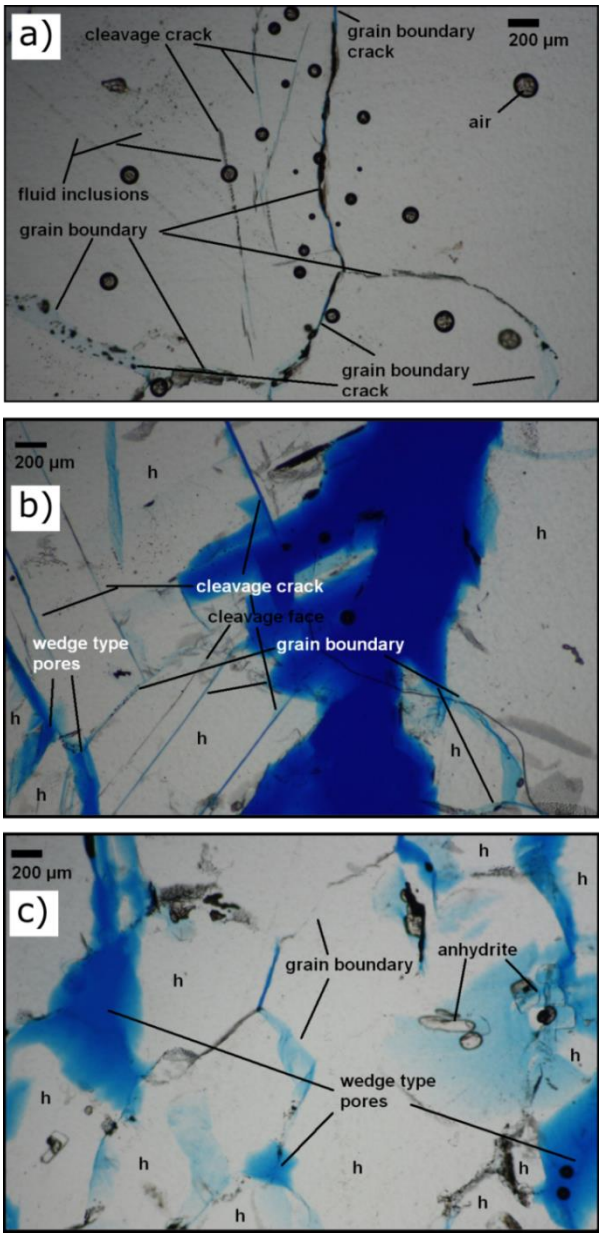

Fig. 23: Images from different thin section areas (see Fig. 22) with typical microfractures that can be observed in a) the upper part and b) at the center of the sample. c) wedge-type pores are apparent, which usually form at triple junctions.

2.3.3 Identification of Material Parameters

Constitutive material models used to describe the deformation of rock salt adequately depend on the optimal set of constitutive parameters. However, parameters used in the discrete element code are usually difficult to determine. To obtain material properties that can be integrated in the discrete element models both sensitivity analysis and parameter identification methods were carried out. Sensitivity analysis is used to understand how changes in the parameters of the constitutive models influence the simulation results. The information gives an indication of which parameters should be examined closely. Parameter identification is based on the information gained by the sensitivity analysis using specific optimization methods. The

objective is to find the best estimate of parameter values that can be applied to simulate laboratory results. Data coming from the uniaxial compression test serves as a calibration reference. The axial and lateral strain versus axial stress, the axial strain versus volumetric strain as well as the cumulative detected AE events were used for calibration.

Sensitivity analysis is almost performed by running the model a number of times and by varying the relevant model values. A large number of runs or designs of experiments are usually required to estimate the sensitivity adequately. Since the simulation of the entire compression test runs several days, sensitivity analysis take high computational efforts. To get reliable results within the time available, the analysis is therefore divided into two parts. The first part of the analysis considers strain curves with axial strain values of up to 0.5%. The range of the linear-elastic deformation behavior as well as the transition to the non-linear deformation behavior is thereby investigated. Since permanent damage occurs due to crack opening, this region is particularly interesting when analyzing the EDZ of a radioactive waste repository. The second part is based upon the information gathered so far to consider the strain curves of the entire compression test up to the peak strength. In addition, a qualitative evaluation with results from AE testing was performed. Investigations were conducted in collaboration with Dynardo GmbH. The results and the theoretical background are represented in detail in Haase (2015) and have therefore been summarized below.

Investigations were conducted using the Software optiSLang (Dynardo GmbH). The software is able to offer a sampling-based sensitivity analysis to identify important parameters, to quantify their influence and to generate a so-called "best design" in comparison with measurement results from the laboratory. optiSLang acts as controlling software that generates run files that can be read into the numerical software by automatically changing the input parameter in given ranges. LS-DYNA, a commercial finite element code based on explicit time integration, was used for the numerical simulations.

Numerical compression tests were performed on a cylindrical specimen with a diameter of 37.5 mm and a length of 75 mm that consisted of 1561 Voronoi elements. To simulate edge effects, the specimen was placed between two PVC spacers (Fig. 24). The bottom of the lower spacer was fixed, while the top of the upper spacer moves downwards in z-direction simulating the loading. To allow a validation with laboratory experiments, additional output data was recorded as close as possible to laboratory conditions. The axial stress is the sum of forces at the top of the PVC spacer divided by the sample area. Axial deformation is calculated by measuring the vertical distance between gridpoints located at the third points of the sample length. Lateral strain was calculated at the center of the sample by measuring the horizontal displacement of gridpoints at the sample area.

The choice of constitutive models used in LS-DYNA is aligned with the models available in 3DEC in order to allow transferability of the results obtained (see chap. 2.2). Deformation is realized both by the deformability of the polyhedral-shaped elements and the displacements or rotations at the grain boundaries.

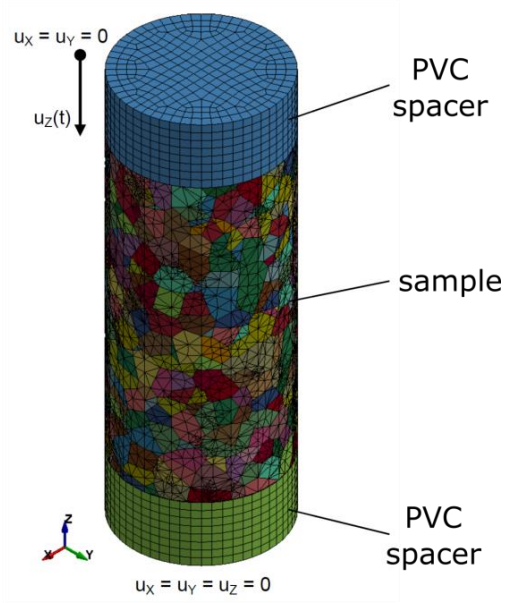

Fig. 24: Numerical model used to simulate uniaxial compression test (modified after Haase (2015)).

The elastic behavior is simulated with a linear-elastic constitutive model. Because of the nature of the discrete element method, the elastic behavior is governed both by the deformability of the polyhedral-shaped elements (blocks) and the displacements at the grain boundaries (contacts). The bulk and shear moduli were used to describe the elastic response within the grains.

The plastic deformation within the salt grains is mainly generated due to an accumulation of dislocations when recovery mechanisms do not occur. With increasing dislocation density and resulting increase of interactions between both free dislocations within each glide plane and different glide planes, they can constrain each other in their development. As a consequence, a larger yield stress is required to maintain plastic deformation. In order to simulate the deformation within the salt grains with an associated mechanism of hardening (dislocation glide), a continuum-based Mohr-Coulomb criterion with an additional strain hardening approach is applied. The model is based on a common Mohr-Coulomb model with nonassociated shear (shear yield function) and associated tension (tensile yield function) flow rules. The shear yield function is given by the internal cohesion c as well as the internal friction angle φ by:

$$f^s = \frac{\tau}{\sigma_n \cdot tan\varphi + c} \geq 1 \qquad \textbf{(6)}$$

The difference of the additional strain hardening approach lies in the possibility that the cohesion, friction, dilation and tensile strength may harden after the onset of plastic yield. In the Mohr-Coulomb model, these properties are, however, assumed to remain constant. In order to simulate the effect of hardening, only the cohesion is increased after yield as a function of the plastic portion of the total strain using the aforementioned approach. Since the structure of the salt crystal is not modified by the deformation processes, a constant volume and crack-free deformation is assumed. Thus, the dilation angle in the shear potential function of the corresponding nonassociated yield function was reduced to zero and the tensile strength was increased in such a way to inhibit tensile failure due to the tension yield function. The

variation of the cohesion with plastic strain (strain hardening function) and the friction angle are the basic parameters that define the deformation of the grains.

Damage and failure due to fracturing along grain boundaries is based on slightly different approaches in the numerical codes used. LS-DYNA can only use bonded contacts with an additional failure criterion to simulate fracturing along discrete elements. The contacts are penalty-based and have a finite stiffness (spring) in normal and tangential direction. The size of the contact segments and its material properties are used to determine the contact spring stiffness. A distinction between stiffness values in normal and tangential direction is not possible. Due to the deformation of the contact springs, interaction forces are calculated at the contacts. If the magnitudes of the tensile normal or the shear tangential contact force exceed the respective strength, the bonded contact breaks. The failure criterion under tensile stress in normal direction is based on an elliptical coupling relationship between normal stress σ_n and shear stress τ, where the tensile strength σ_t^{max} and the shear strength τ^{max} represent the major and minor semi axes:

$$f^t = \left(\frac{\sigma_n}{\sigma_t^{max}}\right)^2 + \left(\frac{\tau}{\tau^{max}}\right)^2 \geq 1 \quad \textbf{(7)}$$

Under compressive stress in normal direction the shear stress is limited to the shear strength:

$$f^s = \frac{\tau}{\tau^{max}} \geq 1 \quad \textbf{(8)}$$

After bond breakage has occurred, in either tension or shear, a simple frictional sliding criterion (Coulomb friction law) is used to describe subsequent deformation:

$$f^s_{slip} = \frac{\tau}{\sigma_n \cdot tan\varphi} \geq 1 \quad \textbf{(9)}$$

where φ is the friction angle of the fracture surface. Dilation of the fracture surfaces takes place at slip which is controlled by an associated flow rule.

Contacts in 3DEC are also penalty-based and are simulated by stiffness springs in normal and tangential direction. In contrast to LS-DYNA, the contact stiffness can be defined independent of the material properties of its adjacent discrete elements. Furthermore, contact stiffness can be different in normal and tangential direction. In order to simulate fracturing along contacts, 3DEC allows the use of comprehensive constitutive models for fractures, such as Mohr-Coulomb or continuously yielding model. Since LS-DYNA is, however, restricted to bonded contacts and in order to ensure a comparison between both numerical codes, a similar approach is applied in 3DEC. A Mohr-Coulomb criterion (shear yield function) including a tension cut-off condition (tension yield function) was used and the friction angle was set to zero to simulate ideal plastic material behavior. Thus, the maximum shear and tensile force is limited to the cohesion c and the tensile strength σ_t^{max} of the contact, respectively:

$$f^s = \frac{\tau}{c} \geq 1 \quad \textbf{(10)}$$

$$f^t = \frac{\sigma_n}{\sigma_t^{max}} \geq 1 \quad \textbf{(11)}$$

Once the onset of failure is identified at a contact, in either tension or shear, the tensile strength and cohesion are considered to be zero. In order to simulate a Coulomb friction law after slip, the residual cohesion was set to zero and the friction angle contains an angle unequal zero. The dilation angle at slip was set equal to the friction angle in conformity with the associated flow rule implemented in LS-DYNA. Fig. 25 compares both approaches.

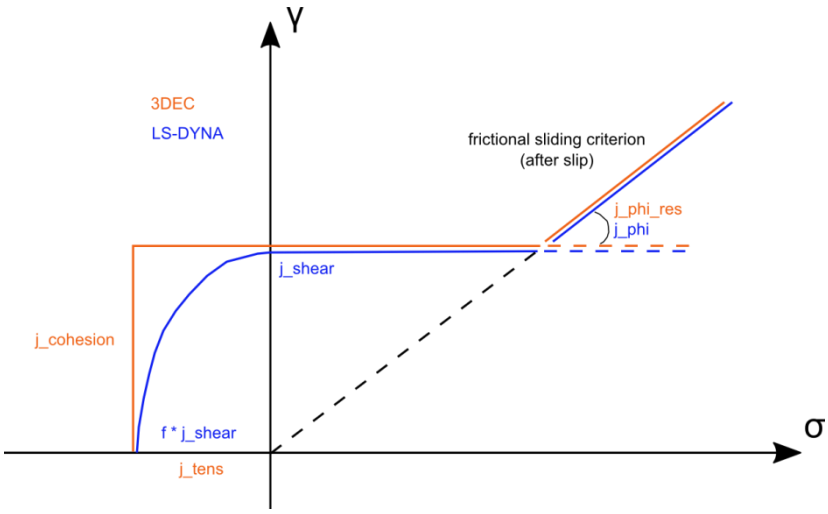

Fig. 25: Constitutive models used in LS-DYNA (blue) and 3DEC (red) to simulate fracturing along grain boundaries (modified after Haase (2015)).

The input parameters used in sensitivity analysis and in LS-DYNA are listed in Table 1.

Table 1: Input parameters used in LS-DYNA

Input parameter					
Grains		Contacts		PVC-Spacer	
Young's mod.	*K_Emod*	shear strength	*j_shear*	Young's modulus	*PVC_Emod*
Poisson ratio	*K_nue*	friction angle	*j_phi*	Poisson ratio	*PVC_nue*
friction angle	*K_fric*	tensile strength	*j_tens*	friction coefficient	*PVC_K_fric*
dilatation	*K_dila*				
cohesion	*K_coh*				

To quantify the influence of input parameters on the simulation results, different quantities are available in OptiSLang. The so-called Metamodel of Optimal Prognosis (MOP) is an important component that represents the most important correlations between parameter input variation and output results. However, the prediction quality of an approximation model may be improved if important input parameters are removed from the model. Within the sensitivity analysis, the Coefficient of Prognosis (CoP) is used to filter relevant input parameters. According to the prognosis capability of the resulting values, optimal meta-models will be selected. Fig. 26 shows the Coefficient of Prognosis matrix for relevant input parameters on

the simulation results (stress-strain curves). The sensitivity analysis to axial strain values of 0.5% reveals that the shear strength of contacts *j-shear* has the greatest influence on the prognosis ability of the simulation results. The relevant coefficients of prognosis (CoP) values are between 57.9% and 83.2%. The input parameters K_fric and j_tens show CoP values of about 15%. The total CoP value of 64.6% for the axial strain-stress curve reveals that the input parameters j_shear and the inner friction angle K_fric do not entirely explain the model reaction.

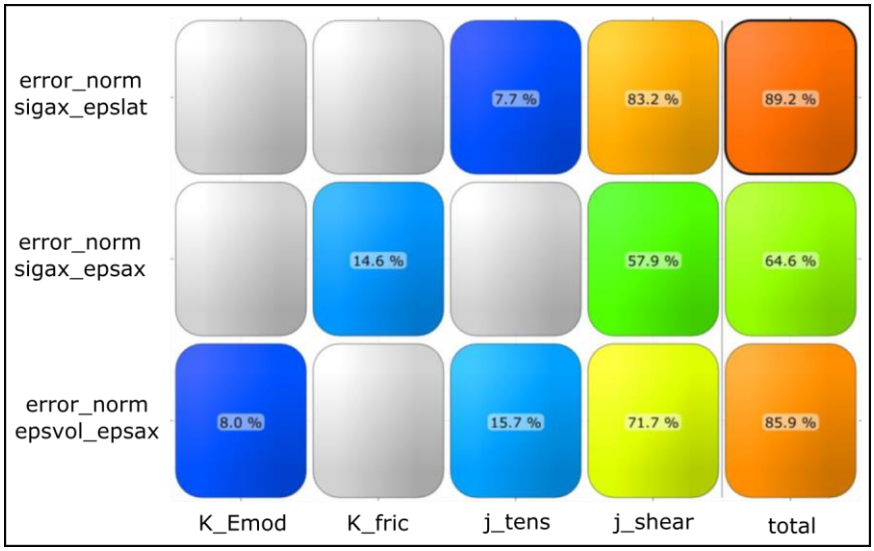

Fig. 26: Coefficient of Prognosis (CoP) matrix for relevant input parameters on the simulation results; stress-strain curves (modified after Haase (2015)).

Fig. 27 shows numerical calculation results against laboratory results. When analyzing the simulated axial strain versus stress curves it is noticeable that many curves deviate early. The lower the shear strength of contacts, the earlier the specimen fails. The resultant curves obtained are, however, not suitable for the prognosis capability since statistical sensitivity was not achieved for more input parameters.

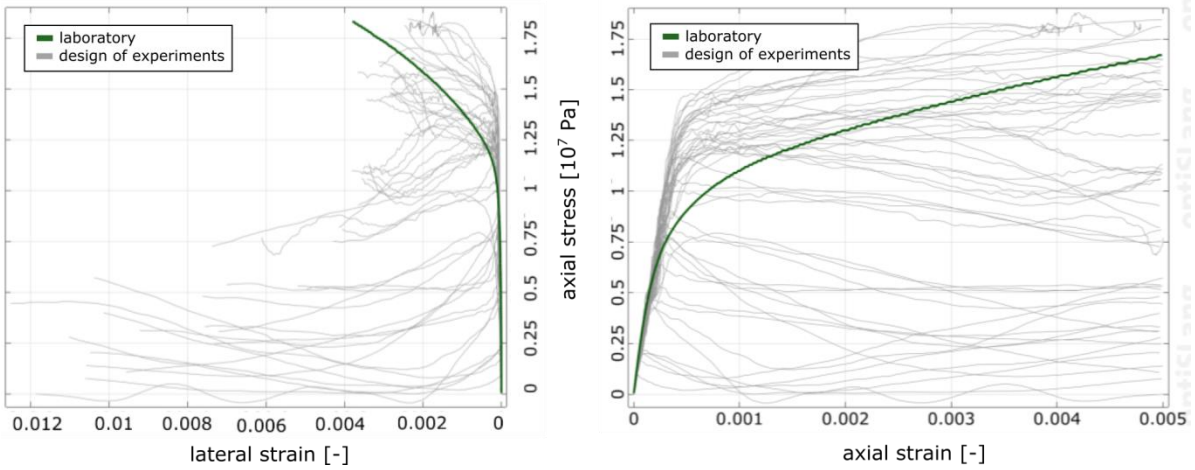

Fig. 27: Sensitivity analysis results showing simulated curves (grey) against laboratory results (green).

With the information coming from the first part of the sensitivity analysis, calculations were conducted for the entire compression test up to the peak strength. The strain hardening

curve was adjusted manually based on the estimated parameter values obtained from the first part of the investigation. Fig. 28 shows numerical calculation results against laboratory results. The axial stress-strain curves show predominantly a failure at 2.5-3% axial compression. Lateral stress-strain curves correspond well to lateral strain of 0.6%, but do not achieve axial compressive strengths with lateral strain values of 2.3%. Axial stresses reach approximately the axial compressive strength of the laboratory test with values of 27 MPa. The curve progression of curves that are above the compressive strength is mainly controlled by the strain hardening function and thus determined by deformation of the grains. However, if a curve is below the compressive strength, the shear strength is decisive and the failure is related to grain boundary cracking.

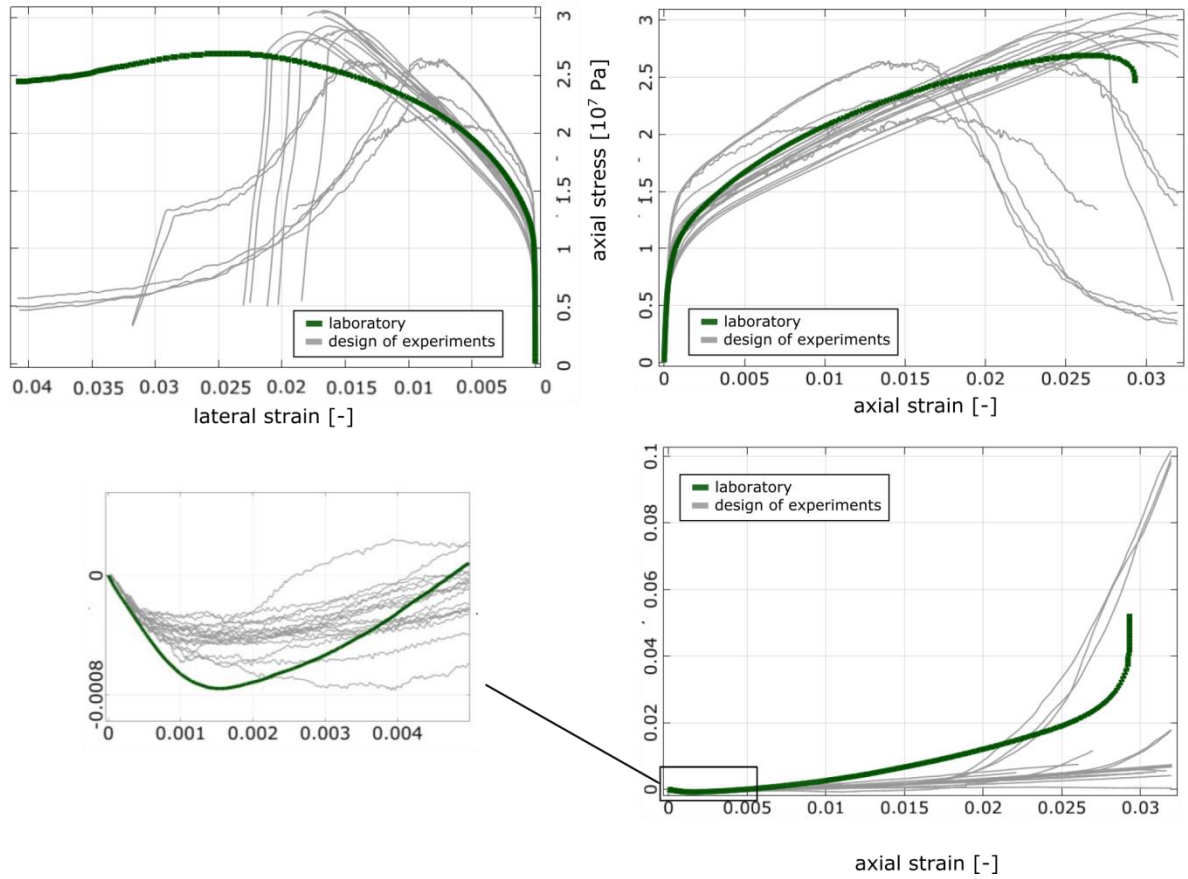

Fig. 28: **Sensitivity analysis results showing simulated curves (grey) against laboratory results (green) (modified after Haase (2015)) .**

Fig. 29 shows the relationship of shear and tensile events compared to the strength at the grain boundaries. To get a better overview, different curves were selected as an example and classified according to their failure mechanisms. The blue and cyan marked calculations show a failure due to the strain hardening function, whereas the orange marked curves are related to grain boundary cracking. The higher the shear strength, the less it is possible to damage the model along the grain boundaries and the lower the number of shear fractures. A similar behavior can be observed when looking at the tensile fractures. Smaller tensile strengths result in a greater number of tensile fractures. This clearly shows that the correct curve progression is mainly achieved by an adequate parameter set controlling grain defor-

mation and deformation along the grain boundaries. The results of the sensitivity analysis indicate that intra- and intercrystalline deformation are closely related to each other.

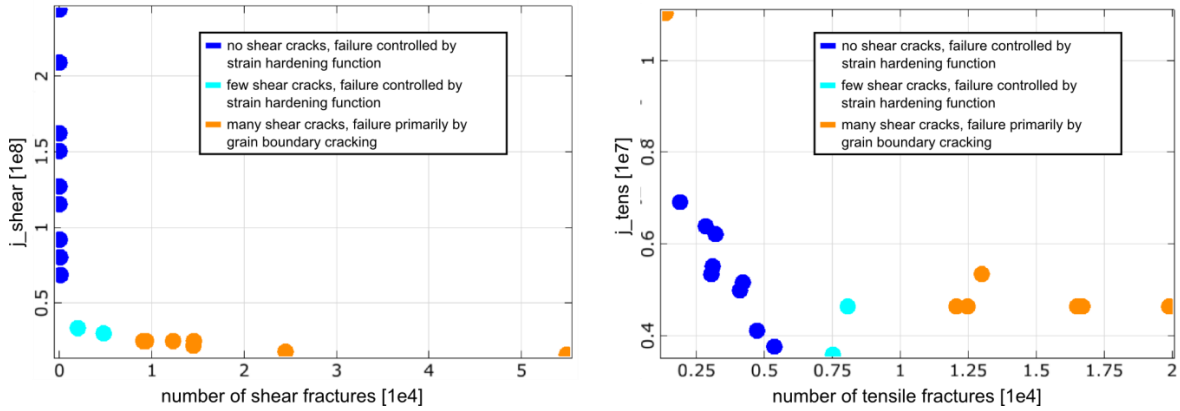

Fig. 29: **Relationship between number of shear (left) and tensile (right) fractures compared to the strength at the grain boundaries. Selected calculations are classified according to their failure mechanisms.**

To make a qualitative comparison between numerical and laboratory results, cumulative fracture events were plotted against axial stress (Fig. 30). A linear increase of fracture events over stress can be determined for the cyan and blue curves. However, these are samples where the failure is mainly controlled by the strain hardening function and determined by intracrystalline deformation of the grains. Thus, the orange curves should better correspond to laboratory results where the failure is primarily due to intercrystalline cracking.

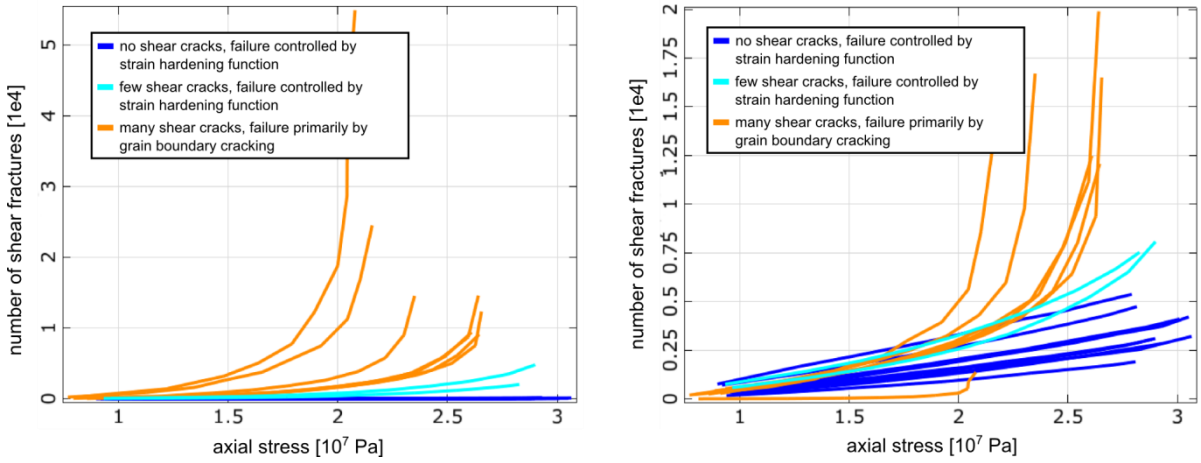

Fig. 30: **Cumulative shear (left) and tensile (right) fracture events versus axial stress for selected numerical calculations. Selected calculations are classified according to their failure mechanisms.**

The results indicate that the number of events, both shear or tensile, increase significantly towards the compressive strength. This is contrary to the laboratory results obtained, where the maximum AE rate is reached at axial stresses of 15 MPa and tends to decline thereafter.

Furthermore, the higher number of tensile fractures over shear events cannot be simulated adequately. However, a direct comparison between laboratory and numerical analysis by LS-DYNA appears difficult since the criteria for the classification into tensile and shear fractures are completely different.

Furthermore, it was shown that the laboratory condition selected has an impact on the deformation behavior of the sample. Due to the lower Young's Modulus of the PVC spacers with respect to the sample and the associated higher elongation at the top and bottom, the sample center becomes constricted at the beginning of loading. This constriction results in a smaller axial strain (Fig. 31). With increasing stress, the deformation behavior changes, which leads to greater axial strain accumulation at the sample center as compared to the entire salt sample.

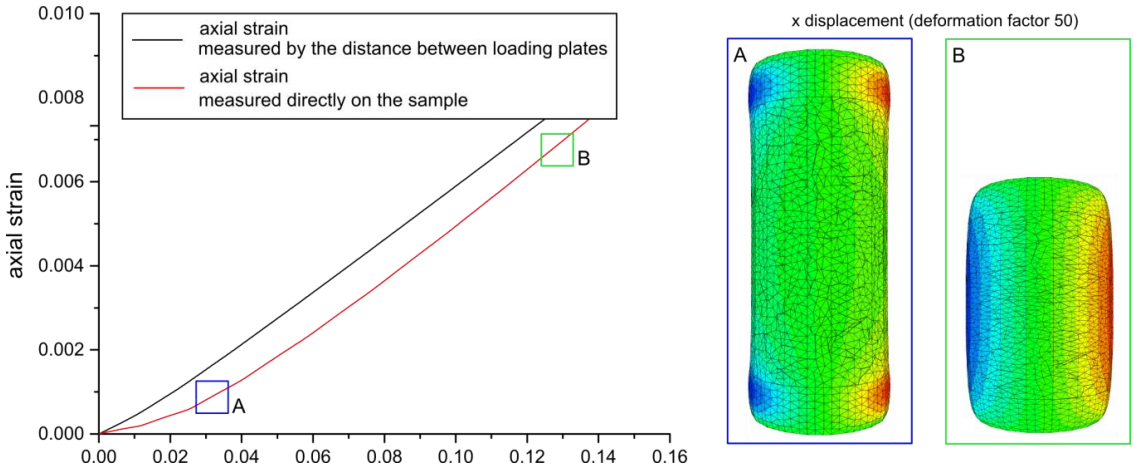

Fig. 31: **Concave and convex deformation of the sample at the beginning and with increasing stress.**

The information obtained from the sensitivity analysis was then used for parameter identification. The objective is to identify the best parameter set (best design) that can be applied to simulate the laboratory results adequately. The best design of the parameter identification was also used as an input parameter set using 3DEC. However, this requires a rescaling of parameter values in order to assign a suitable elastic and plastic response. The best design parameter values and the strain hardening function used in 3DEC are given in Table 2.

In 3DEC, the Voronoi model is the same as the one already used in LS-DYNA (see Fig. 24). With respect to the discretization there are differences. The Voronoi discretization in LS-Dyna is carried out with 10-node quadratic tetrahedral elements whereas 3DEC uses linear shape functions (4-node tetrahedral elements).

Table 2: Calibrated parameters used in 3DEC

	rock salt		PVC-spacer	
	blocks	contacts	blocks	contacts
Young's modulus	36.75 GPa		3 GPa	
Poisson ratio	0.26		0.42	
normal stiffness		100000 GPa/m		35833 GPa/m
shear stiffness		28000 GPa/m		10000 GPa/m
friction angle (at slip)	21.15° (21.15°)	0° (18.52°)		0° (18.52°)
dilation angle	0°	29.75°		18.52°
cohesion (at slip)	$a\ e_{pl}^{\ b} + coh_{ini}$ coh_{ini} = 2 MPa a = 3.92E07 b = 0.422	15.45 MPa (1 MPa)		1 MPa (1 MPa)
tensile strength (at slip)	-	4.64 MPa (0 MPa)		0 MPa (0 MPa)

Fig. 32 shows calculation results of the best design against laboratory results. When looking at the numerical results and the axial stress strain curves, a comparison with laboratory succeeds well. The plastic deformation starts at values of about 7.5 MPa and is characterized by a deviation from linearity. In LS-DYNA, the axial strain accumulations are slightly higher, whereas 3DEC shows slightly lower strain accumulations compared with the laboratory results. Axial stresses reach approximately the axial compressive strength of the laboratory test with values of 27 MPa. The post peak behavior is characterized by brittle fracturing like failure with an abrupt decrease of axial stress as observed in the laboratory. In LS-DYNA, the calculated lateral strain accumulation up to 0.1% is in good agreement with laboratory results. 3DEC shows a slightly stiffer behavior with lower lateral strain accumulations when compared with the laboratory. However, maximum lateral strain with values of up to 0.25

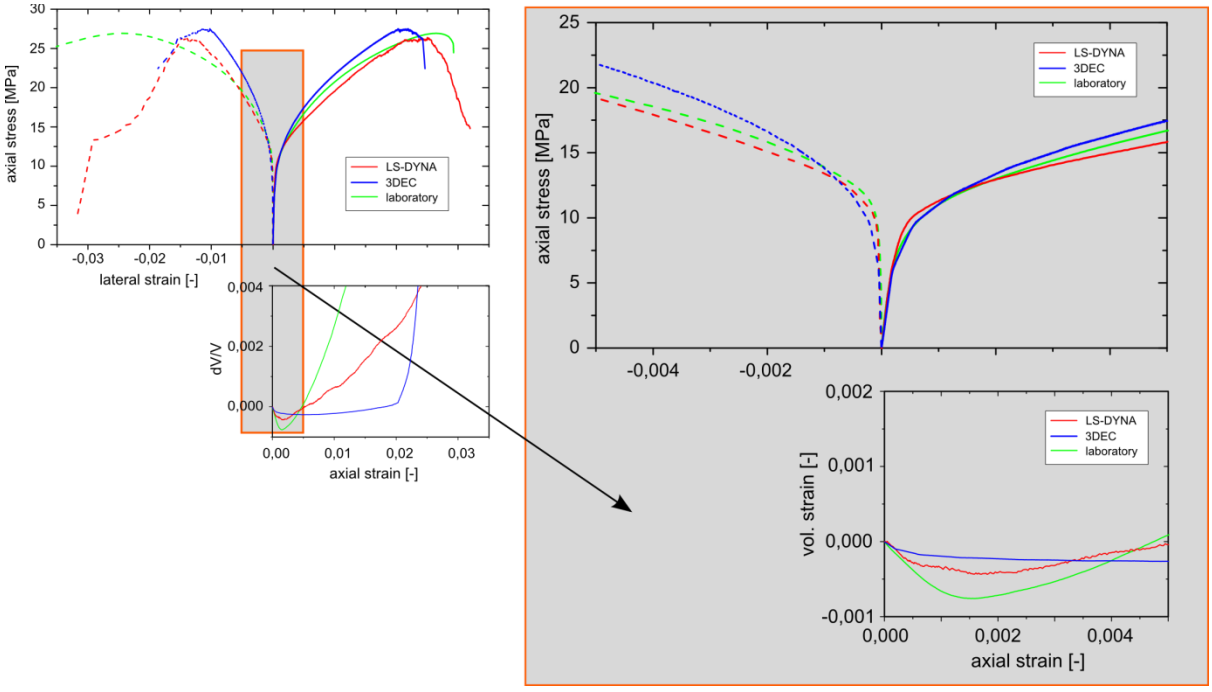

Fig. 32: **Axial and lateral strain versus axial stress, together with volumetric strain versus axial strain of laboratory testing and numerical analysis.**

mm/mm as observed in the laboratory was not achieved in the numerical models. The simulated post peak behavior is characterized by a more or less sudden decrease in stress, whereas the stress, determined in the laboratory, is maintained with increasing lateral strain over a larger range. The volumetric strain, which is directly calculated by using the axial and lateral strain results, does not fully correspond to laboratory tests. The simulation results produced by LS-DYNA qualitatively agree with the basic observations made in the laboratory showing first a compaction due to elasticity that is followed by a subsequent volumetric strain accumulation. The location of the dilatancy boundary is also in conformity with laboratory measurements. Compaction due to elasticity is, however, much too low in 3DEC and the volume increase due to plastic deformation is not adequately simulated. The volumetric strain remains nearly constant over a wider range of axial strain. One reason for this could be the different node elements used for discretization in 3DEC and LS-DYNA. 4-node elements are stiffer compared with 10-node elements and could therefore result in wrong plastic strain accumulations.

To make a qualitative comparison between the numerical analysis and the AE testing, the onset of failure at contacts was equated with events detected by AE testing. The classification of fracture events according to their type of fracture generation was conducted by determining the so-called failure states of contacts in a model using the internal FISH language. There are four contact state indicators in 3DEC, which make it possible to distinguish between intact contacts (indicator = 0), contacts at slip (indicator = 1) and contact failed in tensions (indicator = 3) as well as contacts that have previously slipped (indicator = 2). Only state indicator one and three were used for evaluation. At specific calculation steps (every 1000 steps), the state indicator of each contact was analyzed and the number of failed contacts was plotted over numerical simulation time as well as axial stress (Fig. 33). The onset of failure is identified at stress levels above 3 MPa. The number of tensile fractures increases continuously and the maximum is reached between 10 and 12 MPa axial stress. At the beginning of loading, tensile fractures appear more frequently than shear fractures, which is in good agreement with the laboratory results (see Fig. 20). After this, the number of tensile fractures decreases continuously. The number of shear fractures increases less rapidly up to 12 MPa and is maintained throughout the simulation. Shortly before the peak strength, the number of shear and tensile fractures increases significantly.

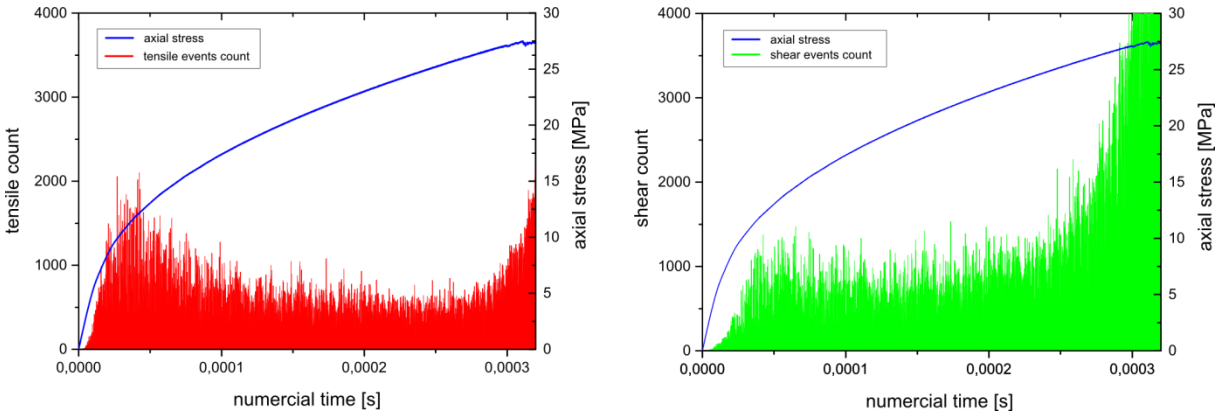

Fig. 33: **Number of contacts failed in either tensile or shear against numerical calculation time.**

Contacts failed in either tensile or shear were evaluated with respect to spatial and temporal occurrence (Fig. 34). To allow a comparison with AE testing results (see Fig. 21), the identification does not include contacts previously failed, but only compromises contacts currently observed to the specified axial stress. When loading starts, cracking is restricted to the specimen ends as observed in the laboratory. Cracking is primarily due to tensile fractures, which is also in good agreement with the AE testing results. Near the peak strength, the locations of crack initiations migrate to the center of the sample. The formation of a distinct nucleation region or a shear band development was not recognized.

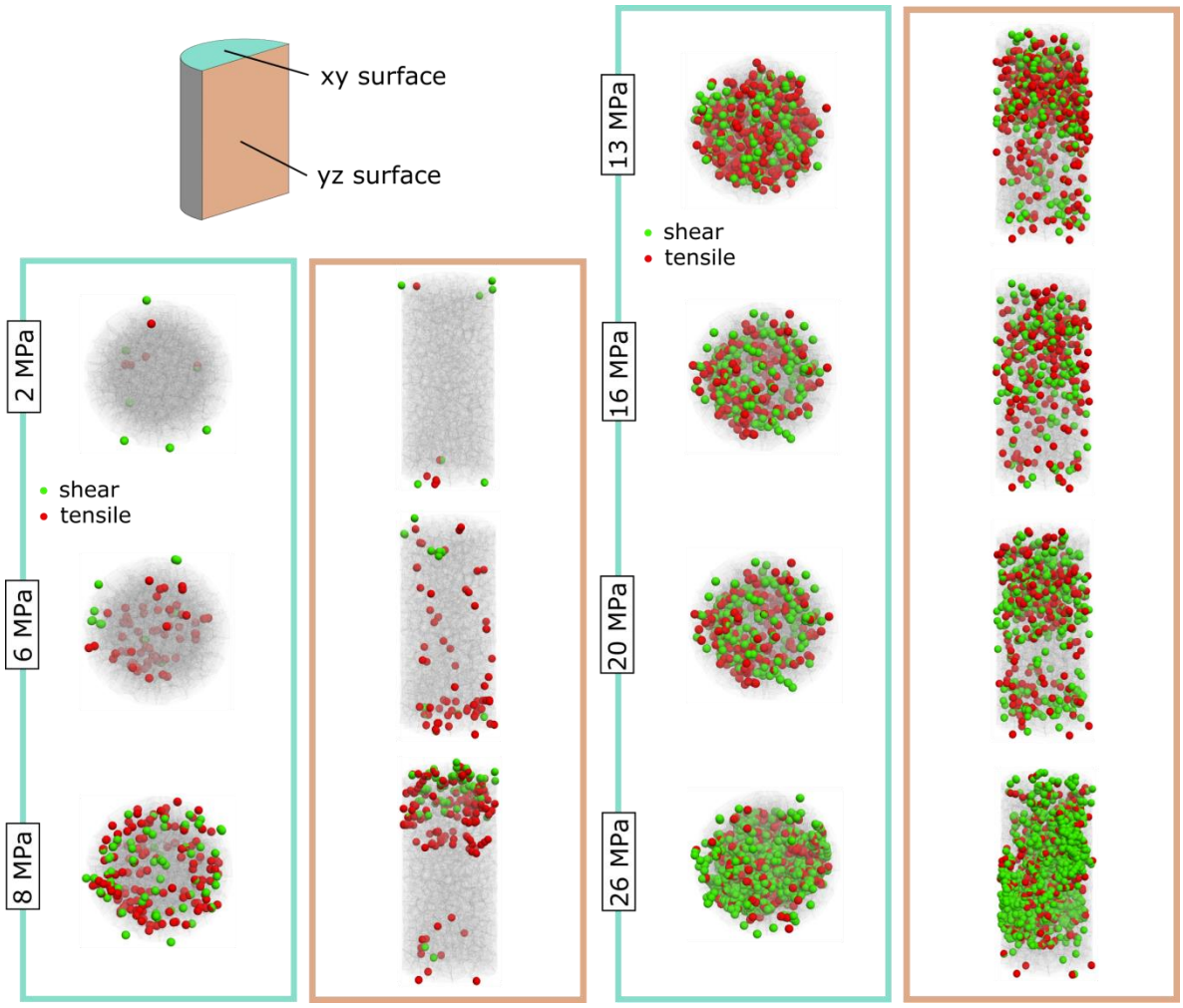

Fig. 34: **Spatial distribution of current contacts in failure, in either shear or tensile, at different stress levels.**

2.4 Discussion

The objective was to develop a modeling approach that can be used to simulate the mechanical deterioration of rock salt at grain scale. It constitutes the basis for the subsequent generation of fracture systems occurring in the EDZ. For this purpose, the DEM code 3DEC was used in combination with polyhedral elements (Voronoi tessellation). Since the shape and arrangement of grains can strongly influence the damage behavior of rocks, it was first

checked how well the Voronoi tessellation corresponds to the microstructure of real rock salt samples. The sphericity and the length-to-width ratio of grains correspond well to the rock salt samples used for comparison but there are differences regarding the grain size distribution and the orientation of the grains. The rock salt samples show a significantly larger proportion of smaller grains. Furthermore, a directional anisotropy in terms of particle shape was recognized that can influence the orientation of fracturing due to stress. However, a further adaptation of the polyhedral elements was not carried out in order to avoid the generation of smaller polyhedral edges and, subsequently, degenerated bad-quality zone elements.

In the first phase of the project, it was assumed that both intra- and intercrystalline deformation processes are related to each other. It is described in the literature that incompatibilities in the plastic deformation of adjacent crystal grains cause local stresses at the grain boundaries, which lead to the formation of intergranular micro cracks. Thus, the models used so far do not allow the simulation of fracturing adequately. However, the entirely new development of a suitable anisotropic model would go beyond the scope of this project due to the amount of time required for implementation. For this reason, the model used in the first phase of the project was optimized by a further parameter adjustment. The results clearly show that the correct mechanical behavior is mainly achieved by an adequate parameter set controlling grain deformation and deformation along the grain boundaries. The results of the analysis indicate that intra- and intercrystalline deformation are closely related to each other. Although the adjustment of the parameters to simulate the mechanical behavior provides good results, the simulation of the fundamental processes of cracking can only be achieved with constitutive models adapted to the DEM approach. Further research is needed in this field.

The identification of material parameters used in the constitutive models was conducted by back calculation of laboratory experiments in terms of uniaxial compression tests. Due to long numerical calculation times when using the usual laboratory sample geometry, the compression test had to be carried out on samples with significantly reduced diameter. This requires detailed knowledge about the mechanical representative elementary volume (REV) that is the smallest volume over which a representative deformation behavior can be expected. The diameter of the sample was set ten times the largest grain in the rock as generally recommended to ensure a sufficient quantity of blocks. However, it has not been studied to what extent the small sample size has an influence on the test results. Furthermore, only one structural Voronoi model was used for calibration. Therefore, it should be noted that certain statements about the statistical variance of the mechanical results are not possible.

The calibration process is based on laboratory experiments in terms of uniaxial compression tests. The parameters derived for the Mohr Coulomb law only provide satisfactory results for relatively small external restraints as usually observed at the outer contour zone. However, under triaxial stress conditions usually observed for rock salt, a non-linear relationship has to be considered so that the linear relationship used in this report can only be an approximation. This applies particularly to the internal friction angle of the grains controlling the plastic deformation of single crystals. The calibration process by means of optimization methods

results in an internal friction angle of 21°. However, the deformation of single crystals can only depend on the differential stress and shall not be dependent on the stress magnitudes as described by the Mohr Coulomb law. Thus, with increasing stress, a higher differential stress is needed for the deformation of grains, which does not correspond to the response of single crystals when subjected to external load.

3 Simulation of Fracturing Processes in the Excavation Damaged Zone

Many methods to describe the damage inside the EDZ are based on continuum mechanical approaches. An advantage is that larger structures can easily be simulated and the development of constitutive models is well devised and proven. A disadvantage is that the simulation of damage with fractures explicitly represented is only suitable to a limited extent. For this reason, DEM models have recently been used to calculate the EDZ (Jobmann & Billaux, 2010; Lisjak et al., 2015). The explicit consideration of discontinuities is the main advantage over the continuum approach where the mechanical behavior of the rock matrix and the fractures are simply homogenized over the volume.

The following chapter contains the generation of realistic fracture networks occurring in the EDZ using the DEM approach. The excavation of a drift is first simulated with continuum mechanical approaches and the zone stresses are recorded in certain parts and for certain depths of the EDZ. The zone stresses are then transmitted as boundary stresses onto a DEM model to simulate the fracturing in the EDZ.

3.1 Continuum Modeling to Derive the In-situ Stress State

The objective of the continuum mechanical modeling is to determine the in situ stresses that occur in the region surrounding an excavation in a rock salt formation. These stresses will be used as boundary conditions in the discrete element modeling to determine the EDZ (chap. 3.2).

The numerical model is based on continuum mechanical approaches and consists of a rock model with an excavation. The model was built under the requirement that the boundary conditions should not influence the simulation results in the region surrounding the disposal gallery. This leads to the simulation model dimensions of 200 m in the length and 200 m in the height. Fig. 35 illustrates the resulting numerical model and the area of interest (colored in blue). The top of the model corresponds to a depth of 1150 m and the bottom boundary is at 1350 m below ground level. The drift is modelled with a simplified geometry by using a square of six meters length with rounded corners at the center of the model. Rounding the corners permits to avoid numerical stress concentration effects that typically occur at sharp corners when the elastic material model is considered. The drift is located at a depth of 1250 m below ground level.

The drift is assumed to be long enough so that stresses along the drift are constant and the deformations in the direction along the drift can be neglected. Thus, the simulation process can then be reduced to a two-dimensional model. This approach is more conservative in comparison to a three-dimensional case. In a full three-dimensional model, the stress distribution and the deformations take place in two directions (along the depth and along the gallery) whereas only one deformation direction is possible in a 2D model. This leads to more stresses and more deformations in a two-dimensional model.

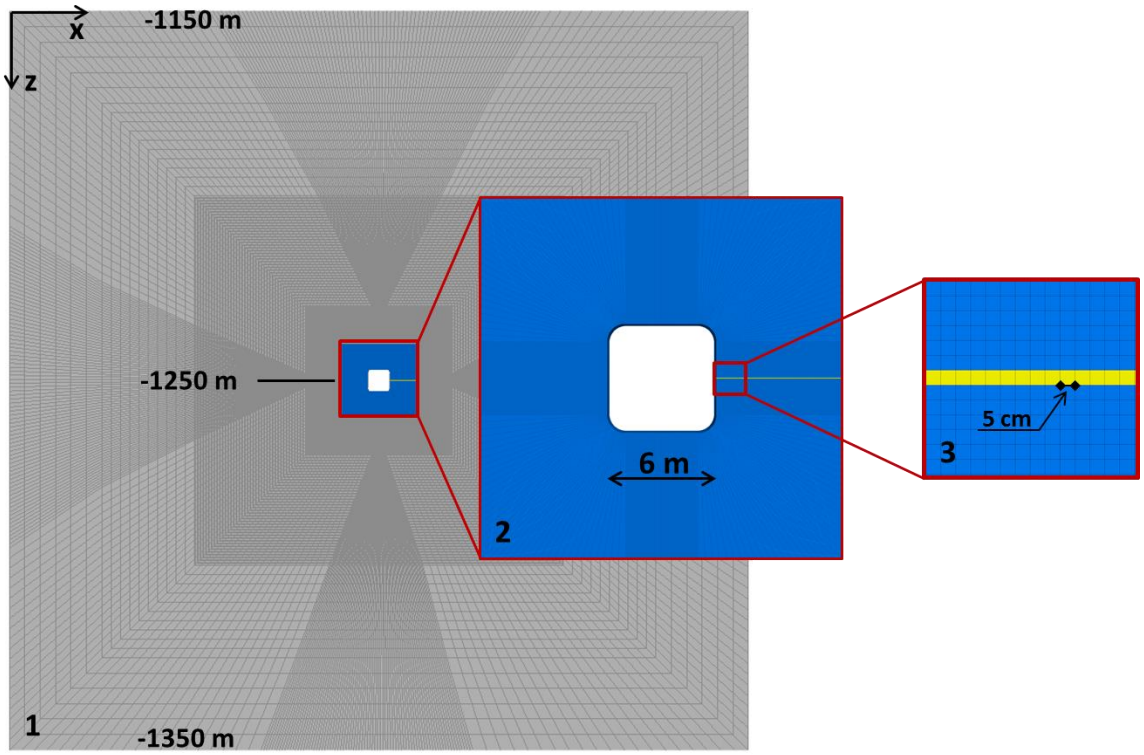

Fig. 35: Numerical model used to derive stress conditions

The model is constrained at the left, right and bottom boundaries with roller boundary conditions. A roller boundary condition supposes that only the degree of freedom perpendicular to the boundary face is fixed while gridpoints are free to move along the two other degrees of freedom parallel to the boundary face. A stress boundary of 24.8 MPa corresponding to the weight of the overburden rock is applied at the top boundary of the model to reestablish the in-situ stress conditions in the model. Since a two-dimensional model is considered, symmetric boundary conditions are placed at the front and back face of the model. When symmetric roller boundaries are applied, the displacement of boundary gridpoints is restricted to a movement within the boundary plane. The gridpoint displacement perpendicular to the boundary is disabled.

The area surrounding the gallery is discretized with identical hexahedral zones. Each discretized zone has a square form of 5 cm length. These dimensions correspond to those of the model, which will be analyzed using the discrete modeling approach at the mesoscopic scale (chap. 3.2). Some zones are monitored during the simulation from the drift contour up to a depth of 7 m. These zones are highlighted in Fig. 35 (yellow zones). Stresses computed in these zones will be used as stress boundaries during the discontinuum mechanical modeling.

The geology considered for this study is a generic rock based on the rock salt formations located in Germany. The rock salt is assumed to be homogeneous. The linear elastic parameters for the generic rock salt are a Young's modulus of 31 GPa coupled with a Poisson's ratio of 0.24. The values were derived from the numerical compression tests performed on cylindrical specimens to allow an alignment between continuum and discontinuum defor-

mation. 2200 kg/m³ is the assumed value for the density of rock salt. This value represents the average density of homogeneous rock salt in the north of Germany. The gravity is set to 9.81 m/s². A stress anisotropy factor of 0.8 is assumed here for testing.

Rock salt exhibits a visco-plastic material behavior when it is subjected to mechanical loads. However, viscous or plastic behavior was neglected and the stress redistribution is solely based on the linear elastic solution. The simulation is performed with the finite difference based code Flac3D (Itasca, 2005). The simulation process starts with the initialization of the primary stress condition. This is the stress state in the rock before excavation. After this step, the excavation takes place by removing the finite difference zones compromising the drift. Numerically, this means that the stiffness of these zones is set to zero. Then, equilibrium iteration is performed. During the calculation, the rock mass converges and stress redistributions occur.

The primary stresses are assumed to be lithostatic heterogeneous since a stress anisotropy factor of 0.8 was set in the model. At the level of the drift, the vertical stress σ_{zz} is equal to -27 MPa whereas the horizontal stresses σ_{xx} and σ_{YY} are equal to -22 MPa before the excavation. The graphical evaluation of the σ_{xx}-, σ_{YY}-, σ_{zz}- and σ_{xz}-stresses after the excavation are presented in Fig. 36.

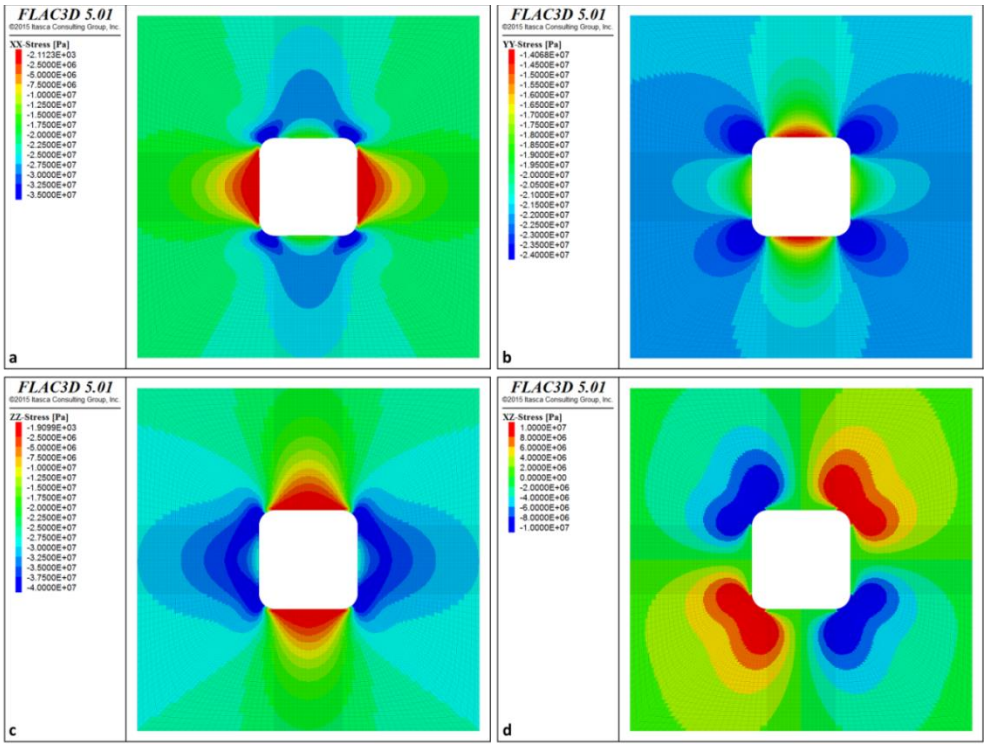

Fig. 36: Stress state after excavation.

In addition, the stresses in the monitored zones are shown in Fig. 37. The σ_{xY}- and σ_{Yz}-stress components remain equal to zero since a 2D-model is considered. The σ_{xx} stresses decrease from -22 MPa to nearly zero at the side wall of the drift due to stress redistribution. The σ_{YY} -stress component is equal to -14 MPa directly at the side wall and increases up to the level of the lithostatic primary stress of -22 MPa. Compared with the analytical results of

the excavation of a circular gallery where the maximum of σ_{zz} is located directly at the side wall and is equal to two times the value of the horizontal stress component, the maximum vertical stress component in the drift is located deeper in the rock. The evaluation of the stresses in the monitored zones shows that the vertical stress at the gallery contour is about -28 MPa, reaches a maximum of -37.5 MPa at 1.5 m from the wall and decreases asymptotically up to vertical primary stress level of -27 MPa (Fig. 37). The contour plot of the shear component σ_{xz} shows a concentration of shear stresses at the corners (Fig. 36). These stresses are antimetric over the diagonals of the squared gallery. In the middle of the model, where zones are monitored, the shear stresses remain negligible compared with the occurred normal stresses.

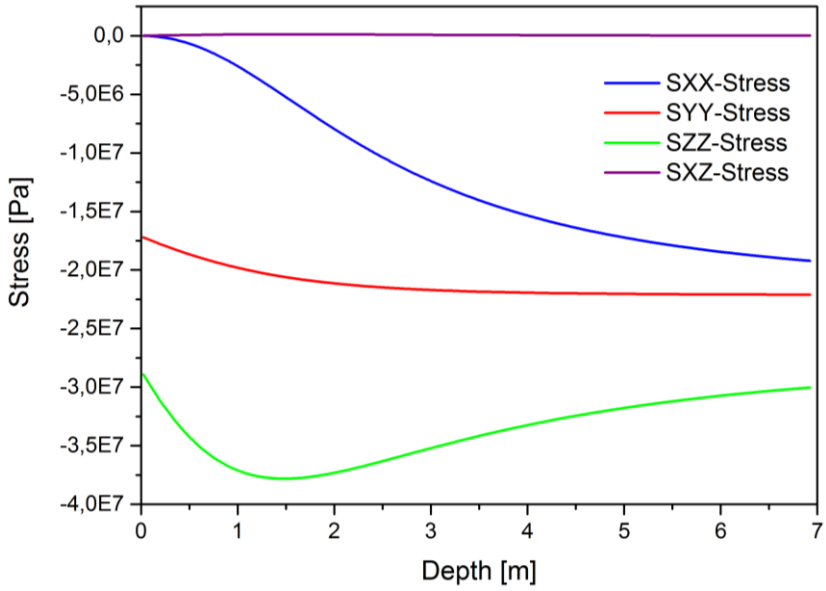

Fig. 37: Monitored stresses with contour depth.

3.2 Discontinuum Modeling to Simulate the Fracturing

Stresses derived from continuum modeling were transferred as boundary conditions on a discrete model consisting of Voronoi elements in order to simulate the fracturing in the EDZ. Displacements in the large model (continuum model) and the submodel (discontinuum model) were, however, not compared in this step. For simplification it was furthermore assumed, that the applied stresses in the submodel are equal on opposite sides. This results in a displacement field where the vertical plane of symmetry is in the center of the submodel. Thus, displacements simulated in the submodel do not correspond to the real displacement field where the convergence is aligned towards the drift across the entire submodel. However, compared to the continuum model the selected submodel is very small, so that differences in the displacement field are likely to have only a minor influence on the fracture processes in the investigated area. Nonetheless, this method can be generalized in order to simulate the real displacement field by considering the displacements calculated in the continuum model as boundary conditions in the discontinuum model.

Discrete modeling was performed on a cube with a length of 50 mm, consisting of 1954 polyhedral shaped elements (Fig. 38). The average grain size of 4mm is the same size as was

used during the calibration of the constitutive material parameters. The constitutive models used are described in chapter 2.3.3 and the numerical parameters are reported in Table 2. In order to avoid any numerical effects due to the boundary conditions, the discrete model is hosted in a continuum far field block (Fig. 39). The dimensions of the block are five times larger than the discrete model. The far field block has the same material parameters as the crystals of the discrete model. The contact surfaces between both models are modeled like the joints of the discrete model. The role of the far field block is to transmit stresses to the discrete model. Therefore**,** the stresses of the monitored zones coming from the continuum mechanical analysis are applied at the boundary faces of the far field block (Fig. 39)**.** σ_{xx} is applied at the boundary faces located in x-direction. Respectively, σ_{YY} and σ_{zz} are applied at the corresponding boundary faces in y- and z-direction.

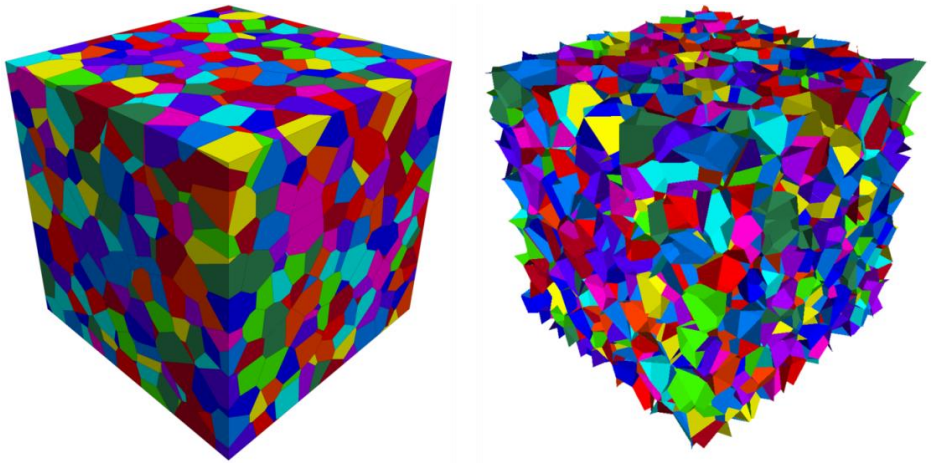

Fig. 38: **3DEC rock salt samples composed of polyhedral shaped elements showing a) the volume elements and b) the grain boundaries.**

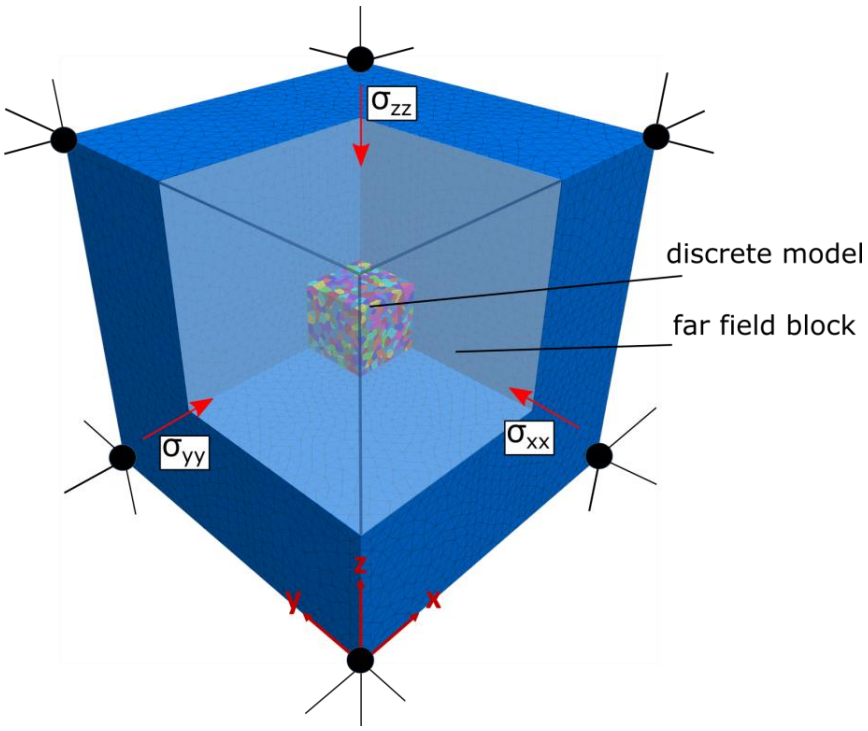

Fig. 39: Continuum far field block used to enclose the discrete model consisting of polyhedral elements. Parts of the far field are hidden for illustration.

Since the shear stresses are zero in the domain of interest, they are not illustrated in Fig. 39. The model is also constrained at the eight corners to avoid displacements which occur during the computational stepping necessary to reach the equilibrium. The outer corners are fixed with roller boundaries in all three directions. Initial stresses were first assigned in the model to simulate the lithostatic stress of the overburden rocks. The discrete model was allowed to reach an equilibrium state under the action of the initial and boundary stresses. Since 3DEC is an explicit code, several computational steps are required to reach an equilibrium state (Itasca, 2013). The differential stress was then changed according to the calculated zone stresses derived from the continuum modeling. This corresponds to the stress redistribution which occurs during the excavation of the drift. During the computation, the stresses in the discrete model converge from the values of the initial stresses to those of the boundary stresses. Monitoring points are located at the center of each face and at the center of the discrete model (Fig. 40). At the faces located in x-direction, i.e. at x = 0 cm and x = 5 cm, displacements in x-direction and σ_{xx}-stress components will be monitored. Respectively, displacements and stress components in y-direction and z-direction will be monitored at the faces located in y-direction and z-direction.

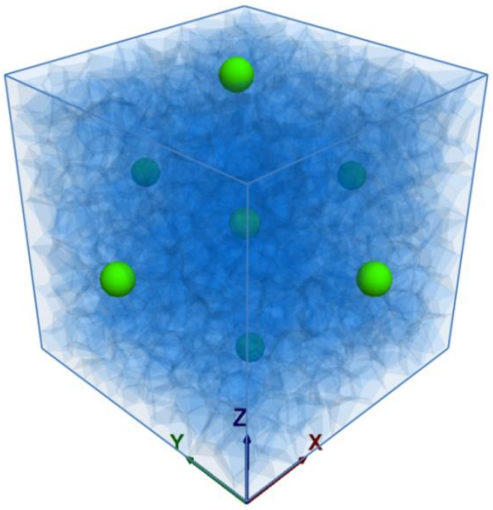

Fig. 40: Monitoring points used to determine the stresses and displacments in the discrete model during simulation.

The simulation results of the discrete modeling are presented exemplarily for continuum zone stresses at a depth of 1.5 m starting from the drift contour (Fig. 35). The initial stress state in this zone is: $\sigma_{xx} = \sigma_{YY} = -22$ MPa and $\sigma_{zz} = -27$ MPa. After excavation, the secondary stress state in the same zone is equal to: $\sigma_{xx} = -5.37$ MPa, $\sigma_{YY} = -20.6$ MPa and $\sigma_{zz} = -37.8$ MPa. Fig. 41 shows the stresses and the displacements in the discrete model at the measuring points after initializing of the stresses before and after excavation. Initial stresses are equal to the stresses monitored in the continuum mechanical approach. Stresses observed after excavation, however, differ somewhat from the continuum mechanical solution. For instance, the σ_{zz}-stress component is equal to about -40 MPa at the boundary faces of the discrete model but is only -30 MPa in the model center compared with -37.5 MPa calculated in this zone with Flac3D after excavation. This stress discrepancy can be explained by the stress redistribution in the discrete model which occurs when plastic deformation takes place both in the Voronoi elements and in the joints between the polyhedral elements.

The evaluation of the occurred deformations in Fig. 41 shows that the discrete model is compressed symmetrically in x- and z-direction due to the acting stresses in these directions. The deformations increase exponentially in the model up to reach a plateau where the model is in equilibrium. No deformations occur in y-direction because the model is not stressed in this direction: the σ_{YY}-stress component remains practically unchanged during the excavation (from -22 MPa to -20.6 MPa). It can also be seen that the center of the model does not move in any direction since this point is the center of symmetry of all stresses acting in the model.

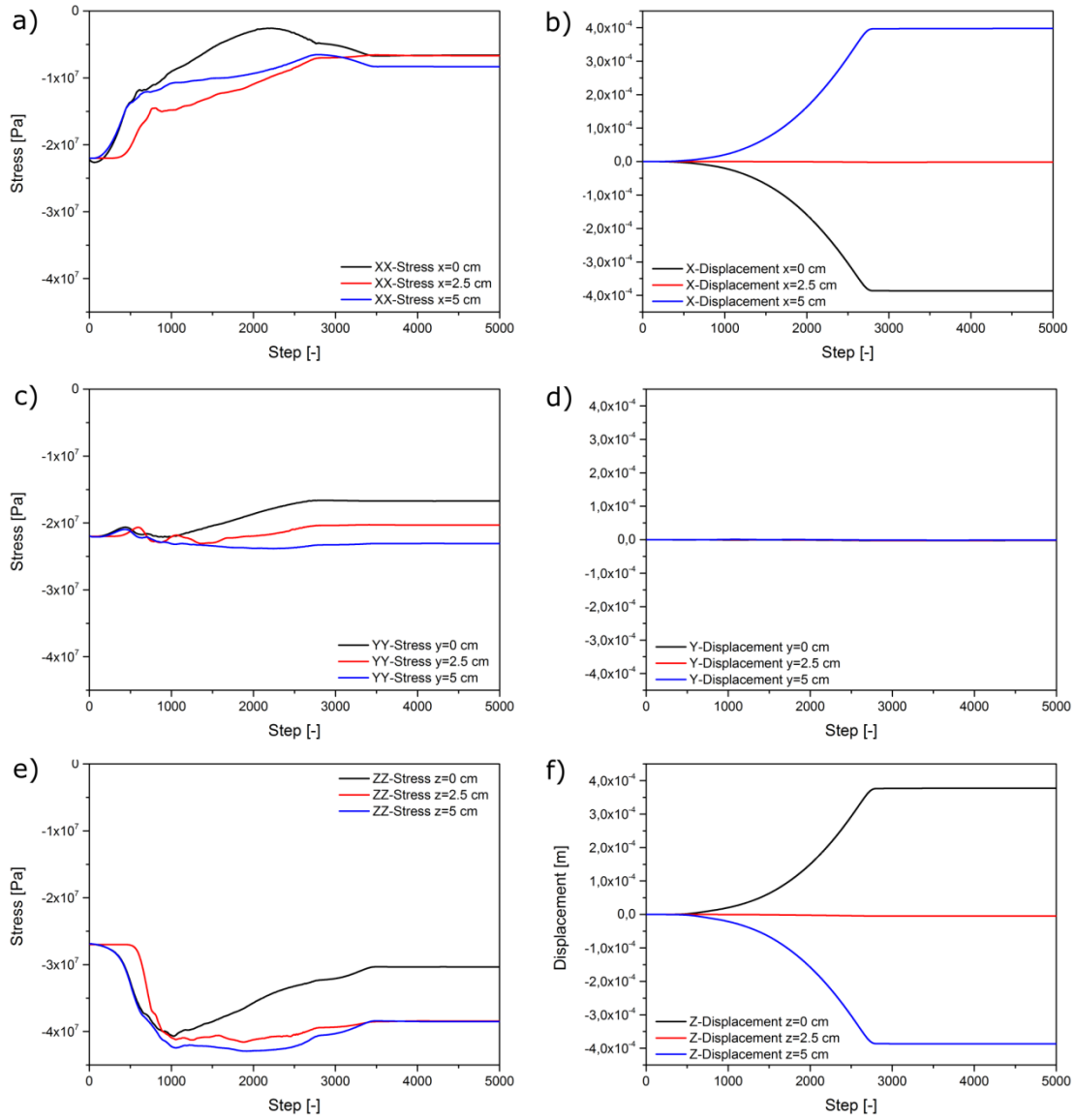

Fig. 41: **Displacement and stress histories at three measuring points within the discrete model consisting of polyhedral elements.**

The fracture network due to the applied stress at a depth of 1.5 m is shown in Fig. 42. The polygonal grain boundaries are subdivided into triangular faces due to the finite difference discretization. A fracture was defined as soon as one of the three knots of a triangular face failed using the internal FISH language. The examinations of the crack pat-

terns show that an important amount of cracks are more or less oriented along the y-z-plane due to the orientation quite perpendicular to the x-direction. Thus, it can be concluded that the resulting damage in the discrete model is anisotropic. The anisotropy is oriented along the z-axis. This corresponds to the direction of the highest stress applied at the boundary of the model. In the case analyzed here, the σ_{zz}-stress component is the minimum principal stress due to the absence of a shear stress component in the considered zone. This is in agreement with observations where the fractures of the EDZ are principally orientated along the direction of the minimum principle stress (Popp et al. 2001).

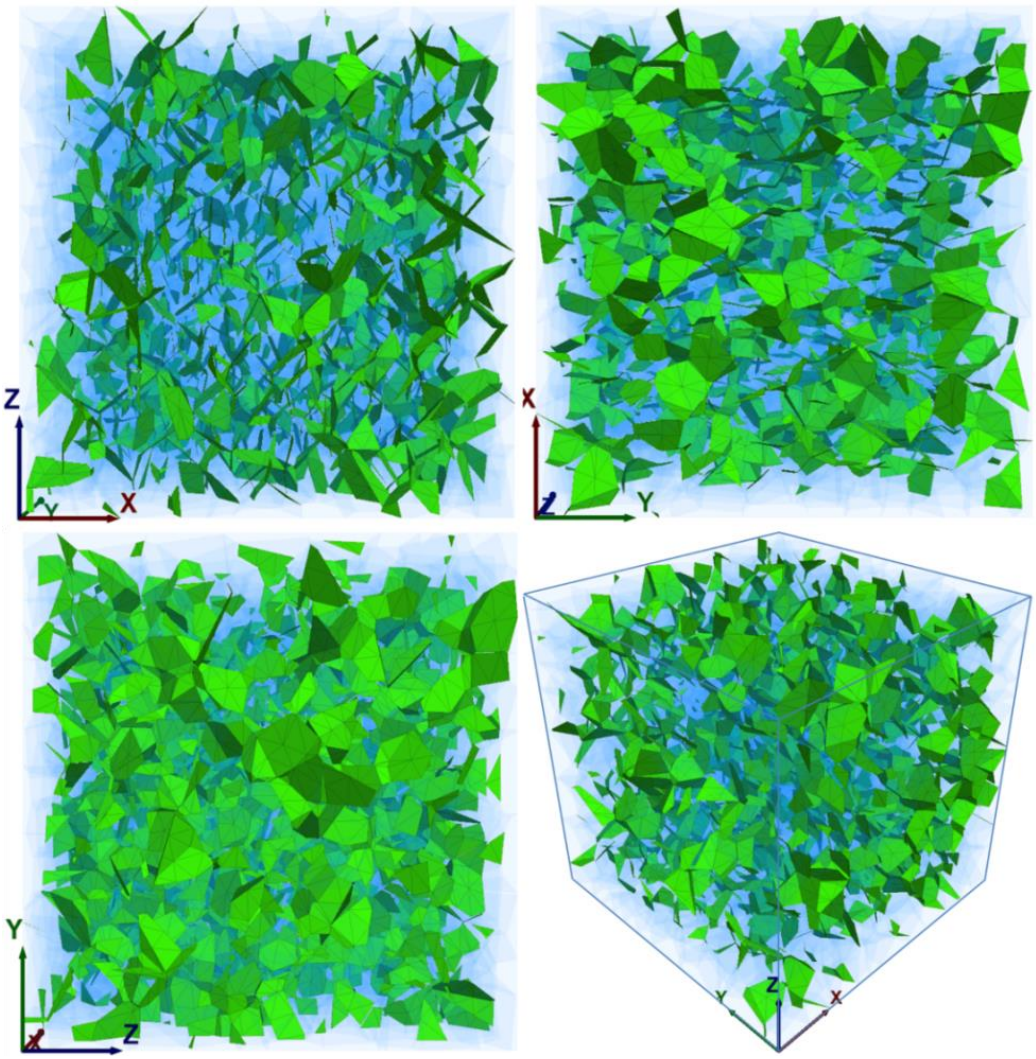

Fig. 42: **Simulated fracture network due to the applied stress state at a depth of 1.5 m from the drift contour.**

Simulated fracture networks for different depths according to the measuring points are shown in Fig. 43. It could be shown that the region damaged the most is at 0.5 m depth. Between 2-3 m depth the fractures decrease considerably but there are still a few fractures at a depth of 4 m.

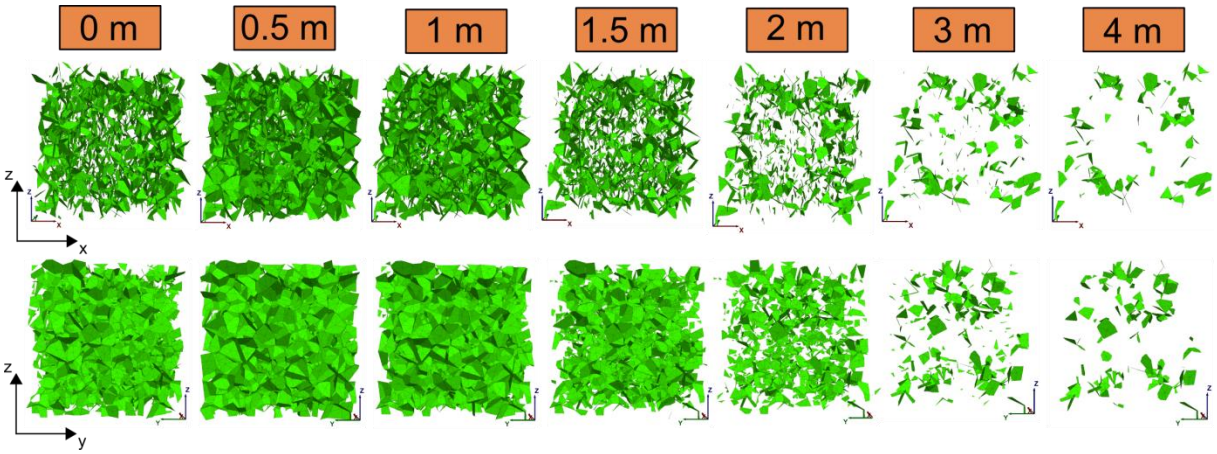

Fig. 43: Simulated fracture networks in the EDZ using the DEM.

However, it must be taken into account that the simulation of the fracture processes inside the EDZ is based solely on uniaxial compression tests in order to calibrate the parameters used in the constitutive models. Thus, it only provides satisfactory results for relatively small external restraints as usually observed at the outer contour zone. Parameters need to be calibrated under triaxial stress conditions usually observed at greater contour depths. Therefore, the question arises how well the simulated fracture system coincides with the one observed in the EDZ, especially at greater depth. A quantitative and qualitative comparison with in-situ fracture networks was not carried out due to a lack of information. However, based on visual observations (scaling at the outer contour), it is known that the fracture system in the EDZ is anisotropic in most cases. Furthermore, a simple comparison with the continuum mechanical solution was conducted. The octahedral shear stress was calculated for the monitored points in the continuum model and related to the dilatancy boundary proposed by Cristescu & Hunsche (1998). The dilatancy boundary gives information about the beginning of fracturing in the EDZ. It turns out that the damage extends to a depth of 2 m and the greatest damage is to be expected at a depth of nearly 1 m, which is in good agreement with the DEM solution (Fig. 44).

3.3 Discussion

The objective was to simulate the fracturing processes inside the EDZ using the DEM approach. For this purpose, the excavation of a drift was first simulated with continuum mechanical approaches and zone stresses were recorded for certain depths of the EDZ. Zone stresses were then transmitted as boundary stresses onto a DEM model comprising polyhedral elements.

The results of the DEM modeling shows a fracture-induced anisotropy, and fractures are oriented parallel to the maximum principal stress. It could be shown that the region damaged the most is at a depth of 0.5 m. Between 2-3 m depth the fracture density decreases considerably. The results are in good agreement with simulations performed with continuum mechanical approaches and using the dilatancy boundary after Cristescu

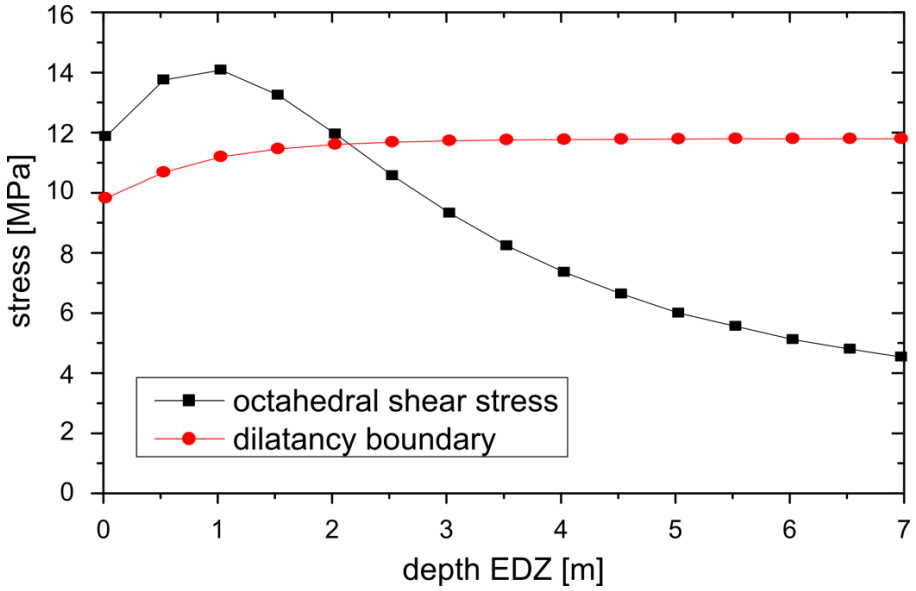

Fig. 44: **Calculated octrahedral shear stresses for the monitored points in the continuum model and dilatancy boundary after Cristescu & Hunsche (1998).**

& Hunsche (1998) to describe the damage in rock salt. However, it should be considered that the stresses derived from continuum modeling and transferred to the DEM model are based on a linear elastic solution. The stresses transferred to the DEM model do not consider the stress rearrangement due to plastic or viscous processes. The use of linear elasticity leads to high stresses as they actually occur in the EDZ. Furthermore, it must be taken into account that the DEM model only provides plastic deformation due to inter granular cracking and the plastic deformation of grains. However, the impact of time-dependent (viscous) processes was not incorporated in this simulation (chap. 2.2)

4 Investigating the Hydraulic Behavior of the Excavation Damaged Zone

So far, the mechanical deterioration of rock salt at grain scale was simulated using the discrete element method in combination with polyhedral elements. The models were mechanically loaded using stress boundary conditions comparable to those of an EDZ. Fairly anisotropic fracture networks were simulated this way (chap. 3.2). In addition to mechanical processes, however, the hydraulic processes must be considered for a comprehensive evaluation of the EDZ. As discussed earlier, the permeability increase in the EDZ is mainly caused by microfractures, which can compromise the sealing function of the originally tight rock salt. Therefore, the specification of adequate permeability values is particularly important since it provides information about major pathways for fluid flow.

The following chapter introduces a method to upscale the information gained from discontinuum modeling to the macroscale since the larger number of fractures makes the discrete approach less efficient for large-scale modeling. By calculating the permeability tensor, it is investigated if the flow of a discontinuum model with fractures explicitly represented can be simulated using continuum modeling approaches. The permeability tensor provides information about the direction and magnitude of the major and minor component of flow. This allows the specification of directionally dependent (anisotropic) permeability properties that can be used as input parameters for continuum models simulating the fluid flow at larger scales. The methodical approach to obtain the permeability tensor is first validated on a polyhedral model where the fractures are completely interconnected (chap. 4.1). Subsequently, the fracture networks provided in chap. 3.2 were used for hydraulic simulations to calculate the hydraulic conductivity tensor (chapter 4.2). However, due to the complex nature of the fracture network, it is not always certain that every fracture system can be simulated by an equivalent porous medium (Oda, 1986). A fracture network behaves more like a porous medium if a sufficient number of discontinuities are present (Long et al., 1982). In addition to the upscaling concept, the connectivity of the fracture network must also be considered. If the fracture network is not at all connected to build a continuous path for fluid flow, a permeability tensor cannot be defined since the global permeability is zero (Bear et al., 2012). Therefore, it is especially interesting to see if the hydraulic tensor with increasing depth contour and thus decreasing fracture density can be determined.

4.1 Upscaling of Hydraulic Data

In practice, discrete approaches such as the Discrete Fracture Network (DFN) analysis are generally used to simulate fluid flow in fractured media (e.g. Jing, 2003). It is a widely accepted approach since it is, so far, an irreplaceable tool for modeling fluid flow in the near-field with fractures explicitly represented (Min et al., 2004). Fractures that have already been generated using polyhedral models (see chapter 3.2) can be regarded as such a DFN. However, when the domain of interest increases, the larger number of fracture makes the discrete approach less efficient due to computational constraints (Jing, 2003). In this case, the application of continuum approaches becomes the method of choice. Thus, using the DFN approach, the hydraulic behavior of the EDZ can only be investigated for near-field problems, whereas simulations to study the entire system have to use continuum mechanical

approaches. Methods are needed to upscale the hydraulic behavior. The commonly used method is based on the following principles: the fluid flow of a given model with fractures explicitly represented is similar to that through a continuum model having equivalent hydraulic properties (equivalent porous medium, e.g. Long et al. (1982); Oda (1986); Renard & De Marsily (1997); Panda & Kulatilake (1999); Niemi et al. (2000); Min et al. (2004)). Using continuum approaches as a DFN equivalent is, however, only feasible when the following requirements are met. First, the Representative Elementary Volume (REV) of the fracture network regarding the hydraulic behavior must exist and be known. Second, the derived equivalent hydraulic properties of the DFN can be approximated by a second-rank, symmetric, positive-definite hydraulic conductivity tensor (Long et al., 1982; Niemi et al., 2000).

The REV of a fracture network is the smallest volume over which the studied parameter, in this case the hydraulic conductivity, yields a constant value (Bear, 1972). Since the fluid flow in a fracture network is highly scale-dependent, the hydraulic conductivity is usually studied for various DFN models and with increasing model size to determine the REV (Fig. 45). The variances of calculated permeability components become smaller as the model size increases, and the permeability values maintain constant ranges after a certain size (Min et al., 2004). However, the simulations carried out in chapter 3 have already reached the limit of practical computational effort. An increase in size or the simulation of several DFN models for studying the hydraulic properties is therefore not feasible. Therefore, the assumption was made that the generated DFN models meet the REV criteria in order to investigate equivalent hydraulic properties. When determining equivalent hydraulic properties of fractured media for large scale modeling, the hydraulic conductivity tensor is a key parameter.

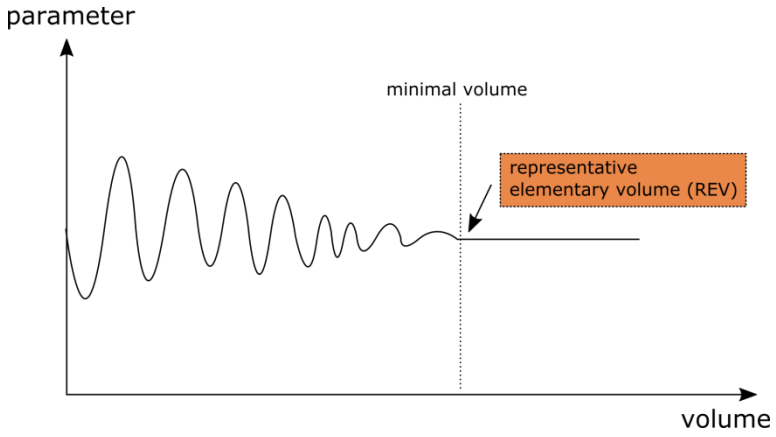

Fig. 45: Statistical definition of a representative elementary volume (REV).

4.1.1 3D Hydraulic Conductivity Tensor as a Criterion for Continuum Behavior

For anisotropic porous media, the relationship between the specific discharge (or Darcy velocity vector) q_i and the hydraulic gradient J_i is given by Darcy's law (Darcy, 1856):

$$q_i = K_{ij} \cdot J_i \qquad \textbf{(12)}$$

where K_{ij} are the components of the hydraulic conductivity tensor. The components of the hydraulic gradient J_i can be interpreted as $\delta h/\delta i$, which is the difference in water head across the length L. For three dimensions and an anisotropic porous medium, the hydraulic conductivity tensor has to be symmetric and plots an ellipsoid with the major and minor axes corresponding to the direction of minimum and maximum permeability (Niemi et al., 2000). In order to check whether the generated DFN behaves as a continuum, the calculated directional permeability must be investigated. The directional permeability is determined by simulating the flow through a DFN under different head directions and by determining the effective hydraulic conductivity based on the (one-dimensional) Darcy law (Niemi et al., 2000). If the calculated directional permeability is plotted for each head direction and it can be represented approximately by a symmetric tensor, then continuum approaches can be used. However, since the fluid flow is largely influenced by the complexity and heterogeneity of the DFN, there is no guarantee that the system behaves as a continuum (Kulatilake & Panda, 2000).

4.1.2 Directional Permeability

As can be seen from the Darcy equation, the two vectors q_i and J_i do not necessarily point in the same direction. Thus, the hydraulic conductivity can be calculated either in the direction of the discharge vector q_i or in the direction of the hydraulic gradient J_i. Bear (1972) illustrates the derivation for conductivity both in the direction of discharge and in the direction of the hydraulic gradient. In this paper, the directional conductivity in the direction of J_i is used and is briefly presented in the following. After Bear (1972), the directional hydraulic conductivity K_J is a scalar physical quantity that describes the ratio between the magnitude of the discharge q_i in the direction of the gradient and the gradient itself:

$$K_J = \frac{|q|cos\theta}{|J|} \qquad |q|cos\theta = K_J|J| \tag{13}$$

where $|J|$ is the magnitude of the hydraulic gradient and $cos\theta$ is the angle between the vectors q_i and J_i (Bear, 1972).

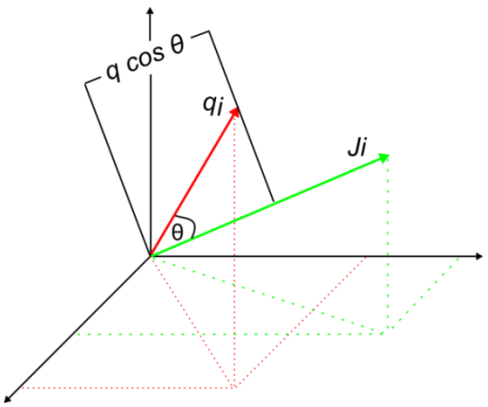

Fig. 46: Relationship between q_i and J_i for calculating the directional hydraulic conductivity

The term $|q|\ cos\theta$ is the component of discharge q_i in the direction of J_i. Using the product $q_i \cdot n_i$ instead, where n_i is a unit vector in the direction of the gradient and substituting eq. (12)

in (13), we get the relationship between the directional conductivity and the hydraulic conductivity tensor (Long et al., 1982):

$$K_J(n_i) = n_j K_{ij} n_i \quad \textbf{(14)}$$

In order to check whether the DFN behaves as a continuum, the calculated directional conductivity for different head directions must be approximated by an ellipsoid with the three principal conductivity values K_x, K_y and K_z (Long et al., 1982):

$$\frac{x^2}{1/K_x} + \frac{y^2}{1/K_y} + \frac{z^2}{1/K_z} = 1 \quad \textbf{(15)}$$

In this case, the reciprocals of square roots of the directional conductivity $K_x^{-1/2}$, $K_y^{-1/2}$ and $K_z^{-1/2}$ are the semi axes of the ellipsoid. The major axis of the ellipsoid is in the direction of minimum conductivity for hydraulic conductivity measurement in the direction of the hydraulic gradient Fig. 47.

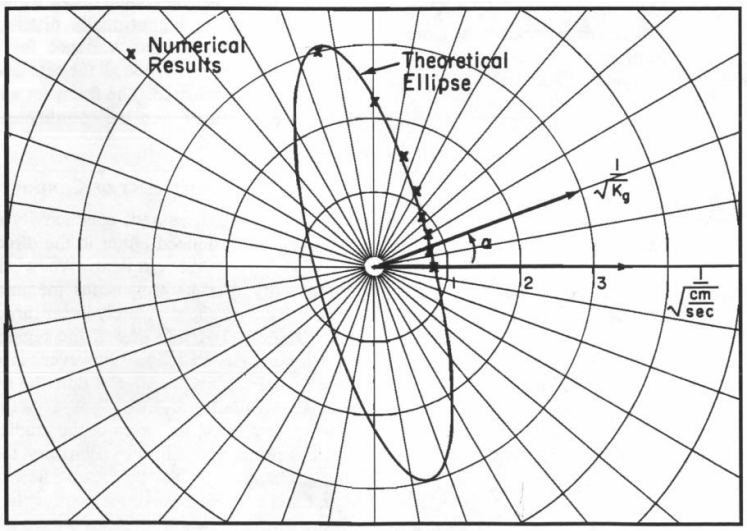

Fig. 47: Comparison between the theoretical permeability ellipse and the calculated numerical results (Long et al., 1982).

Measurements of the directional permeability under different head directions can be used to find the equivalent permeability tensor for a given DFN. A number of different methods have been used in the past to evaluate the hydraulic conductivity tensor of a rectangular DFN model. Many of the methods have in common that fictitious hydraulic boundary conditions are used in order to evaluate the flow discharge. One method uses different but constant hydraulic heads between opposite boundaries, whereas the other two (2D) or four (3D) boundaries of the model were specified as no flux boundaries (e.g. Panda & Kulatilake, 1999; Wang et al., 2002) (Fig. 48a).

A disadvantage of this method is that impermeable boundaries provide insufficient information about the flow behavior (Long et al., 1982). Another method consists of different but constant head conditions on opposite sides, but using linearly varying head boundaries along the other sides (e.g. Long et al., 1982; Oda, 1986; Zhang et al., 1996) (Fig. 48b).

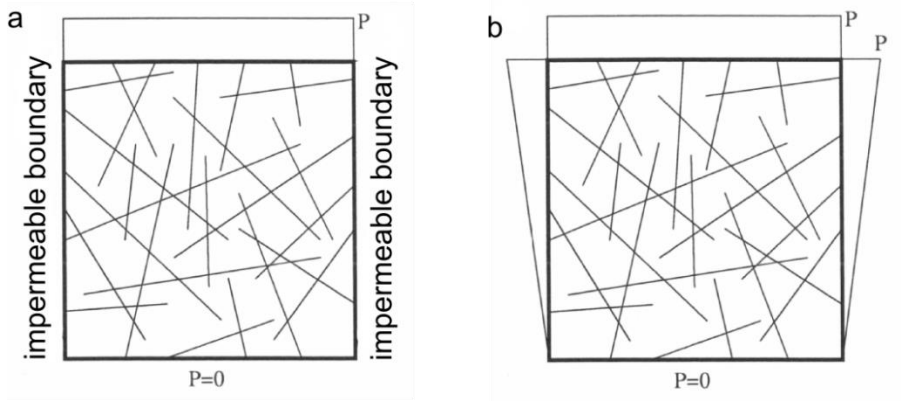

Fig. 48: **Hydraulic boundary conditions with a) impermeable lateral boundaries, and b) two different but constant head conditions on opposite sides and linearly varying head boundaries along the other sides.**

The drawback associated with this approach is that the hydraulic gradient J_i is generally normal to the surfaces having the different but constant head conditions. Thus, the conductivity in any direction can only be measured by cropping and rotating smaller DFN models out of a larger DFN generation region (Fig. 49).

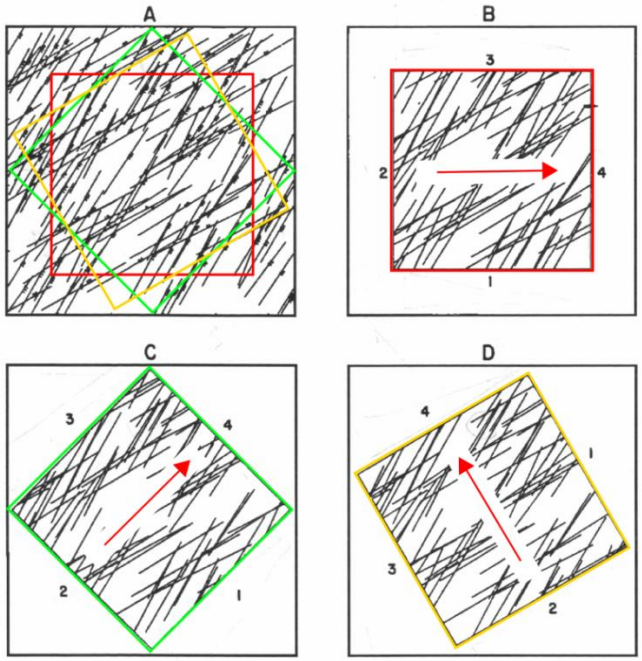

Fig. 49: Generation of different flow regions by cropping and rotating smaller DFN models out of a larger region. Arrow marks the hydraulic head direction (modified after Long et al., (1982)).

Contrary to stochastically generated DFN models, cropping smaller DFN out of a larger region can cause problems for a given DFN model. Therefore, the directional permeability was evaluated rather by changing the hydraulic boundary conditions than by rotating the model (e.g. Jackson et al., 2000; Blum et al., 2007).

Hydraulic boundary conditions were changed using linearly varying heads according to the superposition principle to generate a unit hydraulic gradient vector in any direction. To obtain directional permeability values for different head directions, the gradient vector was rotated counterclockwise from 0° to 150° in 30° steps on the x-y plane starting in the direction of the

x-axis and assuming a right-handed Cartesian coordinate system. This procedure was carried out for different inclination angles (angle between z-direction and the gradient vector) from 90° to 0° in 30° steps in order to characterize the fluid flow of the fracture system for various hydraulic gradients (Fig. 50).

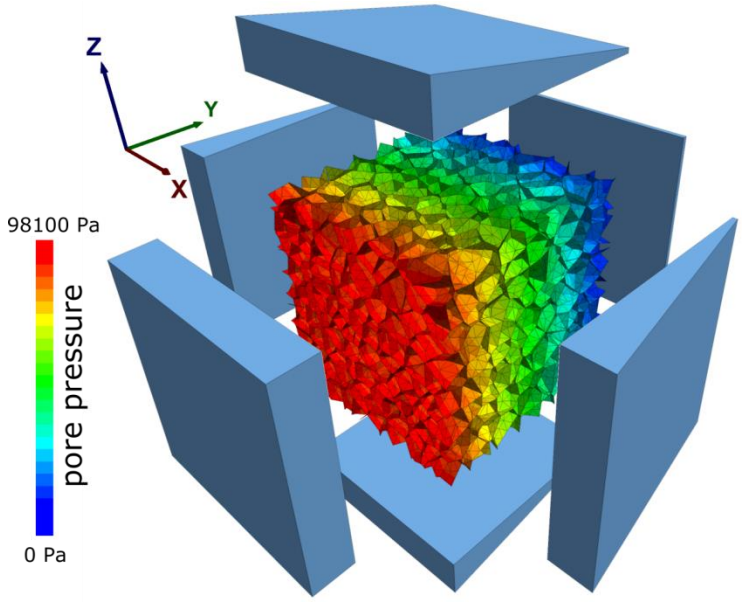

Fig. 50: **Hydraulic gradient vector in y-direction as an example of the hydraulic head boundaries with linearly varying hydraulic heads along the six sides of the cube. A unit head gradient was employed (9.81 Pa/m).**

When evaluating the directional permeability K_J, the components of the Darcy velocity vector q_i need to be determined. This is usually accomplished by measuring the flow rate Q along the six cross-sectional areas A of the cube using the following relationship (Niemi et al., 2000):

$$a_{ji} \cdot q_i = \frac{Q_j}{A_j} \quad j: [1;6]\, i: [1;3] \tag{16}$$

where a_{jx}, a_{jy} and a_{jz} represent the components of the unit vector normal to surface j. The approach used in this study consists of taking the average Darcy velocity vector q_i over the associated crack and matrix volume proposed by Oda (1985):

$$\overline{q_i} = \frac{1}{V}\left(\int_{V(crack)}^{\cdot} q_{i(crack)} \cdot dV_{(crack)} + \int_{V(matrix)}^{\cdot} q_{i(matrix)} \cdot dV_{(matrix)}\right) \tag{17}$$

Assuming the matrix (salt grains) is impermeable and the water flows only through intergranular cracks, eq. (17) becomes:

$$\overline{q_i} = \frac{1}{V}\left(\int_{V(crack)}^{\cdot} q_{i(crack)} \cdot dV_{(crack)}\right) \tag{18}$$

The approach can be used as an easy and robust alternative for calculating flows at the boundaries of the block.

In 3DEC, fluid flow is represented by flow through so-called flow planes. The flow planes are interfaces that separate the blocks and form a system of planar polygons within three-dimensional space (Fig. 51). Flow planes are subdivided into flow zones and flow knots, which is due to the finite difference discretization. The local Darcy velocity vector (specific discharge) was determined for each flow zone using the internal FISH flow zone function *flowrate.* According to Itasca (2013) the function *flowrate* has the unit m^3/s and gives the volumetric discharge (total discharge) Q_i per unit width w of the plates in a zone according to the cubic law:

$$Q_{i;zone} = \frac{\delta_f \cdot g \cdot b^3}{12\mu} \cdot J_i \qquad \textbf{(19)}$$

In order to get the Darcy velocity vector q_i (m/s), the volumetric discharge Q_i has to be divided by the cross sectional area A_i of the zone:

$$qi = \frac{Q_i}{A_i};\ \ A_i = b \cdot w \qquad [b = aperture\ zone;\ w = 1m] \qquad \textbf{(20)}$$

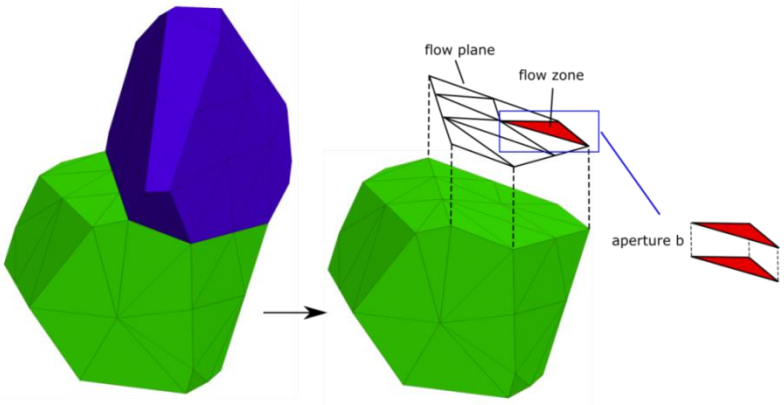

Fig. 51: 3DEC relevant elements for calculating the Darcy velocity vector q_i.

Knowing the Darcy velocity vector q_i and the hydraulic gradient J_i, the directional permeability K_J can be calculated using eq. (13). In order to graphically check whether the DFN behaves as a continuum, the reciprocals of the square roots of the calculated directional permeability $1/\sqrt{K_J}$ were plotted in a polar coordinate system. Furthermore, an average hydraulic conductivity tensor based on the calculated directional permeability K_J was calculated using the method of least squares by minimizing the following expression:

$$\text{MIN}\, f(k_{ij}) := \sum_{n=1}^{N} (K_j^n - n_j K_{ij} n_i)^2 \qquad \textbf{(21)}$$

where N denotes the number of hydraulic head directions. This is followed by a diagonalization of the calculated hydraulic conductivity tensor in order to determine the three principal

values and the three corresponding directions. The procedure for finding the diagonalized tensor K_{ij}^D is as follows (SPE, 2015):

- Find the eigenvalues λ_i *i:[1,n]* of K_{ij} from the eigenvalue equation $det(K_{ij}-\lambda E_n)=0$, where E_n is the n-dimensional identity matrix;
- Find the eigenvectors u_i of the calculated eigenvalues λ_i ;
- Form the similarity transformation matrix with the eigenvectors as columns (u_i^T) and calculate the diagonalized tensor K_{ij}^D. The diagonal values are the eigenvalues corresponding to the eigenvectors.

Substituting the three principal conductivity values K_x, K_y and K_z of the average hydraulic conductivity tensor in eq. (12) and plotting the permeability tensor ellipsoid on the polar diagram containing the directional permeability values shows how well both values fit together. It allows the conclusion that the calculated directional conductivities can be approximated by a symmetric conductivity tensor, and therefore corresponding continuum behavior can be assumed (see Fig. 47). Evaluating the direction in which flow takes place can also be solved graphically by plotting the Darcy velocity vector perpendicular to the ellipsoid surface in the direction of the outward normal (Liakopoulos, 1965). The hydraulic gradient vector J_i and the Darcy velocity vector q_i are collinear along the three principal directions of the ellipsoid.

4.1.3 Validation of the Numerical Method

The validation of the methodical approach was carried out on simple models, where it was possible to analytically solve the fluid flow. For the flow simulations, a constant water density of 1000 kg/m^3, gravity acceleration of 9.81 m/s^2 and a dynamic viscosity of 0.001 kg/ms were assumed. Fig. 52 illustrates, as an example, the determination of the hydraulic conductivity tensor on a simple model having just two fractures. Anisotropy with regard to the fluid flow was created by implementing an orthogonal fracture system with different apertures of fracture planes in each direction. It can be shown that the calculated hydraulic values correspond exactly with the analytic solution.

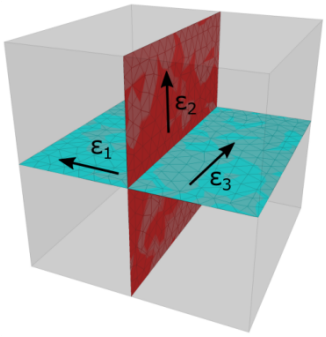

principal direction of specific discharge	principal values of hydr. conduc. tensor k_{ij}	
	analytic	numerical (over crack volume)
ε_1	1,635E-05 m/s	1,635E-05 m/s
ε_2	2,044E-06 m/s	2,044E-06 m/s
ε_3	1,839E-05 m/s	1,839E-05 m/s

Fig. 52: **Principal values of the hydraulic conductivity tensor k_{ij} based on the analytical and numerical solution and using a fracture system with fracture planes arranged orthogonally to each other and parallel to the faces of the cube.**

However, when rotating the fracture system towards the diagonal of the cube, there is a geometrically caused increase of the crack volume. Due to the approach used (volume integral over the crack system), an increase in the crack volume results in larger hydraulic conductivity values compared with the rectangular model (Fig. 53).

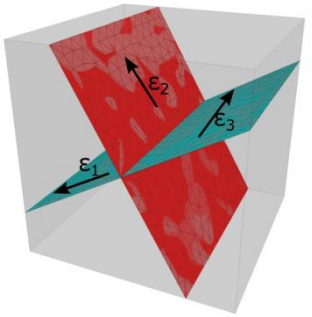

principal direction of specific discharge	principal values of hydr. conduc. tensor k_{ij} numerical (over crack volume)
ε_1	1,886E-05 m/s
ε_2	2,361E-06 m/s
ε_3	2,124E-05 m/s

Fig. 53: Principal values of the hydraulic conductivity tensor k_{ij} based on the numerical solution and using a rotated fracture.

In order to avoid the influence of the cube geometry on the simulation results and to ensure a consistency among the hydraulic calculations, the hydraulic evaluation is therefore carried out within a measuring sphere (Fig. 54).

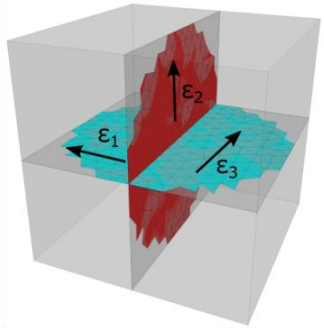

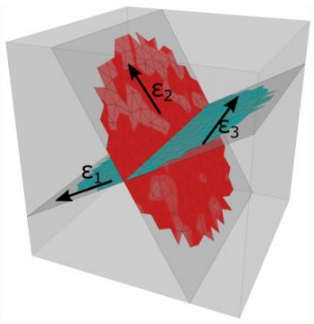

principal direction of specific discharge	principal values of hydr. conduc. tensor k_{ij} numerical (over sphere volume)	principal values of hydr. conduc. tensor k_{ij} numerical (over sphere volume)
ε_1	2,453E-05 m/s	2,453E-05 m/s
ε_2	3,083E-06 m/s	3,134E-06 m/s
ε_3	2,771E-05 m/s	2,774E-05 m/s

Fig. 54: Principal values of the hydraulic conductivity tensor k_{ij} based on the numerical solution. To determine the average Darcy velocity vector only fluid zones lying within a sphere were used for calculation.

In a next step, it was checked whether the polyhedral models are also suitable for hydraulic modeling. However, the polyhedral models were no longer suitable for analytical calculation so that the hydraulic results were only checked for plausibility. First, a polyhedral model was tested in which all the faces between the polyhedral elements are open and have a constant

aperture width of 100 μm. Fig. 55 shows the model used and the calculated hydraulic conductivity tensor. The tensor ellipsoid approximates a sphere, which indicates that the fracture topology has no influence on the direction of permeability. The Voronoi diagram behaves hydraulically isotropic due to a fairly random orientation of fracture planes. Thus, a geometry-induced anisotropy due to a preferred orientation of polyhedral elements can be excluded.

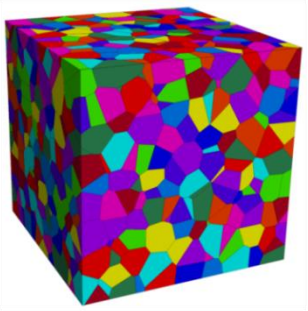

principal direction of specific discharge	principal values of conduc. tensor k_{ij}
ε_1	3,788E-04 m/s
ε_2	3,764E-04 m/s
ε_3	3,771E-04 m/s

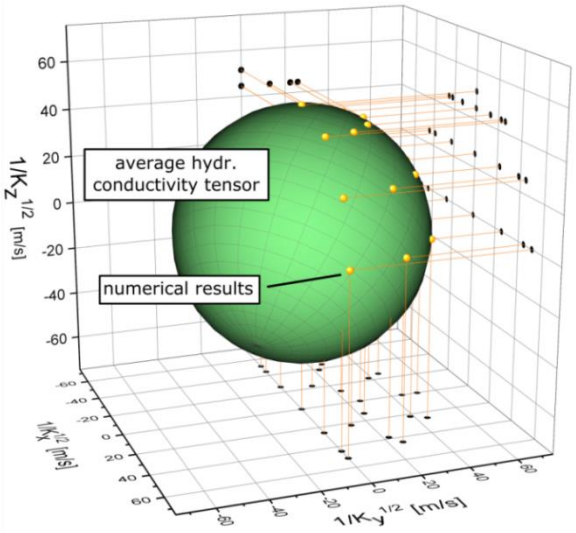

Fig. 55: Determination of the conductivity tensor for an isotropic Voronoi model.

In the second test, the fracture properties were changed in order to cause a preferred fluid flow direction. The aperture of fracture planes having a normal vector n = (0, 1, 2) and a predefined angle tolerance of 40° were halved from 100 to 50 μm (blue colored fracture planes, Fig. 56).

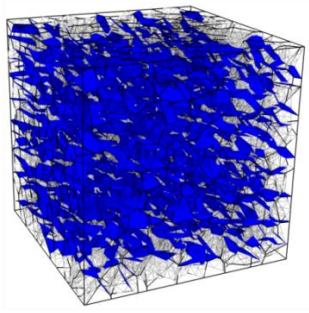

principal direction of specific discharge	principal values of conduc. tensor k_{ij}
ε_1	3,412E-04 m/s
ε_2	2,598E-04 m/s
ε_3	2,618E-04 m/s

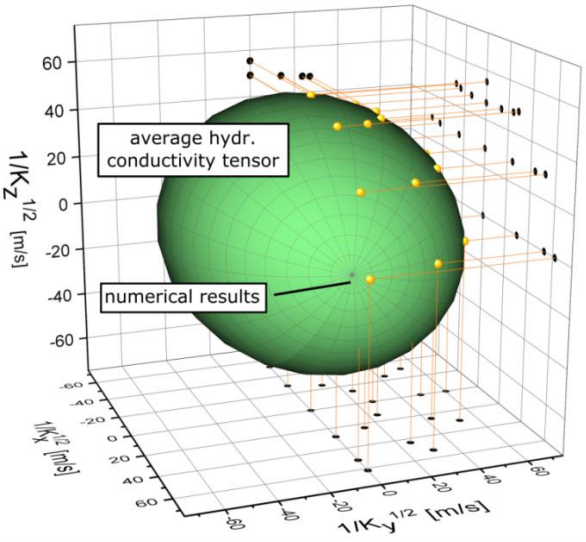

Fig. 56: Determination of the hydraulic conductivity tensor for an anisotropic Voronoi model. The anisotropy was induced by reducing the aperture of fracture planes having a normal vector n = (0, 1, 2) and an angle tolerance of 40° (blue colored fractures).

Since the fracture aperture has a major effect on the permeability following the cubic law, this should induce a distinct anisotropy in the permeability of the fracture network. The tensor ellipsoid clearly indicates the minimum permeability in the direction of the more closed facture planes. The major axis of the ellipsoid is in the direction of minimum conductivity for hydraulic conductivity measurement in the direction of the hydraulic gradient.

4.2 Estimation of Equivalent Hydraulic Properties

The permeability of a DFN depends significantly on the geometry of the fractures (size, orientation and density) as well as the transmissivity of individual fractures (Min et al., 2004). As mentioned earlier, the former was generated using Voronoi models to simulate the fracturing at grain scale. The fluid flow through these individual fractures has not been considered yet, and hydraulic information is needed to derive these properties. The hydraulic calibration of relevant input parameters is generally similar to the procedure used for calibrating the mechanical input parameters: fracture transmissivities are varied until conformity between measured and simulated results is achieved. However, it is very difficult to obtain relevant hydraulic information, and there was no data available that was suitable for calibration. For a first estimate, the aperture was adjusted based on information coming from microscopic investigations. The fluid flow through individual fractures is based on the cubic law where the aperture is the main input parameter controlling the fluid flow. In literature, aperture values derived from microscopical investigations are specified between 1-5 μm (Pusch et al., 2002). Rock salt that was damaged during laboratory testing shows aperture values up to 100 μm but apertures below 10 μm were mainly measured. The cubic law is a simplified model that considers fluid flow between smooth-walled plates. However, natural fractures are more likely to be rough-walled, with walls contacting each other at discrete points (Klimczak et al., 2010). The equivalent aperture that is affected by fluid flow, called hydraulic aperture, is generally smaller than the (mechanical) aperture measured microscopically (Brown, 1987; Hakami & Larsson, 1996). Different approaches of correlating mechanical to hydraulic apertures have been developed (e.g. Bandis et al., 1983; Barton et al., 1985; Witherspoon et al., 1980). However, these approaches are generally based on larger fractures (rock joints) and a transfer to micro fractures at grain scale must be considered with caution. Based on the cubic law, a change of 3 orders of magnitude in aperture would result in a 9 order of magnitude change in permeability (Zhang & Sanderson, 2002). Thus, quantifiable and reliable permeability values depend mainly upon suitable aperture values. The calibration of the hydraulic models is problematic due to a lack of flow input parameters as well as hydraulic data used for validation. Therefore, only a qualitative statement about the permeability of the EDZ within different contour depths is possible

The hydraulic investigations conducted so far only assume a fluid flow along all grain boundaries using constant fracture apertures (chap. 4.1.3). However, it is known that the permeability increase is due to the development of a fracture system. In order to characterize the permeability increase due to the evolution of fractures, the fluid flow in unbroken grain boundaries (contacts) was numerically inhibited using the 3DEC internal command *set crack flow on*. The hydraulic conductivity is thus solely controlled by the formation of new cracks

along the grain boundaries. The maximum allowable hydraulic aperture after a contact has broken was set to 10 μm.

The hydraulic conductivity tensor of the fracture patterns that were introduced in chap. 3.2 were calculated for the depths of 0 m, 0.5 m, 1 m and 1.5 m of the EDZ. At these depths the greatest damage is to be expected (Fig. 43). Fig. 57 shows the ellipsoid calculated and the principal values of the hydraulic conductivity tensor at a depth of 0.5 m from the drift contour.

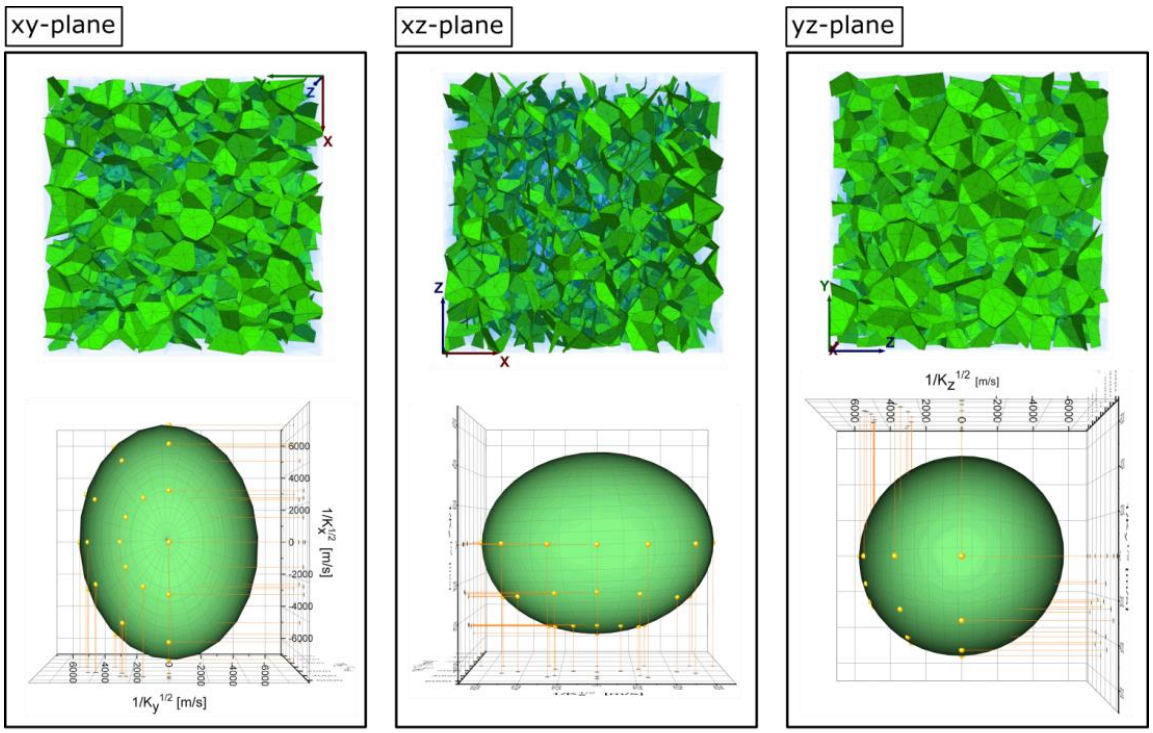

principal direction of specific discharge	principal values of conduc. tensor k_{ij}
ε_1	2,31E-08 m/s
ε_2	3,99E-08 m/s
ε_3	3,80E-08 m/s

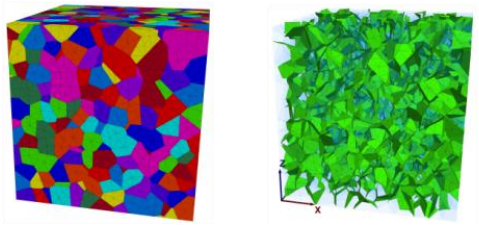

Fig. 57: Calculated hydraulic conductivity tensor ellipsoid at a depth of 0.5 m from the contour and corresponding principal values of the hydraulic conductivity.

Since the calculated numerical results (yellow dots) and the calculated ellipsoid fit together, the hydraulic behavior can be approximated by a symmetric conductivity tensor. Due to the geometry of the fracture pattern, the principle directions of the conductivity tensor are parallel to the orthogonal Cartesian coordinate system. The tensor ellipsoid clearly indicates the maximum permeability (minor axis of the ellipsoid) along the y-z-plane which is in the main direction of the fracture planes and in direction of the highest stress. There is only a small difference between the principle values of the conductivity tensor in the yz-plane and, thus, the conductivity can be assumed as an orthotropic property. The anisotropy factor, defined as the ratio between the maximum and minimum principle conductivity, resulted in a value of 1.73. In order to allow a comparison with values from the literature, the hydraulic conductivity

(m/s) was converted into permeability values (m^2) using the fluid properties given in chap. 4.1.3. The permeability *k* is related to the hydraulic conductivity k_f according to the following equation:

$$k = \frac{k_f \cdot \mu}{\rho_{fluid} \cdot g} \quad \textbf{(22)}$$

where μ is the dynamic viscosity of water, ρ_{fluid} is the density of water and g is the gravity. This lead to permeability values in the order of 10^{-15} m^2 according to Fig. 57. Geotechnical in situ measurements along a drift contour in rock salt using a surface packer give permeability values between 10^{-16} and 10^{-14} m^2 (Bollingerfehr et al. 2011). Wieczorek & Schwarzianeck (2004) specify permeability values between 10^{-16} and 10^{-15} m^2 near the drift surface.

A similar behavior according to the hydraulic conductivity is recognized at a depth of 1 m from the drift contour (Fig. 58). Due to a lower differential stress and thus lower damage, the calculated permeability values are slightly lower.

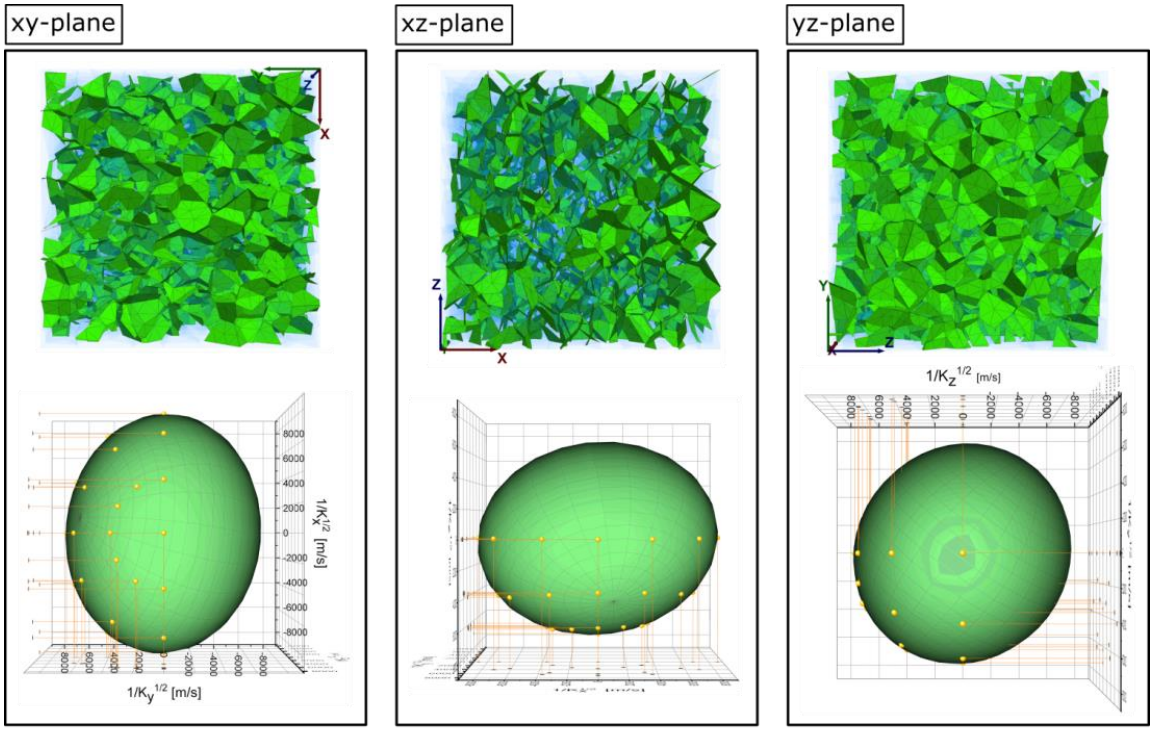

principal direction of specific discharge	principal values of conduc. tensor k_{ij}
ε_1	1,32E-08 m/s
ε_2	2,15E-08 m/s
ε_3	1,95E-08 m/s

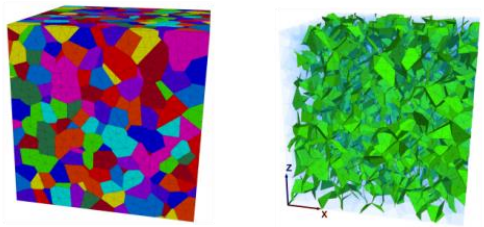

Fig. 58: Calculated hydraulic conductivity tensor ellipsoid at a depth of 1 m from the contour and corresponding principal values of the hydraulic conductivity.

Fig. 59 shows the fracture pattern and the (pore) pressure in the joints at a depth of 0 m from the drift contour. Since the hydraulic gradient is implemented by using boundary conditions, open fractures that are directly connected to the model boundary show an increase in the pore pressure. However, the fracture density is smaller than it was for depths of 0.5 m and 1 m and the fractures no longer connect. A continuous path for fluid flow is absent and the model becomes globally impervious which can be observed by the zero pore pressure regions in the center of the model. Thus, a hydraulic conductivity tensor cannot be specified for depths of 0 m and 2 m from the drift contour due to the non-existing fracture connectivity.

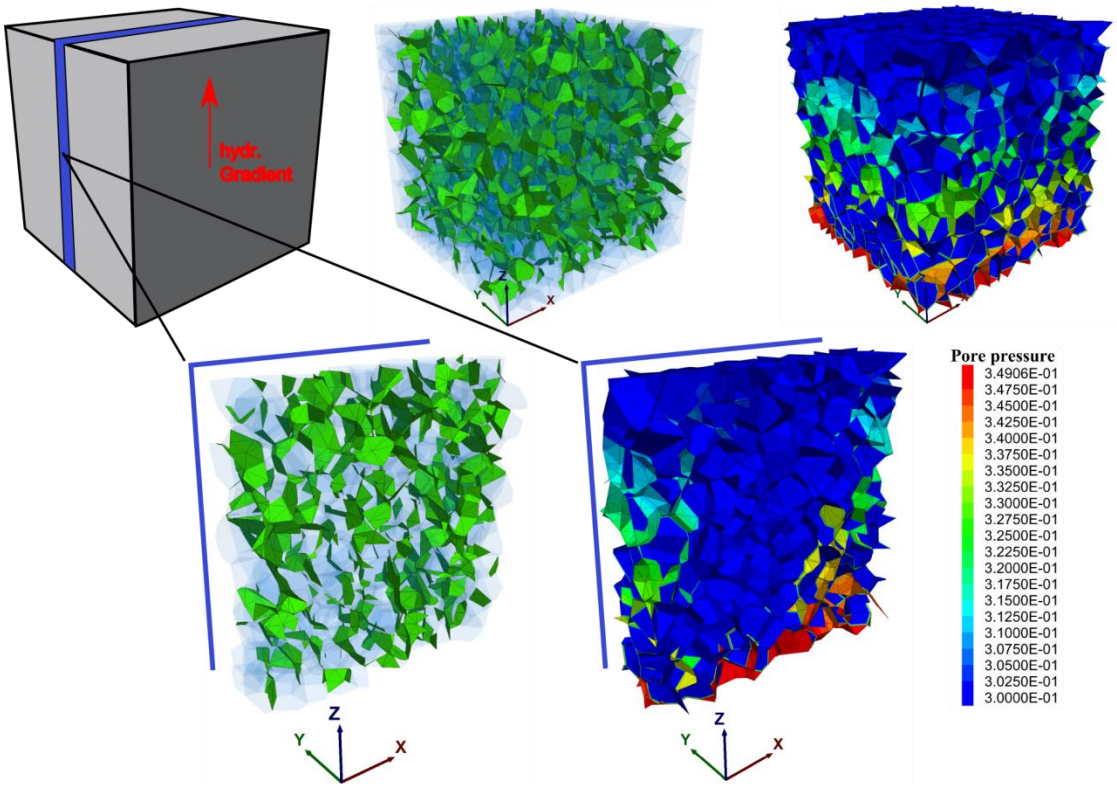

Fig. 59: **Simulated fracture pattern and corresponding pore (or joint) pressure distribution at a depth of 0 m from the drift contour.**

4.3 Discussion

Anisotropic fracture networks were simulated using mechanically calibrated Voronoi models and stress boundary conditions comparable to those in the EDZ. The objective was to characterize the fluid flow in the simulated fracture networks. In order to quantify the fluid flow the hydraulic conductivity tensor was calculated which provides information on the direction and magnitude of the major and minor component of permeability. The models must be calibrated, which is usually carried out by varying relevant input parameters until laboratory or in-situ conditions are achieved. However, hydraulic calibration was not possible and relevant input parameters could only be estimated based on (mechanical) apertures measured microscopically. One of the possibilities to overcome this problem is to determine the full permeability tensor on rock samples in the laboratory (e.g. Renard et al., 2001). Nevertheless, realistic permeability values in the order of 10^{-15} m^2 could be numerically calculated. The anisotropy of

the fracture pattern is also reflected in the hydraulic conductivity tensor. An anisotropy factor of 1.73 can be specified at a depth of 0.5 m from the drift contour. For depths of 0 m and 2 m no tensor ellipsoid could be specified since the simulated fracture connectivity is below the percolation threshold.

Hydraulic simulations are based on fluid flow through fractures simulated along the grain boundaries. Microstructural investigations have shown that intracrystalline cracks may also develop under higher stresses. Although these fractures are considerably less frequently observed, they could also play an important role in the connectivity of fractures and, thus, the fluid flow.

The hydraulic simulations by means of 3DEC are very time-consuming so that the model dimensions have to be reduced. Moreover, the determination of the hydraulic conductivity tensor requires several computational runs so that alternatives have to be considered in the future. An alternative approach could be a geometrical percolation model where the connectivity and hence the permeability can be assessed from the fracture density.

5 Investigations on a Liquid Silica Improved Fracture System

In order to meet the requirement of the sealing function of a technical barrier, injection of liquid silica is generally considered as a sealing technique of microfractures. In the first phase of the project, on-site experiments were conducted in order to verify the sealing injection technique by means of liquid silica. In-situ experimental injection tests of liquid silica were carried out in a small area of the EDZ in the mine Niedersachsen Riedel (K+S AG) from a depth of about 1087.5 m (-1041.5 NN). The liquid silica was mixed with the fluorescent dye Uranin to visualize the silicate in rock salt later. Once the work was completed and after a waiting period of three months, samples (drill cores) were taken from the injected host rock and thin sections were prepared to inspect the fracture system microscopically. The samples were evacuated in a desiccator and soaked with blue epoxy resin to intensify the visualization of microfractures. More information about the cores and the in-situ-experimental injection of sodium silicate solution can be found in the final report “Improvement of the EDZ in salt” (VerA I).

5.1 Microstructural Analysis

For the microscopic examination, the drill core OFP6 was selected. About 25 ml sodium silicate solution was injected over the surface. Fig. 60 shows the investigated core sample with the injected areas (cut parallel to the cylinder axis).

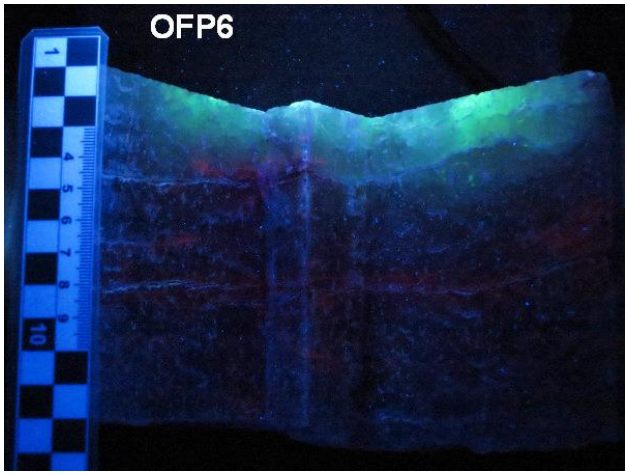

Fig. 60: Core OFP6 showing the fluorescing injected area.

In order to allow a three dimensional characterization of the fracture system, three thin sections (100 x 70 mm) were cut perpendicular to each other (Fig. 61). These thin sections were prepared around the injection hole and, therefore, include areas with sodium silicate solution. Thin section x6 was cut parallel to the cylinder surface, whereas z6 and y6 were orientated along the cyclindrical axis. To allow a comparison with the original host rock, an additional thin section (x6b) was prepared outside the injected area at the bottom of the core.

Microscopic analysis of thin sections was performed using a 1 cm² raster applied on the thin section, which is essential for evaluation. The investigations were performed with a fluorescence microscope (Fa. Leitz). Pictures were taken both in transmitted light and in UV light.

The analysis contains a significant photo documentation that visualizes the chemical gelation process with regard to the injection pressure and the topology of the fracture system. The knowledge gained from these microscopic analyses has therefore been summarized below and is based on typical observations.

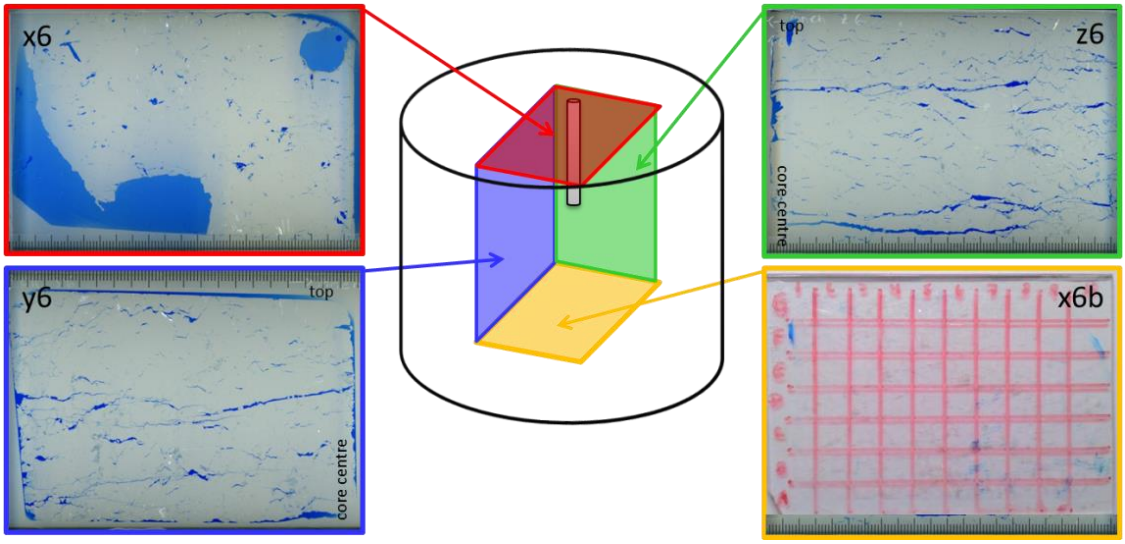

Fig. 61: Orientation of the thin sections.

Pictures that were taken under UV light show fluorescent regions (Fig. 62). The intensely bright green areas result from Uranin which was added into the sodium silicate solution. The Uranin molecules are incorporated partially in the silicate structure during gelation. Furthermore, single fluorescing particles can also be found in the epoxy compound. These particles were probably separated from sodium chloride during the soaking with the epoxy resin. It is not excluded that the blue colored epoxy resin derived light green reflections. During preparation, the epoxy may have transported uranin-bearing dust upon impregnation of the core.

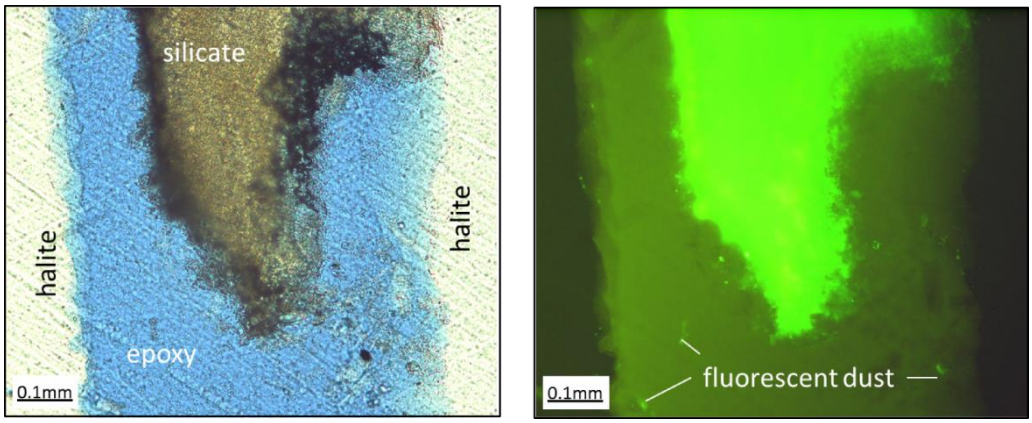

Fig. 62: Under UV light, the silicate fluoresces distinctly with a bright green color (right). In transmitted light (left), it appears brownish. The blue colored epoxy resin appears dark-green. Partly, small light green particles are seen in the epoxy compound.

When sodium silicate comes in contact with rock salt, the chemical gelation of the injection grout starts. At first, this takes place at the edge of the crack. As soon as the local injection pressure decreases in a single crack and nothing more can be inserted, the gelation process starts in the entire crack. Fig. 63 shows a crack system filled with silicate along several grains. Especially under UV light the penetrated silicate is clearly evident. The subsequently injected epoxy cannot penetrate completetly into theses fractures due to sealed flow channels. However, there is some uncertainity when evaluating the preferred flow paths of both silicate and epoxy. Flow paths within a three dimensional fracture system cannot be detected adequately with two dimensional thin sections. However, cracks are naturally different in size and shape. Very narrow areas can lead to bottlenecks when injecting the sodium silicate solution. Due to the small cross section, a faster gelation process can be observed in such areas. If there is an insufficient local injection pressure, no further sodium silicate can be injected through these bottlenecks. As a consequence, only a smaller part of the crack system can be covered. The process-related low injection pressures support such development.

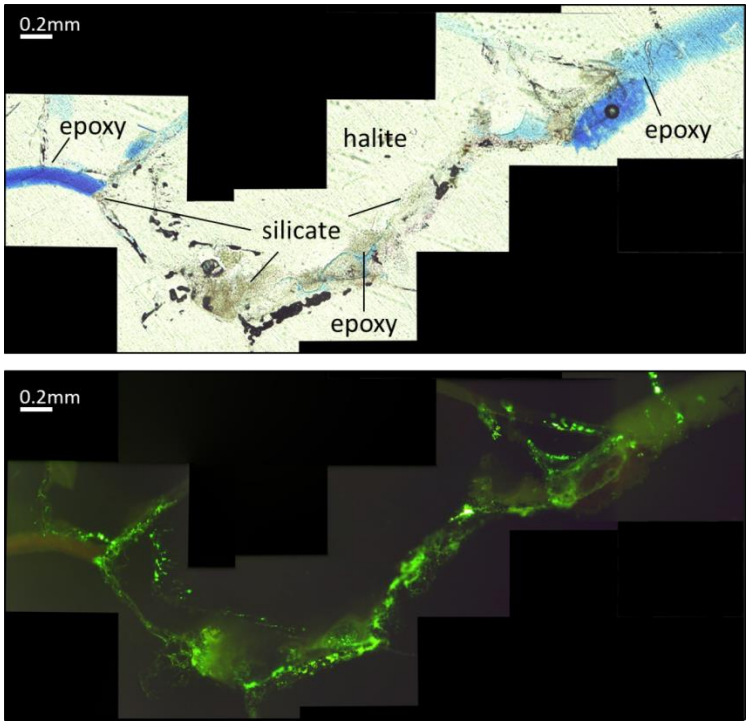

Fig. 63: Thin-section X6; raster E1. With silicate filled crack system through several grains and along the grain boundaries. Top: transmitted ligth; right: UV light.

The penetration behavior of liquid sodium silicate into intragranular cracks or along grain boundaries is shown exemplarily in Fig. 64 and Fig. 65. The crack aperture is less than 10 mircrons, which indicates that the liquid sodium silicate is able to penetrate into smallest fissures.

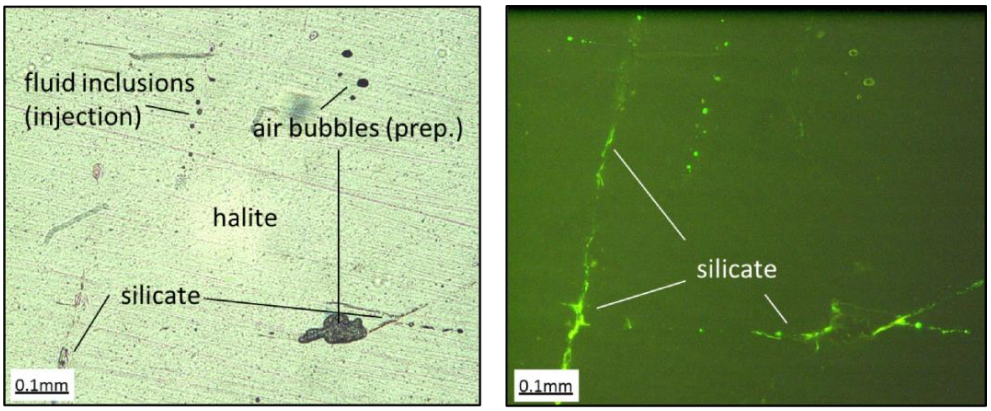

Fig. 64: **Detailed view from Fig. 11. In transmitted light, the silicate is barely visible (left). Under UV light, the fluoresced silicate is visible within the filled crack system. Left: transmitted ligth; right. UV light (prep.: resulting by preparation).**

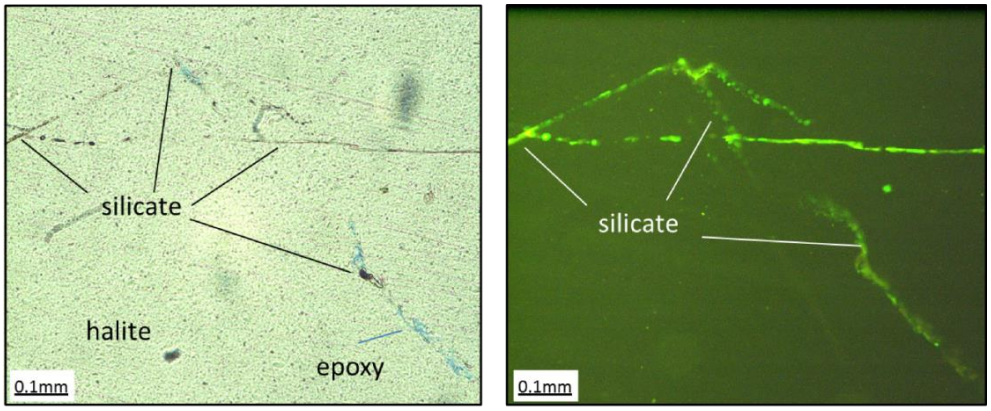

Fig. 65: **Detailed view from Fig. 11. In transmitted light, the silicate is barely visible (left). Under UV light, the fluoresced silicate is visible within the filled crack system. Left: transmitted ligth; right. UV light (prep.: resulting by preparation.**

Fig. 66 and Fig. 67 show exemplarily the silicate fixed in cleavage planes in halite and anhydrite. It has therefore the capability to penetrate into smallest fissures.

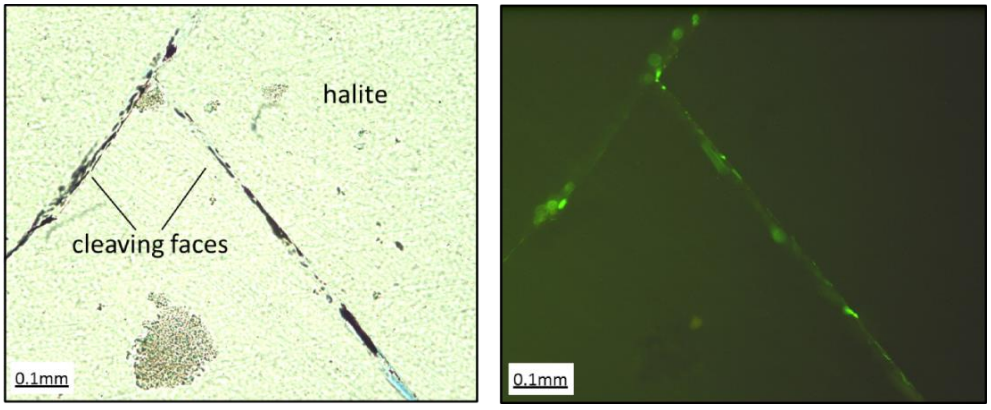

Fig. 66: **Detailed view from Fig. XX. Cleaving face filled with silicate. Left: transmitted light; right: UV light.**

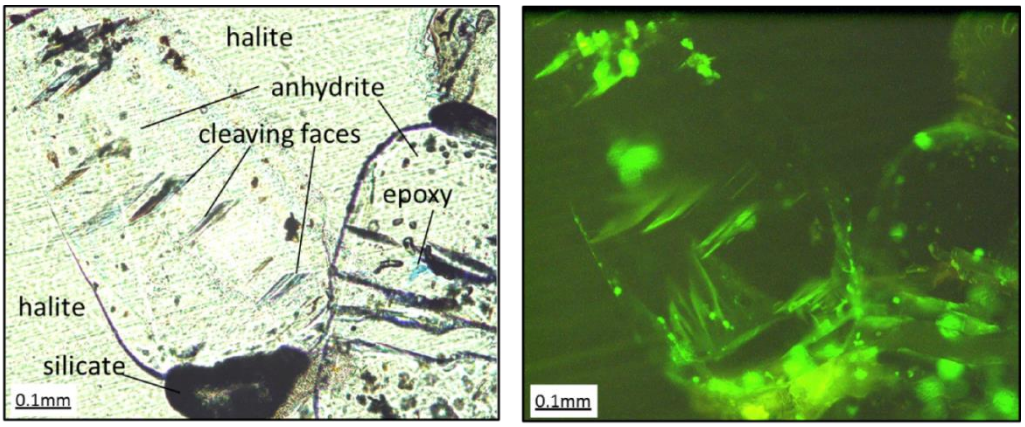

Fig. 67: **Thin section 6; raster D10. Anhydrite crystals with silicate. Left: transmitted ligth; right: UV light.**

Apart from the incorporation of Uranin in the silicate structure during gelation, it is also likely that Uranin molecules are incorporated in the reaction solution. The reaction solution may continue to migrate into the rock salt, which can be seen by fluorescent traces in the form of fluid inclusions (Fig. 68). Partial "necking down" effects are recognizable. The gaseous inclusions are not visible under the UV light. The fluid inclusions can be regarded as a remnant of the reaction solution. Hydrocarbon fluid inclusions can be excluded since these inclusions can only be found in the vicinity of the silicate.

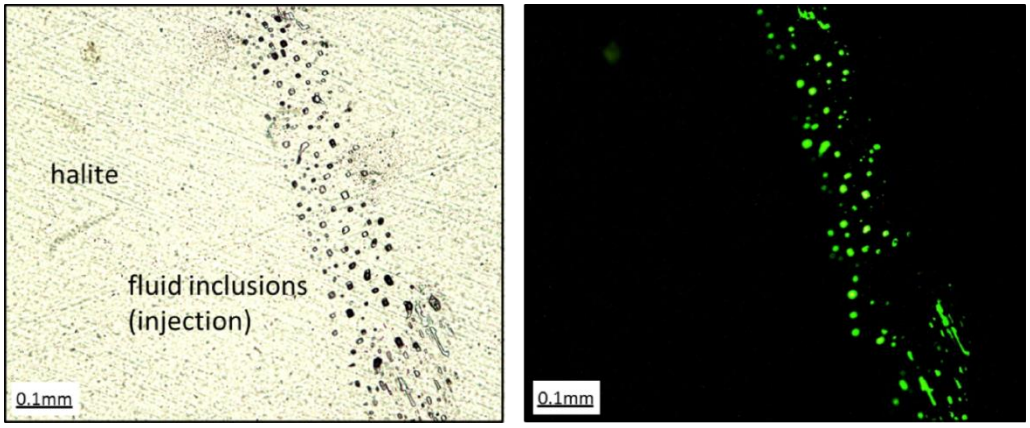

Fig. 68: **Thin-section X6; raster A9. Fluorescent fluid inclusions. Inclusions that contain only gas are not visible unter UV light. In the lower right, "necking down" effects can be seen. Left: transmitted light; right: UV light.**

Fig. 69 shows a crack tip sealed with silicate, which in transmitted light shows as a brownish mass. Starting from the crack tip, fluorescent traces in the form of fluid inclusions can be considered as a remnant of the reaction solution that became trapped within the crystal structure.

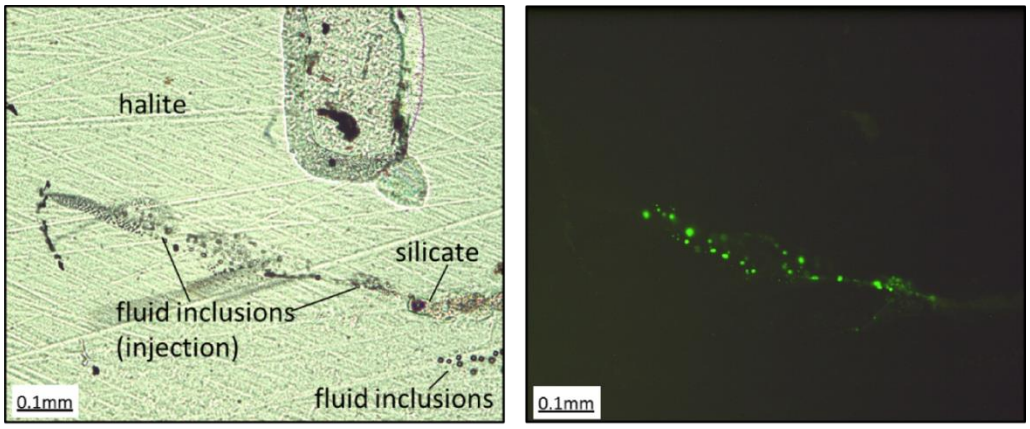

Fig. 69: **Thin-section X6; raster C4. Fluorescent fluid inclusions next to silicate. Left: transmitted light; right: UV light.**

5.2 Discussion

The thin sections of the injected rock salt drill core that were examined give information regarding the penetration behavior of the sodium silicate during an injection for the very first time. In contrast to injection techniques generally used in rock salt, the injection performed in this project was realized using a surface packer that offers only a small injection pressure. For this reason, only a small amount of sodium silicate could be injected. Nevertheless, scientifically valuable and important insights and previously unknown phenomena can be described. It was not clear where the reaction solution remains after the injection of sodium silicate. The present study shows that the reaction solution may continue to migrate into the rock salt and become trapped within the crystal structure in the form of fluid inclusions. Furthermore, it could be shown that sodium silicate solution can penetrate into crack systems with widths of less than 10 microns and seal them.

6 Long-Term Stability of Liquid Silica Improved Rock Salt

Sodium silicate solutions (water-glass; liquid glass) are chemical systems that contain water, anions of silicic acid, and Na_2O. Common properties of the solutions are low viscosities and a high alkaline milieu. A decrease of the pH value, a loss of water and/or an increase of electrolytes (salt) induce an initial gelation and a subsequent hardening of silicate solution. During this process, a network of colloidal particles is formed. The solid reaction product is amorphous silica. Since 1925 sodium silicate solutions have been used as chemical grout in civil engineering to stabilize and seal rocks and soils. Lohmann (1930) describes a successful application of sodium silicate solutions in the course of a dam construction in a potash mine. The reactions with soluble salts make the use of sodium silicate solution suitable for the grouting of evaporate rocks. Essential for an evaluation of the long-term stability of the amorphous silica is sufficient knowledge about the chemical and mineralogical interactions with the rocks and brines.

During the first phase of the project, a laboratory research program was conducted that considered injection of rock salt with sodium silicate solution (Bollingerfehr et al., 2011). The influence of the contact with NaCl and $MgCl_2$ solutions on the mineral content and the composition of the solutions were investigated. It could be shown that the $MgCl_2$ content in saline solutions has a decisive influence on the Si-solubility of amorphous silica. The solubility of the amorphous silica is negligible in saline solutions with > 20 wt% $MgCl_2$ (lower than the solubility of quartz in aqueous solutions). Over time, stable MOC-318-phases are also formed in these solutions. Halite can be regarded as a stable phase, since the solutions used were saturated by halite. Furthermore, it was shown that crystalline structures evolve slowly from the amorphous silica. Laboratory experiments show a built-up of cristobalite structures. According to natural analogues quartz could be a final reaction product. Basic information about the composition of sodium silica solution and MOC/MOS-phases as well as the mechanisms during the contact of sodium silica solution with the saline environment was pointed out in the first phase of the project (Bollingerfehr et al., 2011).

The investigations are divided into three parts. The first part completes experiments regarding the long-term stability of amorphous silica that have been started in the first phase of the project. The solubility of amorphous silica in saturated NaCl-solutions with low contents of $MgCl_2$ (4 and 10 wt% $MgCl_2$) is to be determined. The investigations have been supplemented by an experiment for temperature dependence of amorphous silica in contact with saline solution with > 20 wt% $MgCl_2$ at 35 °C. The second part deals with the formation of silicate-colloids when amorphous silica comes in contact with saline solutions. For this purpose, first index tests were conducted. In the third part it is tested whether amorphous silica is able to act additionally as a chemical barrier. Index tests were performed to check the reaction behavior of selected trace elements in contact with amorphous silica in a saline environment.

6.1 Investigations about the Resistance of Amorphous Silica in Saline Solutions

The experiments are used to complete the database for solubility of amorphous silica in saline solutions. They are a prerequisite for assessing the long-term stability of injected sodium

silicate solutions in rock salt. However, it should be noted that the chemical stability in the laboratory may differ fundamentally from that occurring in situ due to different physical and chemical conditions. Furthermore, the preparation can have a significant impact on the chemical reactivity. The amorphous silica used for the experiments was mechanically highly stressed during preparation and exposed to various environmental conditions. It was first dried and milled and then added to saline solutions. Then, it was removed from the saline solutions and washed with alcohol. In this case, the amorphous silica dehydrated. Thus, a direct comparison of the long term stability between laboratory and in-situ conditions is only possible to a limited extent.

In order to ensure a comparison with investigations already carried out during the first phase of the project, the amorphous silica came from the same production batch, and the experimental solutions used contained similar amounts of electrolytes. Halite grit was solidified with sodium silica solution (water-glas 37/40; δ= 1.36 g/cm³; pH= 11.4; Co. Carl Roth) in a plastic syringe. The samples were stored at room temperature for half a year. The plastic syringes were cut in order to remove the hardened halite grit / amorphous silica cylinders. The samples used for the following experiments were stored at room temperature in plastic boxes for 3.5 years. For the subsequent experiments, the surface areas of the samples were enhanced by crushing and milling. The initial material was dried at 32 °C after milling. with dry screening, the particle fractions < 450 µm, 450 to 2000 µm and > 2000 µm were separated. The particle fraction of 450 to 2000 µm was used for the experiments with salt solutions and colloid investigations (part one and two). The experiment of part three was carried out with the particle fraction < 450 µm. The remaining fraction was archived.

Table 3 shows the analyzed amorphous silica before saline solution addition. It is made up of 84 wt% NaCl and 8.2 wt% amorphous silica. The mass ratio of SiO_2/Na_2O amounts to 1.02. Dried Sodium silica solution analysed by XRF (X-ray fluorescence analysis) shows 78.2 wt% SiO_2 and 21.8 wt% Na_2O. The mass ratio of SiO_2/Na_2O amounts to 3.6.

Initial material	
compounds	wt%
Na_2O	7.9_6
MgO	0.0_7
Al_2O_3	0.0_2
SiO_2	8.1_5
SO_3	0.0_3
NaCl	83.76
total	100

Table 3: Composition of the initial material (halite/amorphous silica). Calculated without water. Analysed by XRF.

Three salt solutions of pure chemicals (Merck suprapur) were used for the experiments. Saturated NaCl-solutions with 4, 10 and 20 wt% $MgCl_2$ were prepared at room temperature (20-22 °C). Table 4 shows the composition of the saline solutions used.

Table 4: **Composition of the saline solutions. The numbers in brackets indicate the weight percent of $MgCl_2$ within the solution.**

	NaCl/$MgCl_2$(4)-solution	NaCl/$MgCl_2$(10)-solution	NaCl/$MgCl_2$(20)-solution
Ion [wt%]			
Na^+	8.41	5.88	1.96
K^+	0	0	0
Mg^{2+}	1.13	2.65	5.21
Cl^-	15.97	16.51	17.97
SO_4^{2-}	0	0	0
Calculated compound [g/L]			
NaCl	256	180	65
KCl	0	0	0
$MgCl_2$	53	125	249
pH	6.17	6.10	6.21

A total of three tests were carried out (V4, V5, V6). Since the amorphous silica is identical to that used in the first part of the project, a consecutive numbering was chosen. The test series V1, V2 and V3 are described in Bollingerfehr et al. (2011). The labelling of the test series and the allocation to the saline solutions are shown in Table 5. The amorphous silica was mixed with saline solution in a mass ratio of 1 to 5 and stored in air tight polyethylene bottles. The bottles were moved on a shaking platform daily for 1 minute. Test V6 was stored in a heating cabinet at 35 °C. At this temperature, the saturated solution was slightly undersaturated.

Table 5: **Description of the test series and sampling frequencies. The test series V1 to V3 were described in VerA I (Bollingerfehr et al. 2011). am. silica = amorphous silica.**

	Test series		
	V4	**V5**	**V6**
solid	halite/am. silica	halite/am. silica	halite/am. silica
solution	NaCl/$MgCl_2$-sol.	NaCl/$MgCl_2$-sol.	NaCl/$MgCl_2$-sol.
$MgCl_2$ in solution [wt%]	4	10	20
system	SiO_2-NaCl-$MgCl_2$-H_2O	SiO_2-NaCl-$MgCl_2$-H_2O	SiO_2-NaCl-$MgCl_2$-H_2O
temperature [°C]	23	23	35
initial weight solid [g]	50	50	50
initial weight solution [g]	250	250	250
sampling solution [days]	0,5/1/2/5/10/ 20/40/90	0,5/1/2/5/10/ 20/40/90	0,5/1/2/5/10/ 20/40/90
sampling solid [days]	1/10/90	1/10/90	1/10/90

For chemical analysis, the mixture of amorphous silica and saline solution must be separated into solid and liquid fractions. 4 ml of each mixture were centrifuged at a speed of 20000 rpm over a period of 30 min. The concentrations of the dissolved Si were determined by inductively coupled plasma mass-spectrometry (Elan 6000 ICP-MS; Co. Perkin Elmer). The concentrations of dissolved Na, K, Mg, Ca, Cl and SO_4 were analyzed by ion chromatography (IC; Co. Methrom). The pH values were measured with a calomel electrode.

The solid fractions obtained this way (4 to 6 g) were cleaned, washed with ethyl alcohol, filtered (45 µm), and dried at 35 °C. This procedure should prevent mineralogical changes of the solid fractions after sampling as far as possible (e.g. crystallization of halite due to evaporation). The solid fractions were investigated using X-ray diffraction analysis (XRD; X´Pert PW 3020; Co. PANalytical), backscattered electron imaging including semi-quantitative energy dispersive X-ray microanalysis (EDX; ESMA; SX100; Co. Cameca) as well as X-ray fluorescence analysis (XRF; Axios; Co. PANalytical). The oxygen contents were calculated on a stoichiometric basis prior to a scaling to 100 wt%. Table 6 shows the investigations carried out on the amorphous silicate and the saline solution and on the amorphous silicate/saline solution mixtures (test series V4, V5 and V6).

Table 6: **Compilation of the performed analysis of the initial components and as well of the test series V4, V5 and V6 according to time. [d]= days.**

	Initial components		Test series		
	solution	solid	**V4 [d]**	**V5 [d]**	**V6 [d]**
IC (Na,K,Mg,Cl,SO_4)	x		0,5/1/2/5/10/ 20/40/90	0,5/1/2/5/10/ 20/40/90	0,5/1/2/5/10/ 20/40/90
ICP-MS (Si)	x		0,5/1/2/5/10/ 20/40/90	0,5/1/2/5/10/ 20/40/90	0,5/1/2/5/10/ 20/40/90
pH	x		0,5/1/2/5/10/ 20/40/90	0,5/1/2/5/10/ 20/40/90	0,5/1/2/5/10/20 0/40/90
XRD		x	1/10/90	1/10/90	1/10/90
RFA		x			
ESMA		x	1/10/90	1/10/90	1/10/90

A backscattered electron image of amorphous silica before the saline solution was added and coated with carbon is shown Fig. 70.

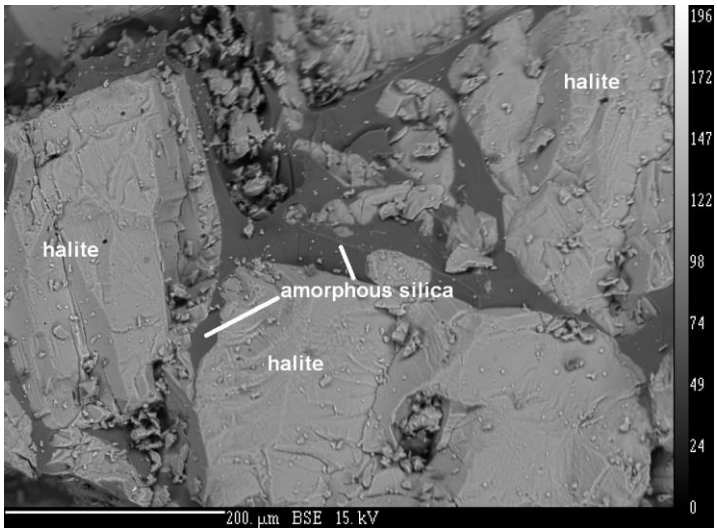

Fig. 70: Backscattered electron image (BSE) of the initial material showing halite and amorphous silica, which were formed by the reaction of sodium silicate solution with halite.

Analysis Carried out on the Solid Fractions

The solids are analyzed by XRD and ESMA. Since new phases are formed in the course of the experiment for which no references exist, an exact allocation of the registered signals is often not possible. The results of the initial material and the test series V4, V5 and V6 are given below.

The results of X-ray diffraction analysis (XRD) of extracted solid samples compared with the initial material are listed in Table 7. Halite is the dominant crystalline phase. The amorphous silica cannot be detected, because of it´s not existing crystallinity. An elevated background assigned an amorphous phase between 50 and 53 °2Θ . This background disappeared in test series V6 after 90 days. A strong signal at 28.56 °2Θ , according to a d-spacing of 3.124 Å, indicates the build-up of a mineral structure. The crystalline SiO_2-form cristobalite has such a lattice spacing, anhydrite also.

Magnesium oxichlorides (MOC) were detected as well. The MOC-518-phases in test series V6 occur on the day 1 and in test series V4 and V5 between the day 1 and day 10. The transfer from MOC-518 into MOC-318 occurs in V6 within the first day of the experiment. In test series V4 and V5, the transformation into MOC-318 did not occur during the experiment.

Table 7: **XRD-results of solids. h = halite; Crist? = possibly cristobalite; Am1 = amorphous area at 50-53 °2Θ, MOC-318: $Mg_2(OH)_3Cl$ x $4H_2O$; MOC-518: $Mg_3(OH)_5Cl$ x $4H_2O$; xx = dominant phases, x = mean phases; - = not detectable. V1, V2 and V3 are described in VerA I.**

Initial material	Test-series	days		
		1	10	90
	V4			
xx	h (31.722 °2Θ)	xx	xx	xx
-	MOC-518 (11.86 °2Θ)	-	x	x
x	Am1 (50-53 °2Θ)	x	x	x
x	(Crist?) (28.559 °2Θ)	x	x	x
	V5			
xx	h (31.722 °2Θ)	xx	xx	xx
-	MOC-518 (11.86 °2Θ)	-	x	x
x	Am1 (50-53 °2Θ)	x	x	x
x	(Crist?) (28.559 °2Θ)	x	x	x
	V6			
xx	h (31.722 °2Θ)	xx	xx	xx
-	MOC-518 (11.86 °2Θ)	x	-	-
-	MOC-318 (11.86 °2Θ)	x	x	x
x	Am1 (50-53 °2Θ)	x	x	-
x	(Crist?) (28.559 °2Θ)	x	x	x

The silicate reacts with the Mg from the solution. EDX analyses of the silicates prove that the release of Na^+ is coupled with a fixation of Mg^{2+}. To some extent, it was not possible to detect sodium in the silicate structures. This reaction appears very quickly, even in Na-solutions with small amounts of Mg (Table 8).

Table 8: **EDX semi-quantitative analysis of silicate from test-series V4 after 1 day reaction time.**

	Elements					Oxides [%]		
	O	Na	Mg	Si	Cl	Na_2O	MgO	SiO_2
wt%	51.3	0.62	6.84	40.88	0.36			
atom-%	64.38	0.54	5.65	29.23	0.2	0.83	11.35	87.46
wt%	51.77	3.31	0.44	44.18	0.3			
atom-%	64.99	2.89	0.36	31.59	0.17	4.46	0.73	94.51

Fig. 71 to Fig. 73 show BSE pictures from the solids. Newly formed halite crystals can be seen in all test series after 1 day of contact with the solutions. These crystals can be traced back to the contact with the saline solutions or result from the drying process. In test series V4 and V5 (SiO_2-NaCl-$MgCl_2$-H_2O-system with 4, respectively 10 wt% $MgCl_2$), the formation

of MOC-518-phases occurs between the first and the tenth day of the experiment (Table 7). The MOC-318-phases could also not be detected within the 90 days of the experiment.

In text series V6 (SiO_2-NaCl-$MgCl_2$-H_2O-system with 20 wt% $MgCl_2$ and 35 °C temperature, slightly undersaturated; Fig. 73, Table 7), needles of MOC-518- and MOC-318-phases are detected after 1 day of contact with solutions. This means that the formation of the MOC-518-phases took place directly after the experiment had started. The transformation into the stable MOC-318-phases started on the first day and ended during the first 10 days of the experiment.

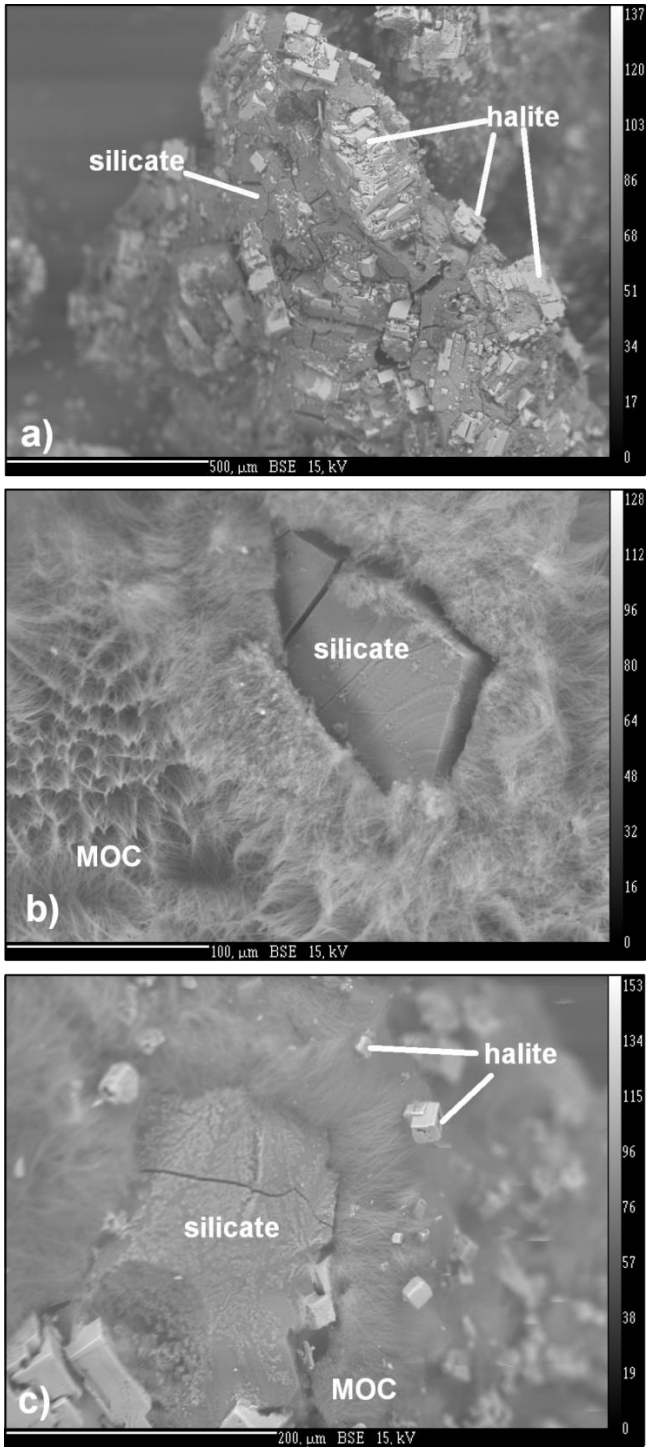

Fig. 71: BSE pictures from solid (halite/amorphous silica) of test series V4 (SiO_2-NaCl-$MgCl_2$-H_2O/OH^--system) with 4 wt% $MgCl_2$ after 1 (a), 10 (b) and 90 (c) days.

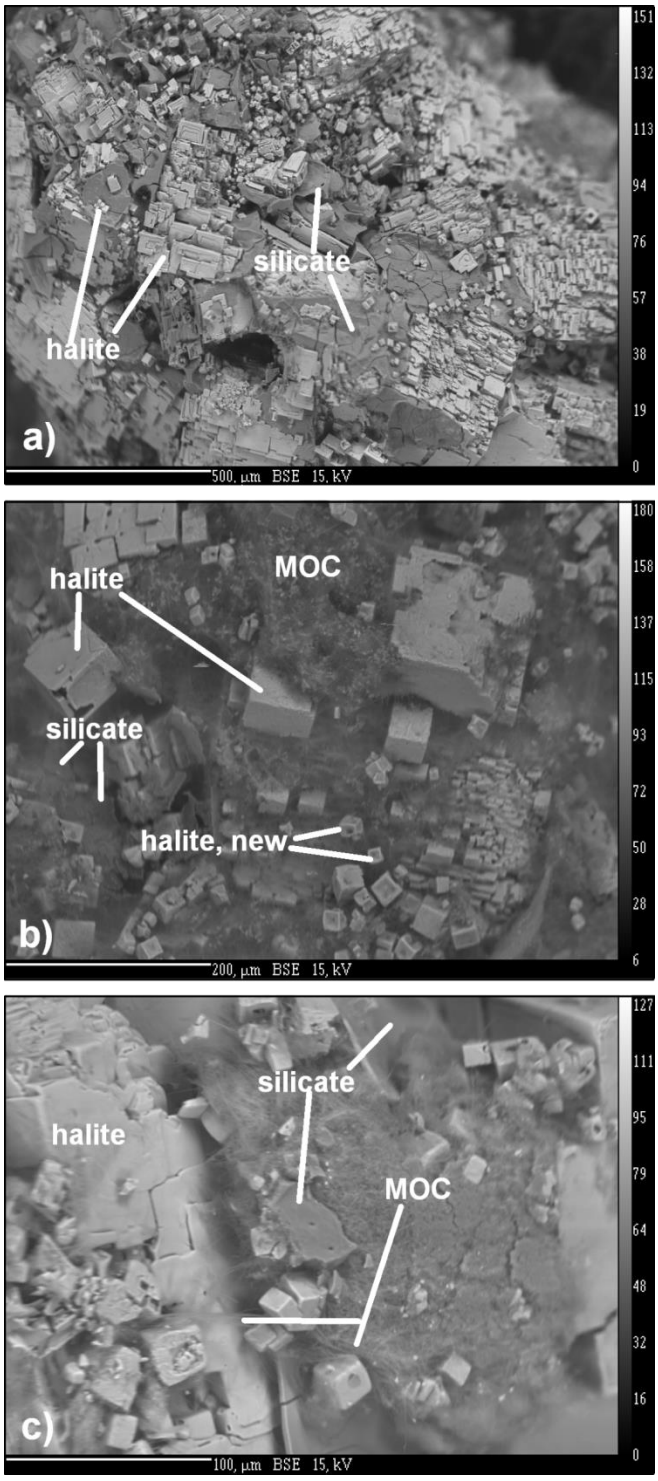

Fig. 72: BSE pictures from solid (halite/amorphous silica) of test series V4 (SiO_2-NaCl-$MgCl_2$-H_2O/OH^--system) with 10 wt% $MgCl_2$ after 1 (a), 10 (b) and 90 (c) days.

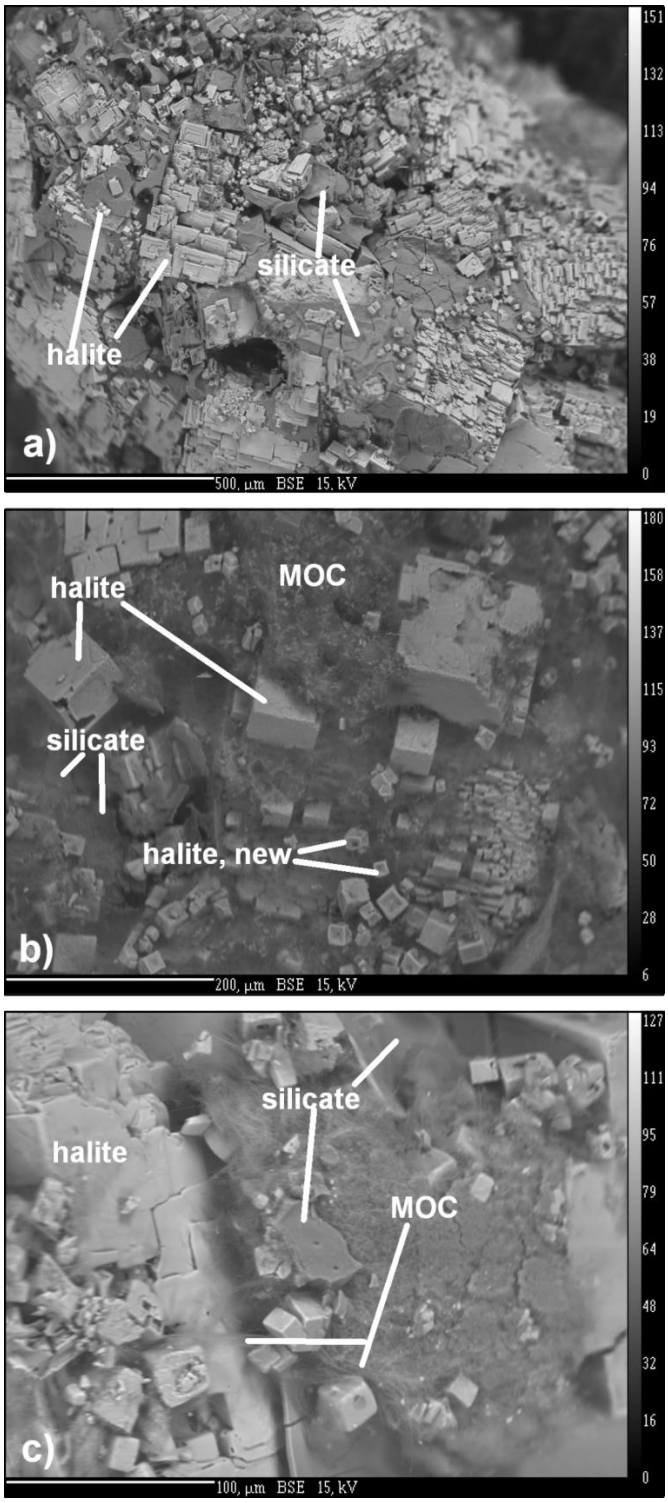

Fig. 73: BSE pictures from solid (halite/amorphous silica) from solutions of test series V4 (SiO_2-NaCl-$MgCl_2$-H_2O/OH^--system) with 20 wt% $MgCl_2$ and 35 °C after 1 (a), 10 (b) and 90 (c) days.

Analysis carried out on liquid fractions

In order to obtain data on the SiO_2 solubility, the solution analysis is of particular importance. The main components as well as the Si content were determined as a function of time. Table 9 shows the main components, the Si amounts and the pH values of the solutions during the experiment. The Si content in all solutions is below the detection limit with < 0.9 µg/g.

In test series V4 (saturated NaCl-solution with 4 wt% $MgCl_2$), the pH value increases within 12 hours from 6.2 up to pH 8.8 and decreases to pH 8.6 after 40 days. The Na content increases from initially 8.4 wt% up to 8.9 wt% while the Mg content decreases from 1.1 wt% to 0.9 wt%. In test series V5 (saturated NaCl-solution with 10 wt% $MgCl_2$), the pH increases within 12 hours from 6.1 up to pH 8.3 and decreases to pH 8.2 after 90 days. The Na content increases from initially 5.9 wt% to 6.4 wt% while the Mg content decreases from 2.7 wt% to 2.4 wt%. In test series V6 (slightly undersaturated NaCl-solution with 20 wt% $MgCl_2$ at 35 °C), the pH rises within 12 hours from 6.2 up to pH 7.2 and levels up to pH 7.3 during the duration of the experiment. The Na content increases from initially 1.96 wt% to 2.6 wt%, and the Mg content decreases slightly from 5.2 wt% to 5.08 wt%.

Table 9: **Composition and pH values of solutions of test series V4, V5 and V6. Dominant components in wt% and Si in µg/g. sampling V4-d1= Test series V4 - day 1.**

sampling	Na	Mg	Cl	pH	Si
V4 (4 wt% $MgCl_2$)	8.41	1.13	15.97	6.2	< 0.9
V4-d0,5	8.52	1.11	16.03	8.8	< 0.9
V4-d1	8.59	1.06	16.00	8.9	< 0.9
V4-d2	8.67	1.02	16.00	8.9	< 0.9
V4-d5	8.91	0.97	16.22	8.9	< 0.9
V4-d10	8.88	0.93	16.04	8.9	< 0.9
V4-d20	8.91	0.90	15.99	8.9	< 0.9
V4-d40	8.90	0.88	15.95	8.9	< 0.9
V4-d90	8.93	0.87	15.97	8.6	< 0.9
V5 (10 wt% $MgCl_2$)	5.88	2.65	16.51	6.1	< 0.9
V5-d0.5	5.97	2.62	16.53	8.3	< 0.9
V5-d1	6.03	2.57	16.49	8.4	< 0.9
V5-d2	6.13	2.53	16.50	8.4	< 0.9
V5-d5	6.22	2.47	16.45	8.3	< 0.9
V5-d10	6.30	2.44	16.45	8.4	< 0.9
V5-d20	6.37	2.38	16.40	8.4	< 0.9
V5-d40	6.35	2.40	16.40	8.4	< 0.9
V5-d90	6.38	2.38	16.43	8.2	< 0.9
V6 (20 wt% $MgCl_2$ 35 °C)	1.96	5.21	17.97	6.2	< 0.9
V6-d0.5	1.88	5.28	17.95	7.2	< 0.9
V6-d1	2.09	5.23	18.11	7.3	< 0.9
V6-d2	2.52	5.15	18.54	7.5	< 0.9
V6-d5	2.59	5.10	18.49	7.4	< 0.9
V6-d10	2.65	5.07	18.55	7.2	< 0.9
V6-d20	2.59	5.08	18.44	7.3	< 0.9
V6-d40	2.61	5.08	18.47	7.3	< 0.9
V6-d90	2.58	5.08	18.45	7.3	< 0.9

Results

The results of VerA I could be confirmed by the recent investigations. Fig. 74 shows the total dissolved SiO_2 contents of the salt solutions of VerA I and VerA II. Evaluated literature data of solubility tests from amorphous SiO_2 in salt solutions and the solubility of quartz in water are used for comparison. In VerA I, the solids had an age of 0.5 years. In pure NaCl-solutions the Si contents show an average value of 59.9 µg SiO_2/g (28 µg Si/g) after one day of contact /VerA I/. In the solution with 20.0 wt% $MgCl_2$ (T = 20 °C), Si reaches a maximum value of 8.6 µg SiO_2/g (4 µg Si/g), while in Q-solution the Si content lay below the detection limit of < 2.14 µg SiO_2/g (1 µg Si/g) /VerA I/. In all solutions of VerA II, the Si solubility of the 3.5-year-old solid lay below the detection limit of < 1.9 µg SiO_2/g (0.9 µg Si/g). (The different detection limits are a result of different analysis instruments).

All salt solutions containing $MgCl_2$ lay below the solubility line of amorphous Silica in $MgCl_2$-solutions from Marshall & Warakomski (1980). The results point to a function of age of the initial material. In this context, it would be interesting to carry out experiments with amorphous silica in pure NaCl solutions as a function of solid age.

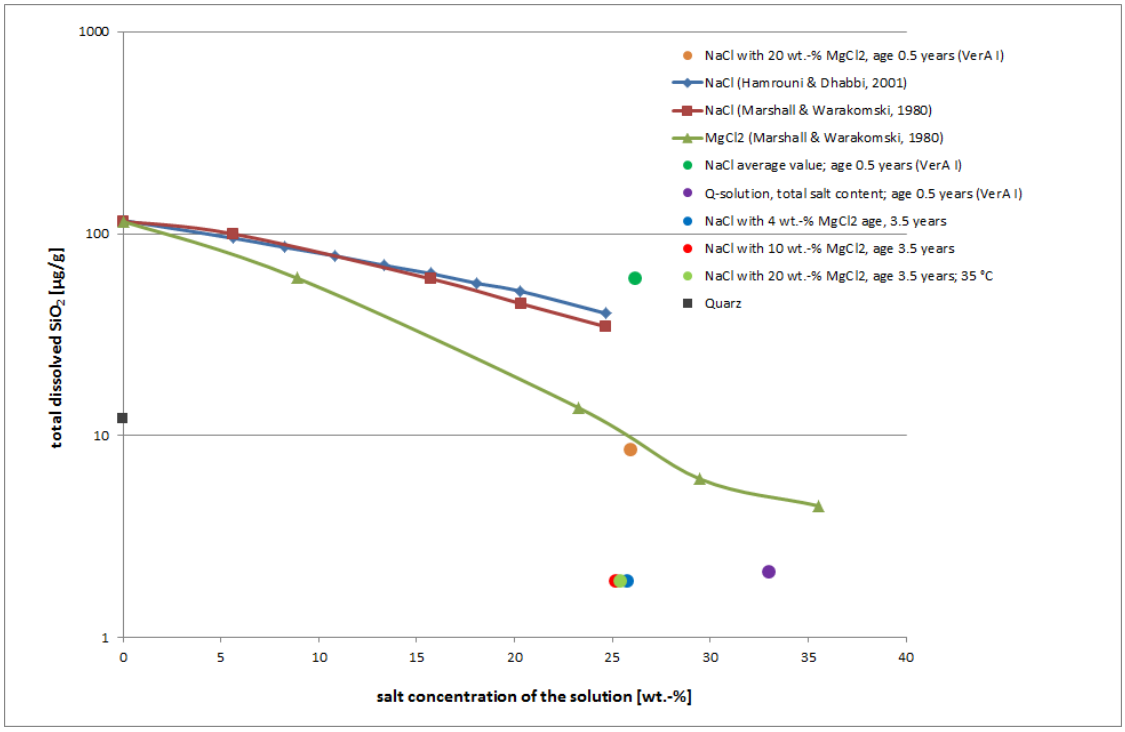

Fig. 74: **SiO_2-contents from tested solutions compared with the solubility of amorphous silica in different concentrations of pure saline solutions. The solubility for quartz at pH 6-7 is given for comparison.**

For the silicate phases, the XRD patterns of the solids in the NaCl-solutions with variable Mg-content are comparable. In the range 20-25 °2Θ, a background signal can be assigned to the amorphous or poorly crystallised MOC. Peaks document the formation of MOC-518, which transfers into the stable MOC-318. Geochemical calculations were made to prove the saturation states of the MOC-phases (Fig. 75). The values confirm the results of the mineralogical

investigations of Vera I and VerA II. Consequently, subsequent reaction of the MOC-318-phase to soluble compounds can be excluded, even over long periods of time.

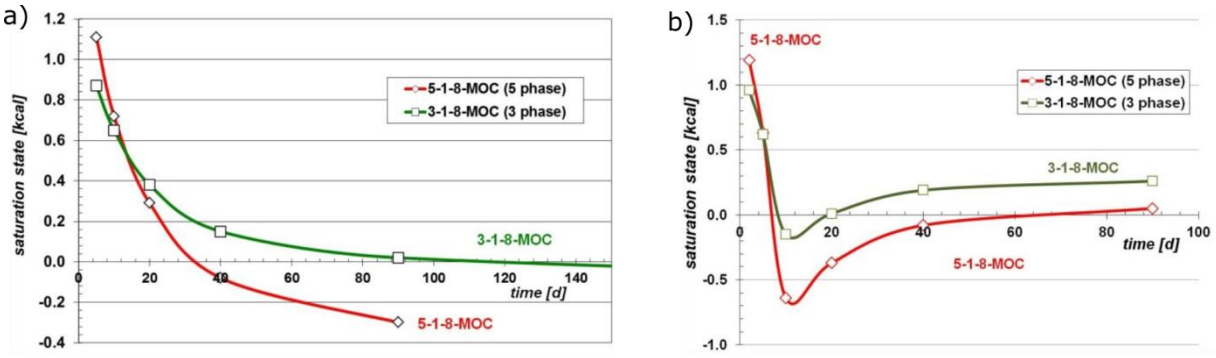

Fig. 75: **Calculated saturation state of the MOC-phases during the first 150 days of the experiment at room temperature (a) and during the experiment at 35 °C in test series V6 (b). Squares and diamonds indicate the calculated saturation state. The red and green lines represent equations adjusted to the calculated saturation states.**

6.2 Colloid Investigations

Sodium silicate solutions consist of sodium cations, hydroxide anions, monomeric and polymeric silicates, and species of colloidal size. In solutions with SiO_2:Na_2O ratios ranging from 2:1 to 4:1 about 75 % of the silica is present as extremely small particles which increase from 1 nm to 2 nm in diameter with increasing ratio (Iler 1982, Otterstad & Brandreth 1998). The condensation of polymerization of the silicates occurs in such a way that the number of Si-O-Si bonds will be maximized and the number of terminal hydroxyl groups will be minimized. Thus more complex and greater particles are formed. In the case, the contents of salts are insignificant, the particles grow in size with decrease in number. The reactions result in a formation of so-called silica sols. However, in the presence of salts three-dimensional gel networks of amorphous silicates arise.

Index tests were carried in order to obtain information on the influence of the solid-state reaction on the amount and size of the silicate species in the residual solution. The initial material of the particle fraction 450 to 2000 µm was used with an age of 3.5 years. The tests focused on pure NaCl solutions as a precipitation of dissolved Mg^{2+}- and Ca^{2+}-cations would influence the measurement results. In addition, NaCl solutions contain in comparison to magnesium salt solutions higher amounts of dissolved silicates. For the execution of the index tests solutions with 10.3 wt%, 5.2 wt%, 2.6 wt%, 1.3 wt% NaCl were prepared at room temperature. Due to the halite content of the solids (initial material) an increase of the NaCl content could be expected. In order to keep the particles in the solutions, the samples were not filtered or centrifuged after sampling. The analyzed solutions were clear and contained no visible suspended matter. The experimental procedure (solid/solution ratio, sampling procedures, et cetera) corresponds to the test series V4 to V6. However, the experiment lasted only 9 hours.

The total Si-content of the solutions was analyzed by ICP-MS and the content of monomeric silicates (e.g. $Si(OH)_4$) was determined by photometry after the formation of coloured molybdate complexes. So the difference between the analysis of photometry and ICP-MS could indicate higher polymerized silicic acid molecules, for example colloids.

Qualitative particle sizes or distributions are investigated by photon cross-correlation spectroscopy (also known as dynamic light scattering). Table 10 shows the pH-values of the initial solutions with different concentrations of NaCl and the after contact with the solid. The Si-values analysed with the different methods and the detected particle sizes are shown as well. The V1-experiments (VerA I) resulted in maximum Si values of about 170 µg/g (ICP-MS) at a pH value of almost 11. These values were determined 12 hours after starting the experiments and the solutions were filtered and centrifuged. Prior to the addition of the saturated NaCl solution, the mixtures of halite grit and water glass were stored for half a year at room temperature. The Si contents of the test solutions decreased in the course of the experiments to values between approx. 20 and 40 µg/g.

Table 10: pH-, Si-content and particle size in different concentrated NaCl-solutions after contact with halite/amorphous silica. The solutions were not filtered or centrifuged.

	NaCl-solution			
wt% NaCl	1.3	2.6	5.2	10.3
pH				
Initial solution	6.2	7.5	7.9	6.6
start	10.7	11.0	10.7	10.4
9h	10.8	11.1	10.8	10.4
Si [µg/g]				
ICP-MS	150	803	680	183
Photometry	34.7	32.5	46.2	40.0
Particle size[µm]	1.3 – 1.9	0.002 – 0.18	0.8 – 1.5	1.3 - 2

Table 10: pH value, Si content and particle size range in NaCl solutions after contact with halite/amorphous silica. The solutions were not filtered or centrifuged with the exception of the saturated NaCl solution (26.4 wt%. Index*: Results of the V1 (VerA I) measurement series. N.d.: not determined.

wt% NaCl	1.3	2.6	5.2	10.3	26.4*
pH value					
Initial solution	6.2	7.5	7.9	6.6	7.2
Start	10.7	11.0	10.7	10.4	10.7
After 9 hours	10.8	11.1	10.8	10.4	10.9 / 10.9
Si content [µg/g]					
Total amount (ICP-MS)	150	803	680	183	163 / 181
Monomeric silicate (Photometry)	34.7	32.5	46.2	40.0	N.d.
Particle size [µm]	1.3 – 1.9	0.002 – 0.18	0.8 – 1.5	1.3 - 2	N.d.

As to be expected, the pH-values of the initial solutions were in the neutral range. The contact with the silicate phases caused a significant increase of the pH-value. This is plausible because of the use of alkaline water glass, the release of hydroxide ions during the polymerization of silica and the low capacity of pure NaCl solution to stabilize the pH-value. Experiments with colored indicators showed comparable results.

In the case of two solutions (1.3 wt% and 10.3 wt% NaCl), the total Si content is comparable to the measurement results of the V1 (VerA I) test series. However, two measurements result in much higher Si values (2.6 wt% and 5.2 wt%). These values are incomprehensible and errors during the measurement cannot be ruled out. Conspicuous in all cases is that the amounts of Si analyzed by ICP-MS are higher than analyzed by photometry. Considering a total Si content of 170 µg/g, the proportion of monomeric silicates varies in a range of 19 % to 27 % with an average value of 23 %. According to the particle size measurements, the remaining Si contents are fixed in colloids, despite the large variations of the size values and the differences between the solutions. The calculated proportions are comparable to the values of Iler (1982). This result suggests that the ratio of the monomeric silica to the higher-molecular silica components changes only slightly in NaCl solutions, however, more investigations are necessary to confirm this finding.

6.3 Reaction Behavior of Selected Trace Elements in Contact with Silicate in a Saline Environment

It is a well-known that sodium silicate solutions and amorphous silicates reduce the concentration of many metal ions in low-saline waters (e.g. Fendorf et al. 1994, Fendorf & Sparks 1994, White et al. 1998). Moreover, natural analogue studies show a large binding capacity of silicates for heavy metals, such as uranium (e.g. Massey et al. 2014). There are several possible mechanisms that reduce the amount of dissolved metals. The mechanisms include the formation of insoluble metal silicates, physical adsorption of the metals onto silicate surfaces, and the encapsulation within silicate polymers. In addition, the polymerization of silicates causes a release of hydroxide ions. As a result of this reaction metals can be fixed in the structure of metal hydroxides. In the case chlorides or sulfate anions are present metal oxichlorides or oxisulfates can precipitate. An example is the reaction of dissolved Mg^{2+} ions. During the experiments the concentration of this metal decreases from initially 5.1 wt% (20 wt% $MgCl_2$) to 4.8 wt.% after 40 days. The processes of fixation were the formation of Mg-silicates and magnesium oxichlorides, which precipitate instead of magnesium hydroxide due to the high Mg-content of the residual solution.

The reactions of monomeric silicates with divalent and trivalent metal ions could be described by the following equations in a simplified manner, where M^{2+} and M^{3+} are used as an abbreviation of the metals:

$2\ M^{2+}\ Si(OH)_4 \Rightarrow M_2SiO_4 + 4\ H+$
$M^{3+} + Si(OH)_4 \Rightarrow MSiO(OH)_3^{2+} + H^+.$

By this way dissolved radionuclides, such as uranyl and neptunyl cations (cf. Dent et al. 1992, Michard et al. 1996), react with silicates, e.g.:

$UO_2^{2+} + Si(OH)_4 \rightarrow UO_2SiO(OH)_3^{+} + H^{+}$.

Final reaction products can be the minerals sodeyite ($(UO_2)_2(SiO_4) \cdot 2H_2O$) or in the presence of magnesium sklodowskite ($Mg(H_3O)_2(UO_2)_2(SiO_4)_2 \cdot 4H_2O$) (cf. Stohl & Smith 1981).

Generally, the interactions of the silanol group of polymeric silica with dissolved metals can be described as

$x(\equiv Si\text{-}OH) + M^{n+} \Rightarrow M(\equiv Si\text{-}O)_x^{(n-x)+} + xH^{+}$.

According to Porter & Weber (1971) the interaction with Fe^{3+} can be written formally as

$(\rightarrow SiOH)_m + Fe^{3+} \Rightarrow (\rightarrow SiOH)_{m-n}(\rightarrow SiO)_nFe^{(3-n)+} + nH^{+}$.

With the regard to the precipitation of hydroxides, it is necessary to consider that their solubility varies in a wide range and the equilibrium solubility of most metals is strongly pH dependent (Fig. 76). Generally, hydroxides of monovalent alkali metals are strong bases with a high solubility. Despite the fact that the values of divalent and trivalent metals are lower, large differences exist. For example, the solubility of Cu, Ni, Cd are somewhere in the region of milligram per liter, whereas the solubility of barium hydroxide shows a strong dependence on temperature and the solubility is about 56 gram per liter water at 20°C. Strontium hydroxide is more readily soluble in water than the hydroxides of calcium and magnesium.

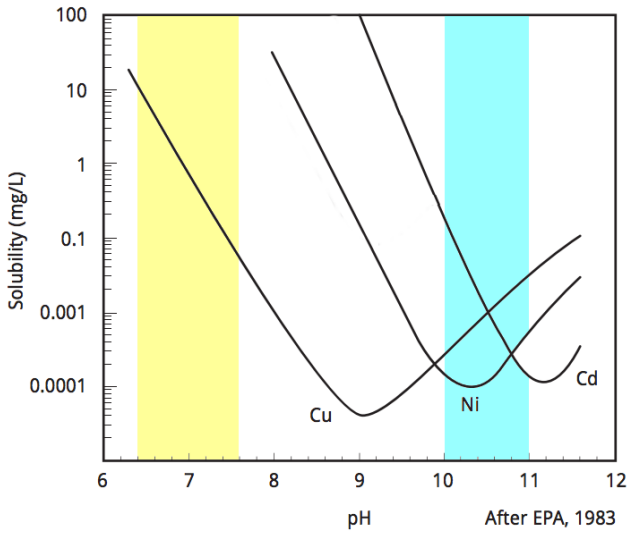

Fig. 76: **Solubility of copper (Cu), nickel (Ni), and cadmium (Cd) in water in dependance of the pH value (Patterson et al. 1983, Ayres et al. 1994). The yellow and the blue fields mark the expected pH range of the NaCl-$MgCl_2$-solution and the NaCl-solution, repsectively.**

The salt content of solutions influences the reactions of the silicate phases. A variety of heavy metal oxychlorides are well-known and described in the literature (e.g. Feitknecht & Ammann 1951, Feitknecht & Collet 1936, 1939, Feitknecht & Fischer 1935, Oswald & Feitknecht 1964). Consequently, metal oxychlorides and oxysulfates can precipitate in a high-saline environment instead of pure hydroxides. In addition, the pH-buffer-capacity of many salt solutions can influence the reaction mechanisms. For this reason, laboratory tests were carried out which proof the formation of solids during the mixing of water glass with barium (Ba), cobalt (Co), iron (Fe), nickel (Ni), and strontium (Sr) salt solutions. The visual observations are comparable to the well-known crystal, silicate or chemical garden experiments. Chemical gardens are obtained from the precipitation reaction on adding crystals of a soluble heavy metal salt to aqueous solutions of sodium or potassium silicate. They are a long-studied phenomenon and detailed information about their formation and composition are described for example by Cartwright (2011a,b) and Pagano et al. (2007).

Due to the positive results of the experiments, first key tests were carried out to obtain quantitative measurement values of the dissolved metal concentrations. Caesium was chosen as an example of a monovalent metal, however, caesium hydroxide, has a high solubility in water. In addition, the behavior of the divalent ions Cs^{+}, Ni^{2+}, Co^{2+}, Ba^{2+} and $[UO_2]^{2+}$ were investigated. Ni^{2+} and Co^{2+} can be viewed as a representative of a larger group of heavy metals that include Cu^{2+} and Cd^{2+} (cf. Fig. 76) or Fe^{2+} and Zn^{2+}. In addition, this selection considers a wide range of ionic radius. Two tests related to the reaction behavior of iodine. It is expected that the chloride minerals of barium, caesium, cobalt, nickel or strontium do not limit the final concentration, because of their high solubility in water.

The fraction < 450 µm of the milled initial material (salt grit/amorphous silica) was used. The experiments were conducted with pure saturated NaCl solution and saturated NaCl solution with 20.0 wt% $MgCl_2$. The initial material was diluted 1:5 with solution (50 g solid / 250 g solution) (Table 11).

Table 11: Compilation of experimental approaches to the retention tests and sampling period.

	unit	SV-1	SV-2	SV-4	SV-4
solid < 450 µm	g	50	50	-	-
Sodium silica solution 37/40	mL	-	-	10	10
NaCl-solution, pure	g	250	-	100	-
NaCl-solution (20 wt% $MgCl_2$)	g	-	250	-	100
Ni^{2+}	µg/g	10	10	-	-
Co^{2+}	µg/g	10	10	-	-
Sr^{2+}	µg/g	10	10	-	-
Ba^{2+}	µg/g	10	10	-	-
Cs^{+}	µg/g	2	2	-	-
$[UO_2]^{2+}$	µg/g	2	2	-	-
I^{-}	µg/g	-	-	10	10
sampling solutions	[d]	1/41/90	1/41/90	1/41/90	1/41/90

For the tests with iodine, a defined quantity of sodium silica solution (37/40) was filled into iodised solutions. To prevent oxidation to iodine I_2, solutions were reductively stabilized with 1 g of Na_2SO_3. The solutions with iodine were stored in glass jars in order to prevent the sorption of I^- to the vessel walls. The tests lasted 90 days. For analysis, the solutions were centrifuged for 30 min at 20000 rpm. The analysis was performed using inductively coupled plasma mass-spectrometry. Mineralogical investigations of the solids were not carried out.

The results of the test series SV-1 to SV-4 are listed in Table 12 and shown in Fig. 77. Table 13 shows the results of pH-measurements (V1- and V2-experiments) in comparison to the concentrations of the divalent heavy metals.

Table 12: **Concentration trends of the studied trace elements in different solutions in contact with silicate (samples: SV-1 and SV-2) and sodium silicate solution (samples: SV-3 and SV-4).**

	unit	blind	1	2	3
Time of contact	[d]	0	1	41	90
sample SV-1 in pure NaCl-solution					
Ni^{2+}	µg/g	9.9	0.4	0.0	0.0
Co^{2+}	µg/g	9.5	0.4	0.0	0.0
Sr^{2+}	µg/g	10.2	9.8	3.1	2.6
Ba^{2+}	µg/g	9.7	9.5	4.1	3.7
Cs^+	µg/g	1.7	1.7	1.6	1.6
$[UO_2]^{2+}$	µg/g	1.8	1.6	0.0	0.0
sample SV-2 in NaCl-solution (20 wt% $MgCl_2$)					
Ni^{2+}	µg/g	9.9	7.9	1.4	0.8
Co^{2+}	µg/g	9.9	8.8	1.1	0.3
Sr^{2+}	µg/g	10.1	10.1	10.1	10.2
Ba^{2+}	µg/g	9.4	9.4	8.5	8.5
Cs^+	µg/g	1.7	1.6	1.6	1.6
$[UO_2]^{2+}$	µg/g	1.9	1.8	1.2	0.9
sample SV-3 in pure NaCl-solution					
I^-	µg/g	10.3	10.2	10.0	10.1
sample SV-4 in NaCl-solution (20 wt% $MgCl_2$)					
I^-	µg/g	9.8	10.1	4.2	10.2

Table 13: **Results of the pH-value (V1-experiments) and concentrations of Ni2+, Co2+, Sr2+, Ba2+, and [UO2]2+ in the initial solutions and after contact with the silicates (samples: SV-1 and SV-2).**

Time of contact	pH-value (V1)	Ni^{2+}	Co^{2+}	Sr^{2+}	Ba^{2+}	$[UO_2]^{2+}$
	V1-experiments	Sample SV-1 in pure NaCl-solution				
0 d	7.19	9.9	9.5	10.2	9.7	1.8
1 d	11.0 / 11.0	0.4	0.4	9.8	9.5	1.6
41 d	10.9 / 10.8	0.0	0.0	3.1	4.1	0.0
90 d	10.8 / 10.8	0.0	0.0	2.6	3.7	0.0
	V2-experiment	Sample SV-2 in NaCl-solution (20 wt% $MgCl_2$)				
0 d	7.7	9.9	9.9	10.1	9.4	1.9
1 d	7.9	7.9	8.8	10.1	9.4	1.8
41 d	7.4	1.4	1.1	10.1	8.5	1.2
90 d	7.4	0.8	0.3	10.2	8.5	0.9

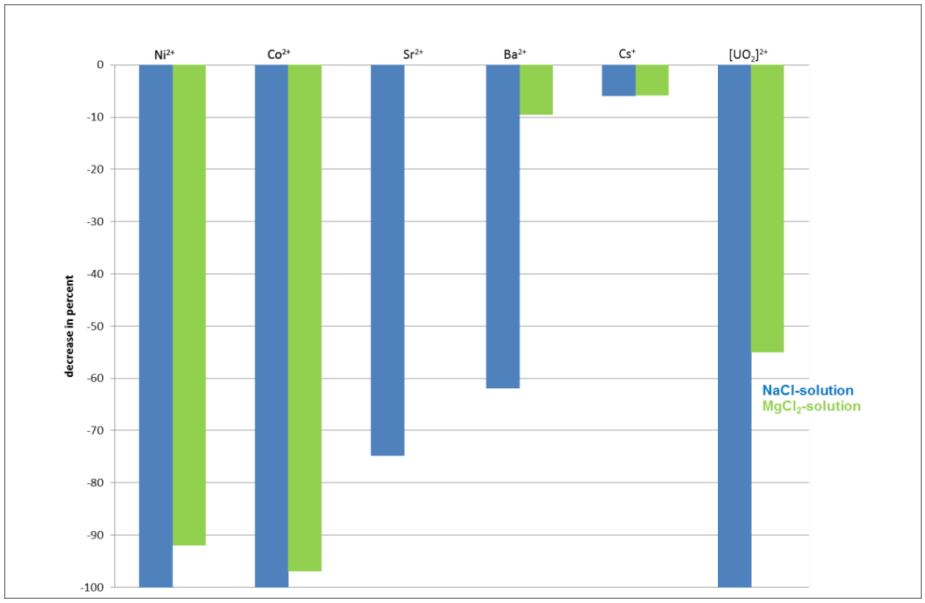

Fig. 77: **Percentage decrease in the dissolved ions due to the contact with amorphous silica.**

In both test solutions, the concentration of the Cs^+ decreases only slightly. The values of the Table 13 illustrate a rapid decrease of Ni^{2+} and Co^{2+} concentrations and contemporaneous a significant increase of the pH-value in the NaCl-solutions. In contrast, it is not possible to correlate the decrease of the Sr^{2+}, Ba^{2+}, and $[UO_2]^{2+}$-concentrations with the change of the pH-value. Finally, Co^{2+} and Ni^{2+} are completely removed, $[UO_2]^{2+}$ up to > 99 % and Ba^{2+} and Sr^{2+} to 60 % to 75.

In the NaCl-solution with 20 wt% $MgCl_2$, the largest decreases are of Co^{2+} and Ni^{2+} with > 90 %, followed by $[UO_2]^{2+}$ with > 50 %. The value for Ba^{2+} decreases only slightly, while for Sr^{2+} no decrease is seen.

With regard to the composition of the test solutions, it must be emphasized that the metals Ni^{2+}, Co^{2+}, Sr^{2+}, Ba^{2+} and the ion $[UO_2]^{2+}$ show in the pure NaCl solution a larger decrease of the concentration. This behavior could be a result of a higher pH value, resulting in a formation of hydroxide phases. Another effect, which might influence the metal concentration, is the higher ionic strength of the NaCl-$MgCl_2$-solution. Consequently, more salt ions are present that could be prevent the binding of heavy metal cations onto the mineral surfaces.

In summary, the experiments demonstrate that silicate solutions and amorphous silicates are able to fix many toxic or radioactive heavy metals, which are dissolved in NaCl- and NaCl-$MgCl_2$-solutions, in insoluble minerals. Due to this fact, it should be verified if injected sodium silicate solutions may act as a chemical barrier for toxic or radioactive heavy metals. However, a reaction of iodine was not recognizable. The deviations are probably due to oxidation processes. Also, no reactions between iodine and sodium silicate solution could be proven. This result points out that the binding capacity of the silicate phases and sodium silicate solutions is limited to positively charges metal cations.

6.4 Discussion

The studies carried out about the long-term behavior of amorphous silica lead to the conclusions that in saline environment, the silicate is insoluble in saturated brines. In the presence of Mg^{2+} stable MOC-phases are formed.

When evaluating the Si solubility of amorphous silica in pure NaCl-solutions, the occurrence of colloids should be pointed out, according to the colloid investigations. For more information, a detailed research program about SiO_2-colloids in salt solutions is still necessary.

First laboratory tests to verify the use (application) of silicate to act as a chemical barrier against repository-relevant elements supply promising results. In the course of the experiment, a decrease in the concentration of several elements is observed:

decrease (NaCl-solution): $Co^{2+} \sim Ni^{2+} > [UO_2]^{2+} >> Sr^{2+} \sim Ba^{2+} >> Cs^{+}$
decrease (NaCl-solution with 20 wt% $MgCl_2$): $Co^{2+} \sim Ni^{2+} >> [UO_2]^{2+} > Ba^{2+} > Sr^{2+} \sim Cs^{+}$

This means that amorphous silicate may act as a chemical barrier for specific elements in the saline environment.

7 Conclusion and Outlook

Discontinuum modeling methods have been used in this research and development project to investigate the fracturing and fluid flow in the EDZ of rock salt. Since the mechanical deterioration of rock salt occurs mainly through micro fractures, the mechanical and hydraulic behavior was investigated at grain scale where the fracturing can be explicitly investigated. For this purpose, the distinct element code 3DEC was used in combination with polyhedral shaped elements in order to simulate the shape and arrangement of grains.

To derive relevant input parameters used in the constitutive models and to validate the mechanical behavior of the models, a comprehensive geotechnical program was carried out. It includes uniaxial compression tests in combination with acoustic emission testing. The calibration of the parameters to simulate the mechanical behavior provides good results, and it was shown that cracking in the EDZ was simulated in a realistic manner. However, simple constitutive models were used for simulation that cannot simulate the interaction between intra- and intercrystalline deformation adequately. Thus, the fundamental processes of cracking can only be simulated with constitutive models adapted to the DEM approach. Furthermore, the calibration process is based on uniaxial compression tests, and the parameters derived provide satisfactory results for only relatively small external loads. While the mechanical parameters could be calibrated well, this is not possible for the hydraulic parameters due to data not available. Only a qualitative statement about the permeability values of the EDZ was given. Therefore, further research should focus on the development of new constitutive models and additional laboratory tests to give a thorough validation of the calculation results.

One disadvantage of the DEM method compared with continuum approaches is that the extent of the computational domain must be limited to make the problem computationally controllable. Currently, the DEM approach can only be used for near-field problems, and methods must be used to upscale the information gained. This seems to be the drawback of the current modeling approach used in this report. However, it is not always necessary to simulate the entire domain to be investigated by using discontinuum modeling methods. For many applications it is sufficient to obtain detailed information with regard to selected regions. The DEM is particularly useful in small-scale scenarios where the results can give a much greater understanding of the mechanical and hydraulic behavior. But it should also be considered that the DEM is one of the most rapidly developing areas of computational mechanics, and computer technology increases every year, improving the efficiency of the method.

It should be emphasized here that the use of the DEM model in combination with polyhedral elements is not only limited to rock salt simulation. The approach used in this project is also particularly suitable to simulate the damage behavior of granitic rocks.

Furthermore, new information regarding the behavior of sodium silicate when penetrating rock salt could be gained. The experiments showed that sodium silicate can close cracks with widths smaller than 10 μm. Furthermore, it could be demonstrated that the aqueous phase of sodium silicate is fixed in the salt in the form of fluid inclusions.

Concerning the long-term behavior of sodium silicate gel in a saliniferous environment it could be shown that the sodium silicate gel has a lower solubility in solution saturated with NaCl and containing Mg^{2+} ions than quartz has in water. Stable MOC-phases are formed, which was demonstrated for temperatures of up to 35°C. First tests showed that silica gel acts as a chemical barrier against specific elements relevant for repositories. The related mechanisms could not be investigated in this research program as this would require systematic testing.

The results of the thin sections investigations, of the investigations concerning the long-term behavior as well as of the initial tests concerning the behavior towards specific elements showed that sodium silicate is an injection agent suitable for rock salt. If and to what extent sodium silicate gel without addition of hardener can be used as injections agent, e.g. in clay rock, needs to be investigated.

8 References

Alkan, H., & Müller, W. (2008). *Numerical Modelling of Dilatancy Induced Percolative Permeation in Rock Salt.* Tech. rep., Institut für Sicherheitstechnologie (ISTec) GmbH.

Asahina, D., Houseworth, J., & Birkholzer, J. (2012). Thermalhydrological-mechanical model for fracture propagation, fluid flow, and transport in porous rock. *TOUGH Symposium 2012*, (S. 17-19).

Ayres, D., Davis, A., & Gietka, P. (1994). *Removing Heavy Metals from Wastewater - Engineering Research Center Report.* Tech. rep., University of Maryland.

Bandis, S., Lumsden, A., & Barton, N. (1983). Fundamentals of rock joint deformation. *International Journal of Rock Mechanics and Mining Sciences \& Geomechanics Abstracts, 20*(6), 249-268.

Barbe, F., Decker, L., Jeulin, D., & Cailletaud, G. (2001). Intergranular and intragranular behavior of polycrystalline aggregates. Part 1: FE model. *International journal of plasticity, 17*(4), 513-536.

Barton, N., Bandis, S., & Bakhtar, K. (1985). Strength, deformation and conductivity coupling of rock joints. *International Journal of Rock Mechanics and Mining Sciences & Geomechanics Abstracts, 22*(3), 121-140.

Bear, J. (1972). *Dynamics of fluids in porous media.* American Elsevier Publishing Company, Inc.

Bear, J., Tsang, C.-F., & De Marsily, G. (2012). *Flow and contaminant transport in fractured rock.* Academic Press.

Berkowitz, B. (1995). Analysis of fracture network connectivity using percolation theory. *Mathematical Geology, 27*(4), 467-483.

Blum, P., Mackay, R., Riley, M. S., & Knight, J. L. (2007). Hydraulische Modellierung und die Ermittlung des repräsentativen Elementarvolumens (REV) im Kluftgestein. *Grundwasser, 12*(1), 48-65.

Bollingerfehr, W., von Borstel, L., Engelhardt, H.-J., Müller, C., & Schmidt, H. (2011). *Vergütung der Auflockerungszone im Salinar (VerA) - Abschlussbericht - FKZ 02E10649.* Tech. rep., DBE TECHNOLOGY GmbH.

Böschel, D., Janich, M., & Roggendorf, H. (2003). Size distribution of colloidal silica in sodium silicate solutions investigated by dynamic light scattering and viscosity measurements. *Journal of colloid and interface science, 267*(2), 360-368.

Bourcier, M., Dimanov, A., E., H., Raphanel, J., Bornert, M., & Desbois, G. (2012). Full field investigation of salt deformation at room temperature: Cooperation of crystal plasticity and grain sliding. In Bérest, Ghoreychi, Hadj-Hassen, & Tijani (Hrsg.), *Mechanical Behavior of Salt VII* (S. 37-43). Taylor & Francis.

Brahme, A., Alvi, M., Saylor, D., Fridy, J., & Rollett, A. (2006). 3D reconstruction of microstructure in a commercial purity aluminum. *Scripta Materialia, 55*(1), 75-80.

Brown, S. R. (1987). Fluid flow through rock joints: the effect of surface roughness. *Journal of Geophysical Research: Solid Earth (1978--2012), 92*(B2), 1337-1347.

Buerger, M. (1930). Translation-Gliding in Crystals of the NaCl Structural Type. *Journal Mineralogical Society of America*.

Cai, M., Kaiser, P., Tasaka, Y., Maejima, T., Morioka, H., & Minami, M. (2004). Generalized crack initiation and crack damage stress thresholds of brittle rock masses near

underground excavations. *Int. Journal of Rock Mechanics & Mining Science, 41*, 833-847.

Carter, N. L., & Heard, H. C. (1970). Temperature and rate dependent deformation of halite. *American Journal of Science, 269*(3), 193-249.

Cartwright, J. H., Escribano, B., & Sainz-Diaz, C. I. (2011). Chemical-garden formation, morphology, and composition. I. Effect of the nature of the cations. *Langmuir, 27*(7), 3286-3293.

Cartwright, J. H., Escribano, B., Sainz-Diaz, C. I., & Stodieck, L. S. (2011). Chemical-garden formation, morphology, and composition. II. Chemical gardens in microgravity. *Langmuir, 27*(7), 3294-3300.

Christianson, M., Board, M., & Rigby, D. (2006). UDEC simulation of triaxial testing of lithophysal tuff. In Koniet.P., S. Holtz, C. Breed, & U. Ozbay (Hrsg.), *Proceedings of the 41st US rock mechanics symposium.*

Cristescu, N., & Hunsche, U. (1998). *Time effects in Rock Mechanics.* Chichester: Wiley & Sons.

Darcy, H. (1856). *Les fontaines publiques de la ville de Dijon.*

Dent, A. J., Ramsay, J. D., & Swanton, S. W. (1992). An EXAFS study of uranyl ion in solution and sorbed onto silica and montmorillonite clay colloids. *Journal of colloid and interface science, 150*(1), 45-60.

Eberhardt, E., Stimpson, B., & Stead, D. (1999). Effects of grain size on the initiation and propagation thresholds of stress-induced brittle fractures. *Rock Mechanics and Rock Engineering, 32*(2), 81-99.

Feitknecht, W., & Ammann, R. (1951). Über das hochbasische Cadmiumhydroxychlorid VI. *Helvetica Chimica Acta, 34*(7), 2266-2268.

Feitknecht, W., & Collet, A. (1931). Über die Konstitution der festen basibasis Salze zweiwertiger Metalle. BasBasis Nickelhalogenide mit "Einfachschichtengitter". *Helvetica Chimica Acta, 19(1)*, 831-841.

Feitknecht, W., & Collet, A. (1939). Zur Chemie und Morphologie der basischen Salze zweiwertiger Metalle VII. Über basische Nickelchloride experimentell bearbeitet. *Helvetica Chimica Acta, 22*(1), 1428-1444.

Feitknecht, W., & Fischer, G. (1935). Zur Chemie und Morphologie der basichen Salze zweiwertiger Metalle. III. Über basische Kobaltchloride. *Helvetica Chimica Acta, 18(1)*, 555-569.

Fendorf, S. E., & Sparks, D. L. (1994). Mechanisms of chromium (III) sorption on silica. 2. Effect of reaction conditions. *Environmental science & technology, 28*(2), 290-297.

Fendorf, S. E., Lamble, G. M., Stapleton, M. G., Kelley, M. J., & Sparks, D. L. (1994). Mechanisms of chromium (III) sorption on silica. 1. Chromium (III) surface structure derived by extended x-ray absorption fine structure spectroscopy. *Environmental science\& technology, 28*(2), 284-289.

Frühwirt, T. (2013). *Einaxiale Druckversuche mit versuchsbegleitender Messung der akutischen Emissionen - Laborbericht.* unpublished.

Gebrande, H., & Kern, H. (1982). Elasticity and inelasticity - Elastizität und Inelastizität. In *SpringerMaterials - The Landolt-Börnstein Database.* Angenheister, G.

Griffith, A. A. (1921). The phenomena of rupture and flow in solids. *Philosophical transactions of the royal society of london. Series A, containing papers of a mathematical or physical character*, 163-198.

Haase, D. (2015). *Parameteridentifikation eines ein-axialen Druckversuchs in LS-DYNA.* unpublished.

Hakami, E., & Larsson, E. (1996). Aperture measurements and flow experiments on a single natural fracture. *International journal of rock mechanics and mining sciences & geomechanics abstracts, 33*(4), 395-404.

Hampel, A., Salzer, K., Günther, R.-M., Minkely, W., Pudewills, A., Leuger, B., et al. (2012). Joint projects on the comparision of constitutive models for the mechanical behavior or rock salt II: Overview of the models and results of 3-D benchmark calculationS. *Proceedings of the 7th conference on the mechanical behavior of salt, Paris, France, 16-19 April 2012.*

Hampel, A., Schulze, O., Heemann, U., Zetsche, F., Günther, R.-M., Salzer, K., et al. (2007). *BMBF-Verbundvorhaben: Die Modellierung des mechanischen Verhaltens von Steinsalz: Vergleich aktueller SStoffgesetz und Vorgehensweisen - Synthesebericht.* Tech. rep.

Harder, J. (1997). *Simulation lokaler Fließvorgänge in Polykristallen.* Ph.D. dissertation, TU Braunschweig.

Heilbronner, R., & Barrett, S. (2013). *Image analysis in earth sciences: microstructures and textures of earth materials* (Bd. 129). Springer Science & Business Media.

Herbst, M., Konietzky, H., & Walter, K. (2008). 3D microstructural modeling. In D. \. Hart (Hrsg.), *Proceedings of Continuum and Distinct Element Numerical Modeling in Geo-Engineering.* Minneapolis, MN, USA.

Hunsche, U., & Hampel, A. (1999). Rock salt—the mechanical properties of the host rock material for a radioactive waste repository. *Engineering geology, 52*(3), 271-291.

Iler, R. K. (1982). Colloidal components in solutions of sodium silicate. In *Soluble Silicates* (S. 95-114). ACS Symposium Series.

Itasca. (2005). *FLAC3D Manuals.*

Itasca. (2013). *3DEC - 3 Dimensional Distinct Element Code Users's Guide.*

Itasca. (2013). *3DEC 5.0 - Constitutive Models.*

Itasca. (2013). *3DEC 5.0 - Theory and Background.*

Jackson, C. P., Hoch, A. R., & Todman, S. (2000). Self-consistency of a heterogeneous continuum porous medium representation of a fractured medium. *Water Resources Research, 36*(1), 189-202.

Jing, L. (2003). A review of techniques, advances and outstanding issues in numerical modelling for rock mechanics and rock engineering. *International Journal of Rock Mechanics and Mining Sciences, 40*(3), 283-353.

Jing, L., & Stephansson, O. (2007). *Fundamentals of Discrete Element Methods for Rock Engineering: Theory and Applications: Theory and Applications* (Bd. 85). Elsevier.

Jobmann, M., & Billaux, D. (2010). Fractal model for permeability calculation from porosity and pore radius information and application to excavation damaged zones surrounding waste emplacement boreholes in opalinus clay. *International Journal of Rock Mechanics \& Mining Sciences, 47*, 583-589.

Junker, L. (2000). *Mikroprozesse der plastischen Verformung und des Bruchs von polykristallinem Molybdändisilizid.* Ph.D. dissertation, Universität Halle-Wittenberg.

Kanani, N. (2006). *Werkstoffkunde für Oberflächentechniker und Galvaniseure: 700 Fragen und Antworten; 66 Tabellen.* Hanser Verlag.

Karato, S.-I. (2008). *Deformation of eart materials: an introduction to the rhealogy of solid earth.* Cambridge University Press, New York.

Kazerani, T., & Zhao, J. (2010). Micromechanical parameters in bonded particle method for modelling of brittle material failure. *International journal for numerical and analytical methods in geomechanics, 34*(18), 1877-1895.

Kelly, A. A., & Knowles, K. M. (2012). *Crystallography and crystal defects.* John Wiley & Sons.

Kleber, W., Bautsch, H.-J., Bohm, J., & Klimm, D. (2010). *Einführung in die Kristallographie.*

Klimczak, C., Schultz, R. A., Parashar, R., & Reeves, D. M. (2010). Cubic law with aperture-length correlation: implications for network scale fluid flow. *Hydrogeology Journal, 18*(4), 851-862.

Knauth, M., Minkley, W., & others. (2014). Modeling of the Mechanical and Hydraulic Behavior of Salt Rocks on a Discontinuum-Mechanical Basis. *48th US Rock Mechanics/Geomechanics Symposium.*

Kockel, F., & Krull, P. (1995). *Untersuchung und Bewertung von Salzformationen. Endlagerung stark wärmeentwickelnder radioaktiver Abfälle in tiefen geologischen Formationen Deutschlands.* Technischer Bericht, BGR, Hannover.

Krone, J., Buhmann, D., Mönig, J., Wolf, J., Heusermann, S., Keller, S., et al. (2008). *Überprüfung und Bewertung des Instrumentariums für eine sicherheitliche Bewertung von Endlagern für HAW – ISIBEL.* Gemeinsamer Abschlussbericht FKZ 02E10065 und 10055, DBE TECHNOLOGY GmbH, BGR, GRS, Peine, Hannover, Braunschweig.

Kulatilake, P., & Panda, B. B. (2000). Effect of block size and joint geometry on jointed rock hydraulics and REV. *Journal of engineering mechanics, 126*(8), 850-858.

Lan, H., Martin, C. D., & Hu, B. (2010). Effect of heterogeneity of brittle rock on micromechanical extensile behavior during compression loading. *Journal of Geophysical Research: Solid Earth (1978--2012), 115*(B1).

Liakopoulos, A. (1965). Darcy's coefficient of permeability as symmetric tensor of second rank. *Hydrological Sciences Journal, 10*(3), 41-48.

Lisjak, A., & Grasselli, G. (2014). A review of discrete modeling techniques for fracturing processes in discontinuous rock masses. *Journal of Rock Mechanics and Geotechnical Engineering*.

Lisjak, A., Garitte, B., Grasselli, G., Müller, H., & Vietor, T. (2015). The excavation of a circular tunnel in a bedded argillaceous rock (Opalinus Clay): Short-term rock mass response and FDEM numerical analysis. *Tunnelling and Underground Space Technology, 45*, 227-248.

Lisjak, A., Tatone, B. S., Grasselli, G., & Vietor, T. (2014). Numerical modelling of the anisotropic mechanical behaviour of opalinus clay at the laboratory-scale using fem/dem. *Rock mechanics and rock engineering, 47*(1), 187-206.

Lockner, D. (1993). The role of acoustic emission in the study of rock fracture. *International Journal of Rock Mechanics and Mining Sciences & Geomechanics, 30*(7), 883-899.

Lohmann, A. (1930). Die Anwendung des Chemischen Verfestigungsverfahrens bei der Abdichtung eines Laugendammes und bei Schachtdichtungsarbeiten auf dem Kaliwerk Sachsen-Weimar in Unterbreizbach (Röhn). *Kali und verwendete Salze, 24*, 81-85.

Long, J., & Witherspoon, P. A. (1985). The relationship of the degree of interconnection to permeability in fracture networks. *Journal of Geophysical Research: Solid Earth (1978--2012), 90*(B4), 3087-3098.

Long, J., Remer, J., Wilson, C., & Witherspoon, P. (1982). Porous media equivalents for networks of discontinuous fractures. *Water Resources Research, 18*(3), 645-658.

Manthei, G. (2004). CHARACTERIZATION OF ACOUSTIC EMISSION SOURCES IN A ROCK SALT SPECIMEN UNDER TRIAXIAL LOAD. *Journal of Acoustic Emission, 22*, 173-189.

Marshall, W. L., & Warakomski, J. M. (1980). Amorphous silica solubilities—II. Effect of aqueous salt solutions at 25 C. *Geochimica et Cosmochimica Acta, 44*(7), 915-924.

Massey, M. S., Lezama-Pacheco, J. S., Nelson, J. M., Fendorf, S., & Maher, K. (2014). Uranium incorporation into amorphous silica. *Environmental science & technology, 48*(15), 8636-8644.

Michard, P., Guibal, E., Vincent, T., & Le Cloirec, P. (1996). Sorption and desorption of uranyl ions by silica gel: pH, particle size and porosity effects. *Microporous materials, 5*(5), 309-324.

Min, K.-B., Jing, L., & Stephansson, O. (2004). Determining the equivalent permeability tensor for fractured rock masses using a stochastic REV approach: method and application to the field data from Sellafield, UK. *Hydrogeology Journal, 12*(5), 497-510.

Mises, R. v. (1928). Mechanik der plastischen Formänderung von Kristallen. *ZAMM-Journal of Applied Mathematics and Mechanics/Zeitschrift für Angewandte Mathematik und Mechanik, 8*(3), 161-185.

Missal, C., Gährken, A., & Stahlmann, J. (2015). Numerical investigations on the ansiotropic damage of the EDZ of drift in rock salt. In L. Roberts, K. Mellegard, & F. Hansen (Hrsg.), *Mechanical Behaviour of Salt VIII, Proceedings of the 8th conference on the mechanical behavior of salt, Rapid City, USA, 26-28 Mayl 2015*, (S. 109-114).

Müller, C., Lerch, C., Otparlik, K., & Konietzky, H. (2012). Simulation of the mechanical deterioration of rock salt at grain scale. In P. G.-H. Bérest (Hrsg.), *Mechanical Behaviour of Salt VII, Proceedings of the 7th conference on the mechanical behavior of salt, Paris, France, 16-19 April 2012*, (S. 107-114).

Müller, H.-H., & Leiss, B. (2013). *Abschlussbericht zur Gefügeanalyse einer deformierten Halitprobe anhand von Dünnschliffen.* unpublished.

Müller-Hoeppe, N., & Schmidt, H. (2015). Construction engineering: Grouting measures in damaged rock salt. *Mechanical Behaviour of Salt VIII, Proceedings of the 8th conference on the mechanical behavior of salt, Rapid City, USA, 26-28 Mayl 2015.*

Müller-Hoeppe, N., Schmidt, H., & Polster, M. (2014). Construction engineering: concept to describe the peremability of the excavation damaged zone as a function of pressure. *Z. Dt. Ges. Geowiss., 165(1)*, 107-114.

Niemi, A., Kontio, K., Kuusela-Lahtinen, A., & Poteri, A. (2000). Hydraulic characterization and upscaling of fracture networks based on multiple-scale well test data. *Water resources research, 36*(12), 3481-3497.

Oda, M. (1985). Permeability tensor for discontinuous rock masses. *Geotechnique, 35*(4), 483-495.

Oda, M. (1986). An equivalent continuum model for coupled stress and fluid flow analysis in jointed rock masses. *Water resources research, 22*(13), 1845-1856.

Oswald, H., & Feitknecht, W. (1964). Über die Hydroxidhalogenide Me2 (OH) 3Cl,-Br,-J zweiwertiger Metalle (Me= Mg, Ni, Co, Cu, Fe, Mn). *Helvetica Chimica Acta, 47*(1), 272-289.

Otterstedt, J.-E., & Brandreth, D. A. (2013). *Small particles technology.* Springer Science \& Business Media.

Pagano, J. J., Thouvenel-Romans, S., & Steinbock, O. (2007). Compositional analysis of copper--silica precipitation tubes. *Physical Chemistry Chemical Physics, 9*(1), 110-116.

Panda, B. B., & Kulatilake, P. (1999). Relations between fracture tensor parameters and jointed rock hydraulics. *Journal of engineering mechanics, 125*(1), 51-59.

Patterson, J. W., Kodukula, P., Aratani, T., & others. (1983). Removal of metals in combined treatment systems. In *Removal of metals in combined treatment systems.* EPA.

Popp, T., Kern, H., & Schulze, O. (2001). Evolution of dilatancy and permeability in rock salt during hydrostatic compaction and triaxial deformation. *Journal of Geophysical Research, 106*(B3), 4061-4078.

Porter, R. A., & Weber, W. J. (1971). The interaction of silicic acid with iron (III) and uranyl ions in dilute aqueous solution. *Journal of Inorganic and Nuclear Chemistry, 33*(8), 2443-2449.

Pusch, G., Alkan, H., & Cinar, Y. (2002). *Mechanische und hydraulische Eigenschaften von Auflockerungszonen des Gebirges in Verbindung mit der Planung von Verschlussbauwerken im Salinar.* Tech. rep., Institut für Erdöl- und Erdgastechnik TU Clausthal.

Quey, R., Dawson, P., & Barbe, F. (2011). Large-scale 3D random polycrystals for the finite element method: Generation, meshing and remeshing. *Comput. Methods Appl. Mech. Engrg. 200, 200*, 1729-1745.

Renard, P., & De Marsily, G. (1997). Calculating equivalent permeability: a review. *Advances in Water Resources, 20*(5), 253-278.

Renard, P., Genty, A., & Stauffer, F. (2001). Laboratory determination of the full permeability tensor. *J. Geophys. Res, 106*(811), 26443-26452.

Robinson, P. (1983). Connectivity of fracture systems-a percolation theory approach. *Journal of Physics A: Mathematical and General, 16*(3), 605.

Rollett, A. D., Lee, S.-B., Campman, R., & Rohrer, G. (2007). Three-dimensional characterization of microstructure by electron back-scatter diffraction. *Annu. Rev. Mater. Res., 37*, 627-658.

Rösler, J., Harders, H., & B{\"a}ker, M. (2008). *Mechanisches Verhalten der Werkstoffe.* Springer-Verlag.

Rycroft, C. (2009). Voro++: A three-dimensional Voronoi cell library in C++. *Lawrence Berkeley National Laboratory*.

Salzer, K., Günther, R.-M., Minkely, W., Popp, T., Wiedemann, M., Hampel, A., et al. (2012). Joint projects on the comparision of constitutive models for the mechanical behavior or rock salt I: Overview of the projects, reference mine for 3-D benchmark calculations, in-situ measurments and laboratory tests. *Proceedings of the 7th conference on the mechanical behavior of salt, Paris, France, 16-19 April 2012.*

Scheffzük, C. (1999). *Neutronographische Texturanalysen und Mikrostrukturuntersuchungen natürlicher und triaxial verformter Halite.* Ph.D. dissertation, Geoforschungszentrum.

Schulze, O., Popp, T., & Kern, H. (2001). Development of damage and permeability in deforming rock salt. *Engineering Geology, 61*(2), 163-180.

Senseny, P., Hansen, F., Russell, J., Carter, N., & Handin, J. (1992). Mechanical behaviour of rock salt: phenomenology and micromechanisms. *International journal of rock mechanics and mining sciences & geomechanics abstracts, 29*(4), 363-378.

Skrotzki, W., Frommeyer, O., & Haasen, P. (1981). Plasticity of polycrystalline ionic solids. *physica status solidi (a), 66*(1), 219-228.

SPE. (2015). Diagonalizing the permeability tensor. *Diagonalizing the permeability tensor*. http://petrowiki.org.

Stauffer, D., & Aharony, A. (1994). *Introduction to percolation theory.* CRC press.

Stoeckhert, F., Molenda, M., Brenne, S., & Alber, M. (2015). Fracture propagation in sandstone and slate--Laboratory experiments, acoustic emissions and fracture mechanics. *Journal of Rock Mechanics and Geotechnical Engineering*.

Stohl, F. V., & Smith, D. K. (1981). Crystal chemistry of the uranyl silicate minerals. *Am. Mineral., 66*.

Tammann, G., & Salge, W. (1927). Octahedral Glide of NaCl at High Temperature, Decrase in Yield Point with Rising Temperature. *Neues Jahrbuch für Mineralogie, 57*, 117.

Tsang, C.-F., Bernier, F., & Davies, C. (2005). Geohydromechanical processes in the Excavation Damaged Zone in crystalline rock, rock salt, and indurated and plastic clays-in the context of radioactive waste disposal. *International Journal of Rock Mechanics \& Mining Sciences, 42*, 109-125.

Uchic, M. D. (2011). Serial sectioning methods for generating 3D characterization data of grain-and precipitate-scale microstructures. In *Computational Methods for Microstructure-Property Relationships* (S. 31-52). Springer.

Wadell, H. (1935). Volume, Shape and Roundness of Quartz Particles. *Journal of Geology, 43 (3)*, 250-280.

Walter, K., Konietzky, H., & Bratskikh, A. (2010). *Bericht zum FuE-Vorhaben "Die Generierung von Mikrostrukturen in 3DEC auf Basis eine Voronoi-Gitters".* Tech. rep., TU Bergakademie Freiberg - Institut für Geotechnik.

Walter, K., Konietzky, H., & Herbst, M. (2009). „Three dimensional discrete element modelling to investigate damage and fracture development at the grain size level “. *Proc. 2nd Int. Conf. on Computational Methods in Tunneling, Bochum, Aedificatio Publishers.*

Wang, M., Kulatilake, P., Um, J., & Narvaiz, J. (2002). Estimation of REV size and three-dimensional hydraulic conductivity tensor for a fractured rock mass through a single well packer test and discrete fracture fluid flow modeling. *International Journal of Rock Mechanics and Mining Sciences, 39*(7), 887-904.

White, W. B., Scheetz, B. E., Silsbee, M., Gill, P., LaRosa-Tompson, J., & Reifsnyder, R. (1998). Interactions of aqueous metal silicates with mine water. *Proceedings of the International Conference on Tailings and Mine Waste, 5th*, (S. 589).

Wichert, J., Frühwirt, T., & H., K. (2014). Risk-assessment of the consolidation of a baroque tombstone of Cottaer sandstone. In H. Konietzky (Hrsg.), *43. Geomechanik-Kolloquium*, *2014-2.*

Wieczorek, K., & Schwarzianeck, P. (2004). *Untersuchung zur Auflockerungszone im Salinar (ALOHA2)- Untersuchungen zur hydraulisch wirksamen Auflockerungszone um Endlagerbereiche im Salinar in Abhängigkeit vom Hohlraumabstand und*

Spanungszustand. Tech. rep., Gesellschaft für Anlagen- und Reaktorsicherheit (GRS) mbH.

Witherspoon, P., Wang, J., Iwai, K., & Gale, J. (1980). Validity of cubic law for fluid flow in a deformable rock fracture. *Water Resources Research, 16*(6), 1016-1024.

Zang, A., Wagner, C., & Dresen, G. (1996). Acoustic emission, microstructure, and damage model of dry and wet sandstone stress to failure. *Journal of Geophysical Research, 101, Issue B8*, 17507-17521.

Zang, A., Wagner, F. C., Stanchits, S., Dresen, G., Andresen, R., & Haidekker, M. A. (1998). Source analysis of acoustic emissions in Aue granite cores under symmetric and asymmetric compressive loads. *Geophysical Journal International, 135*(3), 1113-1130.

Zhang, X., & Sanderson, D. (2002). *Numerical Modelling and Analysis of Fluid Flow and Deformation of Fractured Rock Masses.* Elesvier Science.

Zhang, X., Sanderson, D. J., & Barker, A. J. (2002). Numerical study of fluid flow of deforming fractured rocks using dual permeability model. *Geophysical Journal International, 151*(2), 452-468.

Zhang, X., Sanderson, D., Harkness, R., & Last, N. (1996). Evaluation of the 2-D permeability tensor for fractured rock masses. *International journal of rock mechanics and mining sciences & geomechanics abstracts, 33*(1), 17-37.

Zhang, Z., Zhang, R., Xie, H., Liu, J., & Were, P. (2015). Differences in the acoustic emission characteristics of rock salt compared with granite and marble during the damage evolution process. *Environmental Earth Sciences, 73*(11), 6987-6999.